2014

Non-Hydrostatic Models For Wave Propagation, Breaking, And Run-Up

Zhangping Wei
University of Mississippi

NON-HYDROSTATIC MODELS FOR

WAVE PROPAGATION, BREAKING, AND RUN-UP

A Dissertation
presented in partial fulfillment of requirements
for the degree of Doctor of Philosophy
in the National Center for Computational Hydroscience and Engineering
The University of Mississippi

by

Zhangping Wei

May 2014

ABSTRACT

This dissertation develops a series of non-hydrostatic pressure wave models based on the finite element free surface flow model, CCHE2D, for simulating propagation, breaking, and run-up of coastal wave processes.

The first non-hydrostatic formulation presented in this dissertation directly introduces a non-hydrostatic pressure module into CCHE2D. An edge-based pressure allocation method is implemented, and a depth-integrated vertical momentum equation is introduced. The depth-integrated horizontal momentum equations are solved for a provisional velocity field, and then the non-hydrostatic pressure is obtained by satisfying the divergence-free velocity field condition, subsequently the velocity field is corrected by the non-hydrostatic pressure. Finally, the free surface elevation is computed by the depth-integrated continuity equation.

Next, a depth-integrated non-hydrostatic model for simulating nearshore wave processes is developed by solving a depth-integrated vertical momentum equation and the conservation form of the shallow water equations including extra non-hydrostatic pressure terms. A pressure projection method and the divergence-free velocity field condition are used together to solve the non-hydrostatic pressure. To resolve discontinuous flows, involving breaking waves and hydraulic jumps, a momentum conservation advection scheme is developed. In addition, the model is implemented with a simple but efficient wetting and drying algorithm to deal with the moving shoreline.

The depth-integrated non-hydrostatic pressure models, which assume a linear distribution of the vertical pressure, have limitations in certain applications (e.g., propagation of highly dispersive waves). A multi-layer non-hydrostatic model is developed by adding more layers to the aforementioned second depth-integrated non-hydrostatic model. The multi-layer model is capable of resolving more realistic vertical flow structures and better

ii

representing the wave dynamics.

Finally, a well validated depth-integrated non-hydrostatic model is applied to simulate a wide range of coastal wave processes. These numerical tests further evaluate the non-hydrostatic model from different aspects of engineering practice. In particular, they demonstrate the efficiency of non-hydrostatic models for coastal wave modeling, and they also reveal the great potential of non-hydrostatic models to simulate real-life coastal wave processes.

DEDICATION

This dissertation is dedicated to my parents, Mr. Hanyin Wei and Ms. Yanzhen Yang, for their selfless love and endless support.

ACKNOWLEDGEMENTS

Marcus McGrath, Prof. Jilun Miao, Ms. Nuttita Pophet, Dr. Andi Rusdin, Dr. Dayong Shen, Ms. Tahmina Shirmeen, Ms. Meng Wang, Mr. Gangfeng Wu, Prof. Jihong Xia, Prof. Danrong Zhang, Dr. Mingliang Zhang, and Dr. Xiaoyan Zhou.

I have also been fortunate to receive help from many experts outside of NCCHE during my study. Special thanks go to the non-hydrostatic wave model leading developer, Dr. Marcel Zijlema at Delft University of Technology, the Netherlands, for sharing his insight and experience in non-hydrostatic model development with me. In addition, I would like to express my thanks to Prof. Kwok Fai Cheung and his two students Dr. Yoshiki Yamazaki and Dr. Volker Roeber at University of Hawaii at Manoa, for generously sharing with me their knowledge on depth-integrated non-hydrostatic model development, momentum conservation scheme in wave modeling, and valuable experimental data for model validation. Furthermore, I would like to thank Dr. Claire Mischker at the Graduate Writing Center of The University of Mississippi for proofreading my journal submissions and providing useful suggestions on my technical writing. What's more, I am lucky to have a benchmark database built on the experimental data provided by scholars and experts from around the world to validate my model, I would like to express my appreciation to all of them, particularly, to those whose data is used in this work (listed in alphabetical order): Prof. Serdar Beji at Istanbul Technical University, Turkey, Dr. Michael J. Briggs at Engineer Research & Development Center of US Army Corps of Engineers, Prof. Dubravka Pokrajac at University of Aberdeen, UK, and Prof. Fengyan Shi at University of Delaware.

Finally, I would like to express my deepest appreciation to my parents for giving me life and raising me up with their unconditional love, encouragement, and support through these years. With true love I would also like to thank my wife, Zhengping Zhou, for always believing in me and supporting me in my life and research. Without the love and support from my family, this dissertation would have been inconceivable.

Financial support for this dissertation is provided, in part, by (1) The Department of Homeland Security, managed by the Southeast Regional Research Initiative, administered

TABLE OF CONTENTS

LIST OF FIGURES

LIST OF TABLES

LIST OF ABBREVIATIONS

1D. . . . . One-dimensional

2D. . . . . Two-dimensional

3D. . . . . Three-dimensional

HFA. . . . . Hydrostatic Front Approximation

NLSW. . . . . Nonlinear Shallow Water

RANS. . . . . .Reynolds-averaged Navier-Stokes

SPH. . . . . .Smoothed Particle Hydrodynamics

CHAPTER 1

INTRODUCTION

In the past decades, increasing emphasis has been placed on the coastal wave process because of the rapid development of the coastal area and the tremendous impact of natural hazards (e.g., storm surge and tsunamis). Accurate prediction of wave and hydrodynamic processes in the coastal zone is essential to investigate coastal morphology, protect coastal structures, and mitigate coastal hazards. With the increment of our understanding about wave mechanics and the advancement of computer science and technology, the numerical model has become more and more popular for simulating nonlinear and dispersive wave propagation from deep water to shallow water.

1.1 Literature Review

1.1.1 Reynolds-averaged Navier-Stokes equations

The Reynolds-averaged Navier-Stokes (RANS) equations are obtained by temporally averaging of the Navier-Stokes equations, which describe the motion of fluid substances. As the wave propagation is one kind of flow motion, the RANS equations are very useful for coastal wave modeling. A model based on the RANS equations is valid over the entire range of the water depth and could be applied to simulate linear or nonlinear water wave propagation with or without energy dissipation (Li and Fleming, 2001).

One of the most challenging topics for modeling coastal waves is to simulate wave breaking, since (1) it requires the model to be able to accurately track the free surface location during the wave breaking process, and (2) the model must properly account for the physics of turbulence production, transport, and dissipation throughout the entire wave

breaking process (Liu and Losada, 2002). The RANS model is particularly useful for modeling the three-dimensional (3D) wave breaking process. With the aid of free surface tracking methods, such as the Marker-and-Cell method (Harlow and Welch, 1965), the Volume-of-Fluid method (Hirt and Nichols, 1981) and so on, a RANS model is able to simulate the detailed 3D wave breaking process and wave-structure interaction (e.g., Lin et al., 1999; Christensen and Deigaard, 2001; Lara et al., 2006, among others). Furthermore, the RANS equations coupled with a turbulence model, e.g., $k - \epsilon$ model (Rodi, 1993), is able to take into account the convection, production, and dissipation of turbulent kinetic energy during the wave breaking (e.g., Lin and Liu, 1998a,b; Higuera et al., 2013). However, due to the high computational expense of 3D simulation and the strict stability requirement of the free surface tracking methods, the RANS model is limited to the wave process in a small scale (e.g., laboratory experiments).

1.1.2 Smoothed Particle Hydrodynamics

In recent years, a mesh-free Lagrangian method, the so-called Smoothed Particle Hydrodynamics (SPH) method, has been adopted from the field of astrophysics (Gingold and Monaghan, 1977; Lucy, 1977) to fluid mechanics (Monaghan, 1994). In SPH, the state of a system is represented by a set of particles, which possess material properties and interact with each other within the range controlled by a weight function or smoothing function (Liu and Liu, 2010).

SPH offers a variety of advantages for modeling flow motion, particularly those with a free surface. As the particles move with the flow, there is no additional requirement to track the free surface as needed by the aforementioned RANS models. This property makes SPH very suitable for modeling the wave breaking process (e.g., Dalrymple and Rogers, 2006) and wave-structure interaction (e.g., Gomez-Gesteira and Dalrymple, 2004). In addition, SPH has an apparent advantage over other models of modeling wave interaction with porous structure in the coastal zone, as the discrete solid skeleton could be fully discretized using the

2

particles at adequate resolution without introducing further simplifying assumptions (Ren et al., 2014). There is no doubt that SPH provides a good alternative for modeling coastal waves using the particle technique, however, the computation becomes very expensive once a large computation domain is considered. Although there are several parallel versions of SPH models (e.g., Hérault et al., 2010), it is still very challenging to apply it to a real-life coastal wave process.

1.1.3 Nonlinear shallow water equations

In coastal engineering practice, several simplified but practical approaches are widely used to simulate coastal waves. Nonlinear shallow water (NLSW) equations are derived from depth-integrating the Navier-Stokes equations, in the case where the horizontal length scale is much greater than the vertical length scale. As a result, there is no vertical variation of horizontal velocity throughout the depth of the fluid, and the pressure field is hydrostatic (i.e., the vertical velocity is zero).

Due to the simple formulation of NLSW equations, they have been widely used for simulating different kinds of wave processes. Particularly, they are well suitable to simulate the so-called long waves. In practice, tide flows could be well simulated by a NLSW model (e.g., Titov and Synolakis, 1998), and a storm surge induced by the hurricane is also widely simulated by using NLSW models (e.g., Dietrich et al., 2011; Ding et al., 2012). Furthermore, NLSW models are capable of simulating tsunami wave processes in both laboratory and field scales (e.g., Satake, 1995; Wei et al., 2006).

In addition, NLSW equations with appropriate conservation properties are able to ensure accurate results for large gradient flows over rapidly varying topography (Stelling and Duinmeijer, 2003), so they could also be applied to the shallow water region from the surf zone to the shore. However, due to the lack of frequency dispersion, NLSW equations are not applicable for modeling waves in deep water.

1.1.4 Mild-slope equation

Built upon the linear wave theory, the mild-slope equation of Berkhoff (1976) describes the combined effects of diffraction and refraction for monochromatic wave propagation by assuming the water depth varies slowly over a wave length (i.e., $|\nabla h|/kh \leqslant 1$, where ∇ is the horizontal gradient operator, h is the water depth, and k is the wave number). There are several limitations in this classical mild-slope equation. First of all, as the higher-order bottom effect terms were neglected, the accuracy of this equation for predicting reflection from depth transitions having slopes is up to 1:3 (Booij, 1983). The equation is only suitable for regular wave propagation in a steady state as the time derivative term is absent in the formulation.

Because of the efficiency of the mild-slope equation to simulate wave process from deep water to shallow water and its low computation cost, considerable efforts have been made to extend the capability of the mild-slope equation. To consider a rapidly varying topography such as a steep slope or an undulatory bottom, the second-order bottom effect terms have been included in the mild-slope equation (e.g., Suh et al., 1997). In order to predict the propagation of random waves with a narrow frequency band, time-dependent mild-slope equations were developed in the elliptic form (e.g., Massel, 1993) and also the hyperbolic form (e.g., Chamberlain and Porter, 1995). Furthermore, the mild-slope equation was modified by including the ambient current effect (e.g., Kirby, 1984; Chen et al., 2005). Moreover, the wave breaking process and associated energy dissipation could also be incorporated into the mild-slope equation (e.g., Kubo et al., 1992; Beltrami et al., 2001). In addition, efforts have also been made to account for the bed friction effect on wave propagation in its formulation (Demirbilek and Panchang, 1998). However, it is rare to apply the elliptic-type mild-slope equation in the swash zone, as one encounters the difficulty of specifying boundary conditions along the shoreline, which are essential for solving the elliptic equation (Liu and Losada, 2002).

1.1.5 Boussinesq-type equations

Another popular approach for modeling wave transformation from deep water to shallow water is to solve Boussinesq-type equations. The basic idea of Boussinesq-type equations is the elimination of vertical coordinate, while accounting for some influences of the vertical acceleration (Dingemans, 1997). The classical Boussinesq equations of Peregrine (1967), which lays the foundation for several well-known Boussinesq-type equations used today, only consider weak nonlinearity and weak dispersion, and therefore, his formulation is only applicable to the water depth parameter $kh < 0.75$ in practice (Madsen et al., 2002).

In general, improvements have been obtained to alleviate, if not eliminate, the restrictions of weak dispersion and weak nonlinearity. To increase the frequency dispersion, the classical Boussinesq equations could be extended by either adding a third-order term to consider the dispersion in deep water (Madsen et al., 1991) or using the velocity at a reference depth instead of the depth-integrated velocity (Nwogu, 1993). In addition, use of high-order terms (e.g., Agnon et al., 1999; Gobbi et al., 2000; Madsen et al., 2002) and multiple layers (Lynett and Liu, 2004) in Boussinesq-type models could also improve the frequency dispersion approximation. Meanwhile, the so-called highly or fully nonlinear Boussinesq-type equations have also been derived in various ways (e.g., Wei et al., 1995; Madsen et al., 2003). Recent research of Boussinesq-type models focuses on development of the shock-capturing capability by locally switching back to the NLSW model and treating the wave breaking process with a shock-capturing numerical scheme (e.g., Tonelli and Petti, 2010; Roeber et al., 2010; Shi et al., 2012).

Although numerical models built on the well-established Boussinesq-type equations have been widely used to simulate wave motions, there are several well-known issues of them. These higher-order Boussinesq-type equations usually involve complicated discretization and expensive computation. In order to apply the Boussinesq-type models for simulating nearshore processes, wave breaking has to be treated carefully. Since Boussinesq-type equations are depth-integrated formulations in nature, they cannot describe the overturning of

the free surface. Besides, the classical Boussinesq equations are derived under the assumption of an irrotational and inviscid flow (Peregrine, 1967), they cannot directly account for energy dissipation caused by wave breaking. Several semi-empirical approaches have been developed to address these issues (e.g., Zelt, 1991; Schäffer et al., 1993; Veeramony and Svendsen, 2000). Generally, these approaches have to add an extra dissipation term in the momentum equation, and provide predefined criteria for the onset and cessation of wave breaking and energy dissipation rate by calibration using laboratory experiments. In this regard, the reliability of those tunable parameters is likely dependent on the similarity between the considered case and the experiment, and the accuracy of the experimental data.

1.1.6   Non-hydrostatic method

A relatively new approach for modeling water waves is the so-called non-hydrostatic method. The non-hydrostatic method for simulating water waves still solves the RANS equations, and it explicitly includes the non-hydrostatic pressure to account for the vertical acceleration of flows (Casulli and Stelling, 1998; Stansby and Zhou, 1998). Usually the non-hydrostatic model solves the free surface motion with the depth-integrated continuity equation, and it therefore requires a much lower vertical resolution than that of numerical models with the free surface tracking methods. This property makes the non-hydrostatic model a favorable choice to large-scale applications in coastal engineering. An important issue that determines the efficiency and accuracy of the non-hydrostatic model is the free surface pressure boundary condition. In earlier non-hydrostatic model developments, due to a staggered grid configuration in the vertical direction, the non-hydrostatic pressure is specified at the cell center, and the hydrostatic pressure assumption is made for the free surface layer (e.g., Casulli and Stelling, 1998; Casulli, 1999; Li and Fleming, 2001; Namin et al., 2001; Casulli and Zanolli, 2002; Chen, 2003). This approximation ignores the non-hydrostatic pressure effect at the free surface. As a result, a relatively large number of vertical layers (i.e. 10 - 20 layers) is required to resolve the wave dispersion to an acceptable

level of accuracy.

Stelling and Zijlema (2003) proposed an edge-based compact difference scheme to approximate the vertical gradient of the non-hydrostatic pressure located at the interface between vertical layers, in this way, the zero pressure boundary condition can be precisely specified at the free surface. Furthermore, this pressure allocation method makes even the depth-integrated (one-layer) non-hydrostatic model be able to account for the vertical variation of the flow field, and this capability is absent in other depth-integrated models based on the NLSW equations. It turns out that their two-layer non-hydrostatic model shows similar linear dispersion characteristics as the extended Boussinesq-type models of Madsen and Sørensen (1992) and Nwogu (1993). Later on, they implemented an efficient and stable solver for the non-hydrostatic pressure (Zijlema and Stelling, 2005) and released an operational public domain code: SWASH (Zijlema et al., 2011). To date, their approach has been adopted in other models for simulating wave motions (e.g., Walters, 2005; Yamazaki et al., 2008; Ai et al., 2010; Cui et al., 2012; Ma et al., 2012).

Similar to Boussinesq-type models, non-hydrostatic models simulate the lumped effects of wave breaking rather than the detailed process. So far, the techniques for modeling wave breaking used by non-hydrostatic models are based on the physical principle applied in open channel hydraulics. It has been observed that the NLSW equations can appropriately handle discontinuous flows (e.g., hydraulic jumps and bores) with steep gradients, if the momentum is conserved at the discretized level (Stelling and Duinmeijer, 2003). Consequently, non-hydrostatic models with this property are able to track the actual location of wave breaking and compute the associated energy dissipation correctly without any predefined criteria and empirical parameters as used by Boussinesq-type models (Zijlema and Stelling, 2008). To achieve momentum conservation in the formulation, two strategies have been used. Stelling and Duinmeijer (2003) developed a momentum conservation scheme based on the fully staggered grid, their scheme has been used to handle wave breaking when the non-conservation form of governing equations is considered (Yamazaki et al., 2008; Zijlema et al.,

2011). The other way is to solve the conservation form of governing equations directly, since momentum conservation is automatically taken into account (Zijlema and Stelling, 2008; Ai and Jin, 2012; Ma et al., 2012). A major concern recently addressed in the development of non-hydrostatic models is related to the model efficiency when it is applied to the surf zone, in which energetic wave breaking process requires the model with a relatively high vertical resolution (i.e. 10-20 layers) to obtain accurate results, while wave processes in the rest nearshore zone can be simulated fairly well with a much lower vertical resolution (i.e. 1-3 layers). Smit et al. (2013) proposed a hydrostatic front approximation (HFA) scheme, which assumes a hydrostatic pressure distribution at the front of a breaking wave, and then the wave can rapidly transit into a bore-like shape. As a consequence, the non-hydrostatic model with a low vertical resolution can be applied to the whole nearshore zone at a significantly reduced computational cost. Because of its simplicity and efficiency, the non-hydrostatic method has gained more and more attention in coastal wave modeling community. See recent work of Smit et al. (2014) and Rijnsdorp et al. (2014), among others.

1.2   CCHE2D & 3D Models

In the past decades, strong efforts have been made by scientists at the National Center for Computational Hydroscience & Engineering, The University of Mississippi, USA to develop state-of-the-art numerical models for hydraulic engineering practice. In this section, the status of well verified and validated CCHE2D & 3D, among other models, are briefly reviewed, as they are closely related to this dissertation work. Developments of both models were based on a special finite element method, *Efficient Element Method* of Wang and Hu (1992). The depth-integrated two-dimensional (2D) free surface flow model CCHE2D (Jia and Wang, 1999, 2001; Jia et al., 2002) implicitly solves the NLSW equations based on a partially staggered grid. Specifically, the velocity field is solved on the collocation grid using a velocity correction method, on the other hand, the pressure field is solved on the staggered grid in a finite volume fashion. In terms of the model capability, to date, CCHE2D has been

applied for simulating unsteady turbulent free surface flows, sediment transport, pollutant transport, water quality, flooding, and estuary and coastal process (Jia, 2013a). It should be mentioned that the wave model of CCHE2D-COAST (e.g., Ding and Wang, 2008), which solves the spectral energy balance equation, is a phase-averaged wave model. As a result, it does not simulate the time-varying process of short waves. In CCHE3D (Jia, 2013b), both hydrostatic and non-hydrostatic (hydrodynamic) pressure assumptions can be considered in the 3D solutions according to different test cases. Similar to CCHE2D, a velocity correction method is used to solve the pressure field. CCHE3D has also been extended to study sediment transport, morphological change, pollutant transport, and water quality. It is worth mentioning that the non-hydrostatic pressure of the CCHE3D model is located at the cell center, which is consistent with traditional non-hydrostatic models (e.g., Casulli and Stelling, 1998).

1.3 Research Objectives
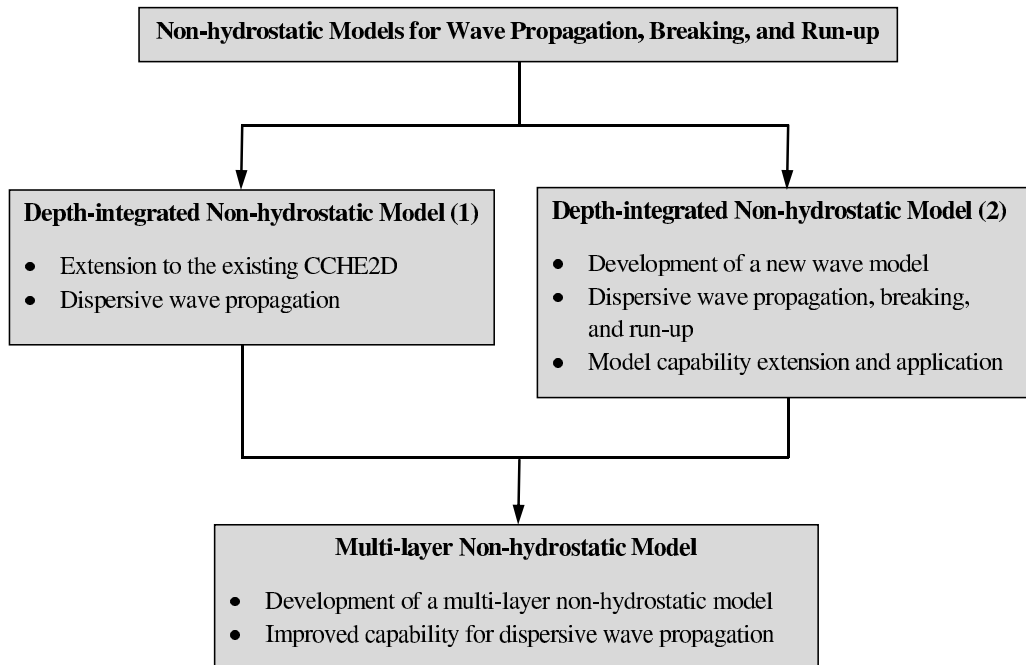
Figure 1.1. Outline of dissertation research objectives

This dissertation integrates the experience of previous non-hydrostatic methods for

9

modeling wave motions, and develops several non-hydrostatic models based on the free surface flow model, CCHE2D, for simulating propagation, breaking, and run-up of nonlinear dispersive waves, which are widely encountered in the coastal zone. Figure 1.1 shows the outline of the dissertation research objectives. They are further listed as follows:

(1) Development of a depth-integrated non-hydrostatic model for weakly dispersive wave propagation by introducing the non-hydrostatic pressure approach into the existing free surface flow model, CCHE2D. Specifically, the edge-based non-hydrostatic pressure allocation method is introduced into CCHE2D, and the existing momentum equations are solved for a provisional velocity field. Next, the non-hydrostatic pressure is obtained by satisfying the divergence-free velocity field condition, and then the velocity field is corrected by the non-hydrostatic pressure. Finally, the free surface elevation is computed by the depth-integrated continuity equation.

(2) Development of a new depth-integrated non-hydrostatic model, CCHE2D-NHWAVE, for simulating nearshore wave processes. Based on the experience gained in the previous development, the second task develops a depth-integrated non-hydrostatic finite element model for simulating nearshore wave processes involving propagation, breaking, and run-up of dispersive waves. The governing equations are a depth-integrated vertical momentum equation and the conservation form of the NLSW equations including extra non-hydrostatic pressure terms. The Efficient Element Method is still used to solve the governing equation on a partially staggered grid using a pressure projection method. To resolve discontinuous flows including breaking waves and hydraulic jumps, a momentum conservation advection scheme is developed on the basis of the partially staggered grid. In addition, the model is implemented with a simple but efficient wetting and drying algorithm to deal with the moving shoreline.

(3) Development of a multi-layer non-hydrostatic model with an improved capability for modeling dispersive waves. In order to simulate highly dispersive waves and better

10

approximate vertical structure of flows, a multi-layer (or 3D) non-hydrostatic model is needed. The third task aims to develop a multi-layer model for wave propagation by extending the depth-integrated model developed in Objective (2) with several strictly horizontal layers in the vertical direction. A similar numerical procedure is applied to solve the governing equations in several steps.

(4) Application of the non-hydrostatic model for simulating a wide range of coastal wave processes. To fulfill the dissertation objective, the last task applies the well verified and validated CCHE2D-NHWAVE, which is capable of considering weakly dispersive wave propagation, breaking, and run-up, for predicting several types of coastal wave processes. Through these investigations, the capability of the model for simulating real-life coastal wave processes is thoroughly evaluated.

1.4   Dissertation Contents

In the following chapters, Chapter 2 describes the derivation of the governing equations for the depth-integrated and multi-layer non-hydrostatic wave models from the 3D continuity equation and the RANS equations. The numerical boundary conditions used in this dissertation are also presented. In Chapter 3, a depth-integrated non-hydrostatic finite element model for wave propagation is developed by introducing the non-hydrostatic pressure approach into the existing free surface flow model, CCHE2D. Chapter 4 focuses on developing a depth-integrated non-hydrostatic model for simulating nearshore wave processes, different from the work in Chapter 3, the new model solves the conservation form of governing equations with a momentum conservation advection scheme, and a simple but efficient wetting and drying algorithm is incorporated to model the moving shoreline. In Chapter 5, continuing effort is made to extend the depth-integrated non-hydrostatic formulation presented in Chapter 4 to be a multi-layer model. In Chapter 6, a well validated non-hydrostatic model is applied to study a wide range of coastal wave processes. Finally, the summary of this dissertation and recommendation for future work are presented in Chapter 7.

CHAPTER 2

MATHEMATICAL FORMULATION

In this chapter, the governing equations for non-hydrostatic wave models are derived from the 3D continuity equation and the RANS equations. In addition, the boundary conditions used in this dissertation are also presented.

2.1 Governing Equations for the Depth-integrated Non-hydrostatic Models
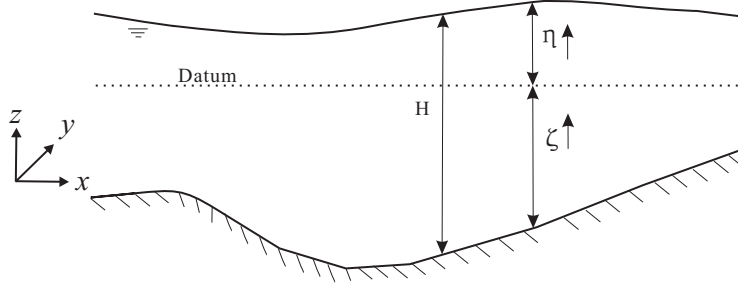
Figure 2.1. Computational domain with the free surface and the bottom.

We consider a physical domain in a Cartesian coordinate system (x, y, z) that is vertically bounded by the free surface elevation $\eta(x, y, t)$ and the bed elevation $\zeta(x, y)$ as shown in Figure 2.1, where t is the time, and the water depth is $H(x, y, t) = \eta(x, y, t) - \zeta(x, y)$. The vertical datum is usually set equal to the still water level (sea level) for coastal and oceanographic studies. The incompressible 3D continuity equation and the RANS equations are given by

$$\frac{\partial u}{\partial x} + \frac{\partial v}{\partial y} + \frac{\partial w}{\partial z} = 0 \qquad (2.1)$$

$$\frac{\partial u}{\partial t} + \frac{\partial uu}{\partial x} + \frac{\partial uv}{\partial y} + \frac{\partial uw}{\partial z} = -\frac{1}{\rho}\frac{\partial p}{\partial x} + \frac{1}{\rho}\left(\frac{\partial \tau_{xx}}{\partial x} + \frac{\partial \tau_{xy}}{\partial y} + \frac{\partial \tau_{xz}}{\partial z}\right) \qquad (2.2)$$

$$\frac{\partial v}{\partial t} + \frac{\partial uv}{\partial x} + \frac{\partial vv}{\partial y} + \frac{\partial vw}{\partial z} = -\frac{1}{\rho}\frac{\partial p}{\partial y} + \frac{1}{\rho}\left(\frac{\partial \tau_{yx}}{\partial x} + \frac{\partial \tau_{yy}}{\partial y} + \frac{\partial \tau_{yz}}{\partial z}\right) \qquad (2.3)$$

12

$$\frac{\partial w}{\partial t} + \frac{\partial uw}{\partial x} + \frac{\partial vw}{\partial y} + \frac{\partial ww}{\partial z} = -g - \frac{1}{\rho}\frac{\partial p}{\partial z} + \frac{1}{\rho}\left(\frac{\partial \tau_{zx}}{\partial x} + \frac{\partial \tau_{zy}}{\partial y} + \frac{\partial \tau_{zz}}{\partial z}\right) \tag{2.4}$$

where (u, v, w) is flow velocity in the x, y, and z directions; ρ is the water density; p is the total pressure; g is the gravitational acceleration; τ_{xx}, τ_{xy},$\cdots$, and τ_{zz} are the stresses.

The kinematic boundary conditions at the free surface and the bottom are given by

$$w_\eta = \frac{D\eta}{Dt} = \frac{\partial \eta}{\partial t} + u_\eta\frac{\partial \eta}{\partial x} + v_\eta\frac{\partial \eta}{\partial y} \tag{2.5}$$

$$w_\zeta = \frac{D\zeta}{Dt} = u_\zeta\frac{\partial \zeta}{\partial x} + v_\zeta\frac{\partial \zeta}{\partial y} \tag{2.6}$$

the total pressure is decomposed into hydrostatic and non-hydrostatic parts (Casulli and Stelling, 1998; Stelling and Zijlema, 2003) as

$$p = \rho g(\eta - z) + \hat{q} \tag{2.7}$$

where $\hat{q}$ denotes the non-hydrostatic pressure. It is assumed that the vertical advection and dissipation terms are small compared with the non-hydrostatic pressure term, and then substitution of Equation (2.7) into Equations (2.2), (2.3), and (2.4) gives

$$\frac{\partial u}{\partial t} + \frac{\partial uu}{\partial x} + \frac{\partial uv}{\partial y} + \frac{\partial uw}{\partial z} = -g\frac{\partial \eta}{\partial x} - \frac{1}{\rho}\frac{\partial \hat{q}}{\partial x} + \frac{1}{\rho}\left(\frac{\partial \tau_{xx}}{\partial x} + \frac{\partial \tau_{xy}}{\partial y} + \frac{\partial \tau_{xz}}{\partial z}\right) \tag{2.8}$$

$$\frac{\partial v}{\partial t} + \frac{\partial uv}{\partial x} + \frac{\partial vv}{\partial y} + \frac{\partial vw}{\partial z} = -g\frac{\partial \eta}{\partial y} - \frac{1}{\rho}\frac{\partial \hat{q}}{\partial y} + \frac{1}{\rho}\left(\frac{\partial \tau_{yx}}{\partial x} + \frac{\partial \tau_{yy}}{\partial y} + \frac{\partial \tau_{yz}}{\partial z}\right) \tag{2.9}$$

$$\frac{\partial w}{\partial t} = -\frac{1}{\rho}\frac{\partial \hat{q}}{\partial z} \tag{2.10}$$

Equations (2.1), (2.8), (2.9), and (2.10) are averaged over the water depth H to derive a set of depth-integrated governing equations, which are similar to the NLSW equations but including extra non-hydrostatic pressure terms. In this study, only the integration of the non-hydrostatic pressure terms will be treated in detail, the depth integration of the rest terms

will not be repeated here as it appears in many standard references (e.g., Wu, 2007). Walters (2005) assumed that the non-hydrostatic pressure can be expressed in terms of a horizontal variation and a vertical profile by

$$\hat{q}(x, y, z, t) = q(x, y, \zeta, t) f(z) \tag{2.11}$$

where $q(x, y, \zeta, t)$ is the non-hydrostatic pressure at the bed surface, and $f(z)$ is a function used to define the vertical distribution of the non-hydrostatic pressure. It is noted that $\hat{q}(x, y, \eta, t)$, the non-hydrostatic pressure at the free surface, is the atmospheric pressure with the value equal to zero. By virtue of the Leibniz rule, the depth-integration of the non-hydrostatic pressure term in the u momentum equation is

$$\int_{\zeta}^{\eta} \frac{\partial \hat{q}}{\partial x} \, \mathrm{d}z = \frac{\partial}{\partial x} q \int_{\zeta}^{\eta} f(z) \, \mathrm{d}z + q f(\zeta) \frac{\partial \zeta}{\partial z} \tag{2.12}$$

In this study, the vertical distribution of the non-hydrostatic pressure is assumed to be linear, which implies that $f(\eta) = 0$, $f(\zeta) = 1$, and $\int_{\zeta}^{\eta} f(z) dz = \frac{1}{2} H$. As a result, the above equation is written as

$$\int_{\zeta}^{\eta} \frac{\partial \hat{q}}{\partial x} \, \mathrm{d}z = \frac{1}{2} \left(H \frac{\partial q}{\partial x} + q \left(\frac{\partial \eta}{\partial x} + \frac{\partial \zeta}{\partial x} \right) \right) \tag{2.13}$$

A similar expression can be derived for the non-hydrostatic pressure term in the v momentum equation. Finally, the depth-integrated governing equations in the conservation form are derived as

$$\frac{\partial H}{\partial t} + \frac{\partial (HU)}{\partial x} + \frac{\partial (HV)}{\partial y} = 0 \tag{2.14}$$

$$\begin{aligned}
\frac{\partial (HU)}{\partial t} + \frac{\partial (HUU)}{\partial x} + \frac{\partial (HUV)}{\partial y} &= -gH \frac{\partial \eta}{\partial x} - \frac{1}{2\rho} \left(H \frac{\partial q}{\partial x} + q \left(\frac{\partial \eta}{\partial x} + \frac{\partial \zeta}{\partial x} \right) \right) \\
&\quad - \frac{gn^2 U}{H^{1/3}} \sqrt{U^2 + V^2} + \left(\frac{\partial (HT_{xx})}{\partial x} + \frac{\partial (HT_{xy})}{\partial y} \right)
\end{aligned} \tag{2.15}$$

$$\frac{\partial(HV)}{\partial t} + \frac{\partial(HUV)}{\partial x} + \frac{\partial(HVV)}{\partial y} = -gH\frac{\partial\eta}{\partial y} - \frac{1}{2\rho}\left(H\frac{\partial q}{\partial y} + q\left(\frac{\partial\eta}{\partial y} + \frac{\partial\zeta}{\partial y}\right)\right)$$
$$- \frac{gn^2 V}{H^{1/3}}\sqrt{U^2 + V^2} + \left(\frac{\partial(HT_{yx})}{\partial x} + \frac{\partial(HT_{yy})}{\partial y}\right) \tag{2.16}$$

$$\frac{DW}{Dt} = \frac{q}{\rho H} \tag{2.17}$$

where U, V, and W are the depth-integrated velocity components in the x, y, and z directions, respectively. Chapter 3 solves the non-conservation form of governing equations, which can be easily obtained by rearranging Equations (2.14), (2.15), (2.16), and (2.17), they will not be repeated here.

It is noted that the governing equations above are in terms of the flux terms $Q^u = HU$ and $Q^v = HV$, not the primitive variables U and V. To obtain the conservation form of momentum equations for U and V, following Zijlema and Stelling (2008) and Ai et al. (2010), we multiply Equation (2.14) with U and V, and subtract these equations from Equations (2.15) and (2.16), respectively, and then the reformulated momentum equations are given by

$$H\frac{\partial U}{\partial t} + \frac{\partial(HUU)}{\partial x} - U\frac{\partial(HU)}{\partial x} + \frac{\partial(HUV)}{\partial y} - U\frac{\partial(HV)}{\partial y} = -gH\frac{\partial\eta}{\partial x}$$
$$- \frac{1}{2\rho}\left(H\frac{\partial q}{\partial x} + q\left(\frac{\partial\eta}{\partial x} + \frac{\partial\zeta}{\partial x}\right)\right) - \frac{gn^2 U}{H^{1/3}}\sqrt{U^2 + V^2} + \left(\frac{\partial(HT_{xx})}{\partial x} + \frac{\partial(HT_{xy})}{\partial y}\right) \tag{2.18}$$

$$H\frac{\partial V}{\partial t} + \frac{\partial(HUV)}{\partial x} - V\frac{\partial(HU)}{\partial x} + \frac{\partial(HVV)}{\partial y} - V\frac{\partial(HV)}{\partial y} = -gH\frac{\partial\eta}{\partial y}$$
$$- \frac{1}{2\rho}\left(H\frac{\partial q}{\partial y} + q\left(\frac{\partial\eta}{\partial y} + \frac{\partial\zeta}{\partial y}\right)\right) - \frac{gn^2 V}{H^{1/3}}\sqrt{U^2 + V^2} + \left(\frac{\partial(HT_{yx})}{\partial x} + \frac{\partial(HT_{yy})}{\partial y}\right) \tag{2.19}$$

where n is the Manning roughness coefficient, and the depth-integrated normal and shear stresses (normalized by the water density) are given by

$$T_{xx} = 2\nu_t\frac{\partial U}{\partial x} \tag{2.20}$$

$$T_{xy} = T_{yx} = \nu_t\left(\frac{\partial V}{\partial x} + \frac{\partial U}{\partial y}\right) \tag{2.21}$$

15

$$T_{yy} = 2\nu_t \frac{\partial V}{\partial y} \tag{2.22}$$

in which ν_t is the turbulent kinematic viscosity due to wave breaking and subgrid turbulence. In this development, ν_t is estimated by the Smagorinsky subgrid model (Smagorinsky, 1963) as

$$\nu_t = (C_s \Delta_s)^2 \sqrt{2\left(\left(\frac{\partial U}{\partial x}\right)^2 + \left(\frac{\partial V}{\partial y}\right)^2 + \frac{1}{2}\left(\frac{\partial U}{\partial y} + \frac{\partial V}{\partial x}\right)^2\right)} \tag{2.23}$$

and the Smagorinsky constant C_s is usually given a value between 0.1 and 0.2, and 0.2 is used in this study. The length scale parameter Δ_s defines the smallest resolvable eddy, it is approximated by $\Delta_s = \sqrt{\Delta_x \Delta_y}$ with mesh sizes Δ_x and Δ_y in x and y directions, respectively.

2.2   Governing Equations for the Multi-layer Non-hydrostatic Model
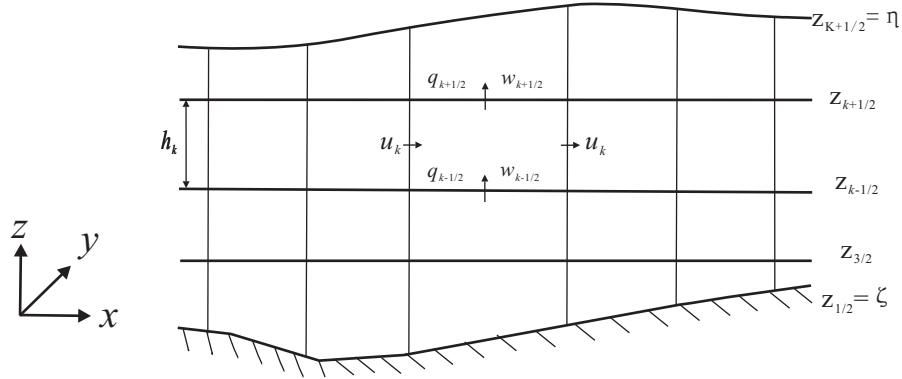
Figure 2.2. Definition sketch of variable arrangements in the x-z plane.

In Chapter 5, a multi-layer non-hydrostatic model is developed on the basis of the already developed depth-integrated non-hydrostatic model presented in Chapter 4. In the vertical direction, the physical domain is divided into several layers with multiple strictly horizontal layer interfaces. The edge-based pressure allocation method is still kept. As a result, the non-hydrostatic pressure and the vertical velocity are located at the interface between vertical layers, and the horizontal velocities are allocated at the middle of each layer. As an example, Figure 2.2 shows the variable arrangements in the x-z plane, where the layer k is bounded by layer interfaces $z_{k-1/2}(x, y, t)$ and $z_{k+1/2}(x, y, t)$, and its thickness

16

is h_k, which is defined by $h_k = \min\left(z_{k+1/2}, \eta\right) - \max\left(z_{k-1/2}, \zeta\right)$. Consequently, the cell is active in the computation only if $h_k > 0$.

To derive the governing equations for the multi-layer non-hydrostatic model, it is assumed the advection and dissipation terms in the vertical momentum equation are smaller than the non-hydrostatic pressure term. As a result, we have the incompressible continuity equation (2.1) and the simplified momentum equations as follows

$$\frac{\partial u}{\partial t} + \frac{\partial uu}{\partial x} + \frac{\partial uv}{\partial y} + \frac{\partial uw}{\partial z} = -g\frac{\partial \eta}{\partial x} - \frac{1}{\rho}\frac{\partial q}{\partial x} + \frac{1}{\rho}\left(\frac{\partial \tau_{xx}}{\partial x} + \frac{\partial \tau_{xy}}{\partial y} + \frac{\partial \tau_{xz}}{\partial z}\right) \tag{2.24}$$

$$\frac{\partial v}{\partial t} + \frac{\partial uv}{\partial x} + \frac{\partial vv}{\partial y} + \frac{\partial vw}{\partial z} = -g\frac{\partial \eta}{\partial y} - \frac{1}{\rho}\frac{\partial q}{\partial y} + \frac{1}{\rho}\left(\frac{\partial \tau_{yx}}{\partial x} + \frac{\partial \tau_{yy}}{\partial y} + \frac{\partial \tau_{yz}}{\partial z}\right) \tag{2.25}$$

$$\frac{\partial w}{\partial t} = -\frac{1}{\rho}\frac{\partial q}{\partial z} \tag{2.26}$$

In the following sections, similar to the work of Zijlema and Stelling (2005), Integration of Equations (2.1), (2.24), and (2.25) from $z_{k-1/2}$ to $z_{k+1/2}$, and Equation (2.26) from z_k to z_{k+1} gives the governing equations for the multi-layer non-hydrostatic model.

2.2.1 Layer integration of the continuity equation and free surface equation

By utilizing the Leibniz rule, Equation (2.1) is vertically integrated from $z_{k-1/2}$ to $z_{k+1/2}$ as follows

$$\int_{z_{k-1/2}}^{z_{k+1/2}} \left(\frac{\partial u}{\partial x} + \frac{\partial v}{\partial y} + \frac{\partial w}{\partial z}\right) \mathrm{d}z =$$
$$\frac{\partial (hu)_k}{\partial x} + \frac{\partial (hv)_k}{\partial y} - u\frac{\partial z}{\partial x}\Big|_{z_{k-1/2}}^{z_{k+1/2}} - v\frac{\partial z}{\partial y}\Big|_{z_{k-1/2}}^{z_{k+1/2}} + w_{k+1/2} - w_{k-1/2} = 0 \tag{2.27}$$

It should pointed out that there is no assumption made in the above equation. We apply the kinematic boundary conditions at layer k, one has

$$\frac{\partial h_k}{\partial t} + \frac{\partial (hu)_k}{\partial x} + \frac{\partial (hv)_k}{\partial y} = 0 \tag{2.28}$$

17

On the other hand, Equation (2.1) can also be vertically integrated from ζ to η by considering the kinematic boundary conditions at the bottom and the free surface, one has

$$\int_\zeta^\eta \left(\frac{\partial u}{\partial x} + \frac{\partial v}{\partial y} + \frac{\partial w}{\partial z} \right) dz = \frac{\partial \eta}{\partial t} + \frac{\partial}{\partial x} \int_\zeta^\eta u \, dz + \frac{\partial}{\partial y} \int_\zeta^\eta v \, dz = 0 \tag{2.29}$$

in which the vertical integration of velocity is approximated by the summation of the flux at each layer, e.g.,

$$\int_\zeta^\eta u \, dz = \sum_{k=1}^K h_k u_k \tag{2.30}$$

2.2.2 Layer integration of the horizontal momentum equations

In this section, layer integration of each term in the u momentum equation from $z_{k-1/2}$ to $z_{k+1/2}$ is presented in detail. First of all, the layer integration of the time derivative term is

$$\int_{z_{k-1/2}}^{z_{k+1/2}} \frac{\partial u}{\partial t} \, dz = \frac{\partial (hu)_k}{\partial t} - u \frac{\partial z}{\partial t} \Big|_{z_{k-1/2}}^{z_{k+1/2}} \tag{2.31}$$

And then, we integrate each of the advection terms. The first one is integrated by

$$\int_{z_{k-1/2}}^{z_{k+1/2}} \frac{\partial u^2}{\partial x} \, dz = \frac{\partial}{\partial x} \int_{z_{k-1/2}}^{z_{k+1/2}} u^2 \, dz - u^2 \frac{\partial z}{\partial x} \Big|_{z_{k-1/2}}^{z_{k+1/2}} \tag{2.32}$$

It is assumed that the dispersion effect due to the vertical non-uniformities of the flow velocity can be neglected (Zijlema and Stelling, 2005), one has

$$\int_{z_{k-1/2}}^{z_{k+1/2}} \frac{\partial u^2}{\partial x} \, dz = \frac{\partial (huu)_k}{\partial x} - u^2 \frac{\partial z}{\partial x} \Big|_{z_{k-1/2}}^{z_{k+1/2}} \tag{2.33}$$

Similarly, the second and third advection terms are obtained by

$$\int_{z_{k-1/2}}^{z_{k+1/2}} \frac{\partial uv}{\partial y} \, dz = \frac{\partial (huv)_k}{\partial y} - uv \frac{\partial z}{\partial y} \Big|_{z_{k-1/2}}^{z_{k+1/2}} \tag{2.34}$$

$$\int_{z_{k-1/2}}^{z_{k+1/2}} \frac{\partial uw}{\partial z} \, dz = (uw)_{k+1/2} - (uw)_{k-1/2} \tag{2.35}$$

18

Since the horizontal velocity is defined at the layer center, its value at the layer interface is approximated by

$$u_{k+1/2} = \frac{u_k h_{k+1} + u_{k+1} h_k}{h_k + h_{k+1}} \tag{2.36}$$

Next, we consider the layer integration of the dissipation terms. The first dissipation term in Equation (2.24) is integrated as

$$\int_{z_{k-1/2}}^{z_{k+1/2}} \frac{\partial \tau_{xx}}{\partial x} \, dz = \frac{\partial}{\partial x} \left(\int_{z_{k-1/2}}^{z_{k+1/2}} \tau_{xx} \, dz \right) - \tau_{xx} \frac{\partial z}{\partial x} \Big|_{z_{k-1/2}}^{z_{k+1/2}} \tag{2.37}$$

Similarly, the second and third dissipation terms are obtained as

$$\int_{z_{k-1/2}}^{z_{k+1/2}} \frac{\partial \tau_{xy}}{\partial y} \, dz = \frac{\partial}{\partial y} \left(\int_{z_{k-1/2}}^{z_{k+1/2}} \tau_{xy} \, dz \right) - \tau_{xy} \frac{\partial z}{\partial y} \Big|_{z_{k-1/2}}^{z_{k+1/2}} \tag{2.38}$$

$$\int_{z_{k-1/2}}^{z_{k+1/2}} \frac{\partial \tau_{xz}}{\partial z} \, dz = \tau_{xz,k+1/2} - \tau_{xz,k-1/2} \tag{2.39}$$

The gradient of free surface elevation is independent of the water depth, so the vertical integration will have no effect. And the non-hydrostatic pressure term is integrated as

$$\int_{z_{k-1/2}}^{z_{k+1/2}} \frac{\partial q}{\partial x} \, dz = \frac{\partial}{\partial x} \int_{z_{k-1/2}}^{z_{k+1/2}} q \, dz - q \frac{\partial z}{\partial x} \Big|_{z_{k-1/2}}^{z_{k+1/2}} \tag{2.40}$$

where the integral is approximated by following Zijlema and Stelling (2005) as

$$\int_{z_{k-1/2}}^{z_{k+1/2}} q \, dz \approx \frac{1}{2} h_k \left(q_{k+1/2} + q_{k-1/2} \right) = h_k q_k \tag{2.41}$$

Similar steps can be applied to integrate the v momentum equation. In summary,

the layer integrated horizontal momentum equations are given by

$$\frac{\partial(hu)_k}{\partial t} + \frac{\partial(huu)_k}{\partial x} + \frac{\partial(huv)_k}{\partial y} + u_{k+1/2}w_{k+1/2} - u_{k-1/2}w_{k-1/2} =$$

$$-gh_k\frac{\partial\eta}{\partial x} - \frac{1}{\rho}\left(\frac{\partial h_k q_k}{\partial x} - q\frac{\partial z}{\partial x}\Big|_{z_{k-1/2}}^{z_{k+1/2}}\right) + \left[\frac{\partial(hT_{xx})_k}{\partial x} + \frac{\partial(hT_{xy})_k}{\partial y}\right] + \frac{1}{\rho}\left[(\tau_x)_{k+1/2} - (\tau_x)_{k-1/2}\right]$$

$$(2.42)$$

$$\frac{\partial(hv)_k}{\partial t} + \frac{\partial(huv)_k}{\partial x} + \frac{\partial(hvv)_k}{\partial y} + v_{k+1/2}w_{k+1/2} - v_{k-1/2}w_{k-1/2} =$$

$$-gh_k\frac{\partial\eta}{\partial y} - \frac{1}{\rho}\left(\frac{\partial h_k q_k}{\partial y} - q\frac{\partial z}{\partial y}\Big|_{z_{k-1/2}}^{z_{k+1/2}}\right) + \left[\frac{\partial(hT_{yx})_k}{\partial x} + \frac{\partial(hT_{yy})_k}{\partial y}\right] + \frac{1}{\rho}\left[(\tau_y)_{k+1/2} - (\tau_y)_{k-1/2}\right]$$

$$(2.43)$$

where T_{xx}, T_{xy}, T_{yx}, and T_{yy} are normal and shear stresses at layer k, see Section 2.1 for their definitions; τ_x and τ_y are x and y components of shear force per horizontal area (Wu, 2007) at the layer interfaces of layer k, and they are defined by, e.g.,

$$\tau_x = \tau_{xz} - \tau_{xx}\frac{\partial z}{\partial x} - \tau_{xy}\frac{\partial z}{\partial y} \qquad (2.44)$$

It should be pointed out that the shear forces only exist at the free surface (e.g., wind force) and bed surface (e.g., friction force). In this work, we will not consider the wind effect on wave motions.

2.2.3   Layer integration of the vertical momentum equation

Since the vertical velocity w and the non-hydrostatic pressure q are located at the layer interface $z_{k+1/2}$, the vertical integration is carried out from z_k to z_{k+1}. Following Zijlema and Stelling (2005), we integrate the vertical momentum equation (2.26) by the Keller-Box scheme (Lam and Simpson, 1976). First of all, the vertical momentum equation is solved at layer interface $z_{k-1/2}$ and the non-hydrostatic pressure gradient is approximated through

the forward differencing scheme. Integration of the time derivative term is given by

$$\int_{z_{k-1}}^{z_k} \frac{\partial w}{\partial t}\,\mathrm{d}z = \frac{\partial (hw)_{k-1/2}}{\partial t} - w\frac{\partial z}{\partial t}\bigg|_{z_{k-1}}^{z_k} \approx \frac{\partial (hw)_{k-1/2}}{\partial t} \tag{2.45}$$

where the layer thickness centered at the layer interface $h_{k-1/2}$ is determined by $h_{k-1/2} = (h_k + h_{k-1})/2$. Note that the time derivative term $-w\frac{\partial z}{\partial t}\Big|_{z_{k-1}}^{z_k}$ is only available at the moving surfaces. The integration of the non-hydrostatic pressure gradient is given by

$$\int_{z_{k-1}}^{z_k} \frac{\partial q}{\partial z}\,\mathrm{d}z = q_{k+1/2} - q_{k-1/2} \tag{2.46}$$

As a result, the final momentum equation at $z_{k-1/2}$ is written as

$$\frac{\partial (hw)_{k-1/2}}{\partial t} = -\frac{1}{\rho}\left(q_{k+1/2} - q_{k-1/2}\right) \tag{2.47}$$

And then the vertical momentum equation is solved at layer interface $z_{k+1/2}$ with the non-hydrostatic pressure gradient approximated by the backward differencing scheme. It is directly given by

$$\frac{\partial (hw)_{k+1/2}}{\partial t} = -\frac{1}{\rho}\left(q_{k+1/2} - q_{k-1/2}\right) \tag{2.48}$$

Finally, we take the average of the discretized vertical momentum equations at $z_{k-1/2}$ and $z_{k+1/2}$ onto the layer k, resulting in

$$\frac{\partial (hw)_{k-1/2}}{\partial t} + \frac{\partial (hw)_{k+1/2}}{\partial t} = -\frac{2}{\rho}\left(q_{k+1/2} - q_{k-1/2}\right) \tag{2.49}$$

It is noted that the momentum equations (2.42) and (2.43) are formulated in term of the flux, and not the primary variables u and v. To obtain the conservation form of momentum equations for u and v, we multiply Equation (2.28) with u and v at the corresponding level z_k, and subtract these equations from Equations (2.42) and (2.43), respectively. And

then the reformulated horizontal momentum equations are given by

$$h_k \frac{\partial u_k}{\partial t} + \left[\frac{\partial (huu)_k}{\partial x} - u_k \frac{\partial (hu)_k}{\partial x} \right] + \left[\frac{\partial (huv)_k}{\partial y} - u_k \frac{\partial (hv)_k}{\partial y} \right] + \left(u_{k+1/2} w_{k+1/2} - u_{k-1/2} w_{k-1/2} \right) =$$
$$-gh_k \frac{\partial \eta}{\partial x} - \frac{1}{\rho} \left(\frac{\partial h_k q_k}{\partial x} - q \frac{\partial z}{\partial x} \Big|_{z_{k-1/2}}^{z_{k+1/2}} \right) + \left[\frac{\partial (hT_{xx})_k}{\partial x} + \frac{\partial (hT_{xy})_k}{\partial y} \right] + \frac{1}{\rho} \left[(\tau_x)_{k+1/2} - (\tau_x)_{k-1/2} \right]$$

$$(2.50)$$

$$h_k \frac{\partial v_k}{\partial t} + \left[\frac{\partial (huv)_k}{\partial x} - v_k \frac{\partial (hu)_k}{\partial x} \right] + \left[\frac{\partial (hvv)_k}{\partial y} - v_k \frac{\partial (hv)_k}{\partial y} \right] + \left(v_{k+1/2} w_{k+1/2} - v_{k-1/2} w_{k-1/2} \right) =$$
$$-gh_k \frac{\partial \eta}{\partial y} - \frac{1}{\rho} \left(\frac{\partial h_k q_k}{\partial y} - q \frac{\partial z}{\partial y} \Big|_{z_{k-1/2}}^{z_{k+1/2}} \right) + \left[\frac{\partial (hT_{yx})_k}{\partial x} + \frac{\partial (hT_{yy})_k}{\partial y} \right] + \frac{1}{\rho} \left[(\tau_y)_{k+1/2} - (\tau_y)_{k-1/2} \right]$$

$$(2.51)$$

It should be pointed out that the solution of the aforementioned governing equations does not rest on the choice of numerical methods (e.g., finite difference method or finite element method) at all.

2.3   Boundary Conditions

2.3.1   Free surface

This study doesn't consider the wind stress and the surface tension, so the atmospheric pressure boundary condition is assumed at the free surface.

2.3.2   Bottom

At the bottom, the effect of bed friction can be considered by using the Manning equation if necessary. The vertical velocity at the bed surface is computed by the bottom kinematic boundary condition with Equation (2.6).

2.3.3   Inlet

At the inlet, an incident normal velocity u_I is given based on the linear wave theory by

$$u_I = \frac{\omega f_r}{k(\eta_I - \zeta)} \eta_I \qquad (2.52)$$

22

where $\omega = 2\pi/T$ is the angular frequency of wave with T the wave period; $k = 2\pi/L$ is the wave number with L the wave length; η_I is the incident wave surface elevation, which is usually specified as a sinusoidal or a monochromatic wave in the case of regular waves; f_r is a ramp function used to prevent the initial short waves to have relatively large amplitudes (Stelling and Zijlema, 2003), it is defined by

$$f_r(t) = \frac{1}{2}\left(1 + \tanh\frac{t - 3T}{T}\right) \tag{2.53}$$

The non-hydrostatic pressure is assumed as zero at the inlet.

In addition, the solitary wave can also be specified at the inlet by providing either free surface elevation or velocity by

$$\eta(x,t) = \frac{A}{\cosh^2(kct)} \tag{2.54}$$

$$u(x,t) = \frac{\eta c}{\eta + h} \tag{2.55}$$

where A is the solitary wave height; h is the still water depth; g is the gravitational acceleration; η is the free surface elevation with reference to the still water level; the wave celerity c is defined by $\sqrt{g(A + h)}$; the wave number k is calculated by $\sqrt{3A/4h^3}$.

2.3.4 Outlet

At the outlet, the flow is assumed to be hydrostatic. To allow the waves to cross the outflow boundary without reflection, the Sommerfeld's radiation boundary condition is applied:

$$\frac{\partial f}{\partial x} + c\frac{\partial f}{\partial x} = 0 \tag{2.56}$$

where f can be either the water surface elevation or the velocity; c is the phase velocity defined as $c = \sqrt{gh}$.

Another technique for absorbing waves is the sponge layer boundary condition, which

requires an extension of computational domain by several wave lengths. It introduces a damping term with a coefficient λ in the momentum equation in the extended domain as

$$\frac{\partial u}{\partial t} + \cdots + \lambda u = 0 \tag{2.57}$$

the following sponge layer damping coefficient λ by Dingemans (1997) is adopted:

$$\lambda = \begin{cases} \frac{1}{4}\left(\tanh\left[\frac{\sin(\pi(4\hat{x}-1)/2)}{1-(4\hat{x}-1)^2}\right]+1\right), & 0 < \hat{x} < \frac{1}{2} \\ \\ \frac{1}{4}\left(\tanh\left[\frac{\sin(\pi(3-4\hat{x})/2)}{1-(3-4\hat{x})^2}\right]+1\right), & \frac{1}{2} < \hat{x} < 1 \end{cases} \tag{2.58}$$

where the dimensionless extended domain size is $\hat{x} = (x - L_0)/L_s$, with the sponge layer length L_s starting at $x = L_0$. It should be noted that the radiation boundary condition and the sponge layer technique can be combined if necessary.

At a closed wall, the free reflective condition is specified. In the case of a vertical wall parallel to y axis, the boundary condition is specified by

$$u = \frac{\partial v}{\partial x} = \frac{\partial w}{\partial x} = 0 \tag{2.59}$$

CHAPTER 3

DEPTH-INTEGRATED MODEL FOR WAVE PROPAGATION

In this chapter, a depth-integrated non-hydrostatic finite element model for simulating dynamic propagation of weakly dispersive waves is presented. Shallow water equations including extra non-hydrostatic pressure terms and a depth-integrated vertical momentum equation are solved with a linear distribution assumed in the vertical direction for the non-hydrostatic pressure and the vertical velocity. The model is developed based on the platform of a finite element free surface flow model, CCHE2D. And the depth-integrated non-hydrostatic wave model is solved semi-implicitly: the provisional flow velocity is first implicitly solved by using the shallow water equations; the non-hydrostatic pressure, which is implicitly obtained by ensuring a divergence-free velocity field, is used to correct the provisional velocity; finally the depth-integrated continuity equation is explicitly solved to satisfy global mass conservation. The developed wave model is verified by analytical solutions and validated by laboratory experiments, and the computed results show that the wave model can properly handle linear and nonlinear dispersive waves, wave shoaling, diffraction, refraction, and focusing.

In the following sections, the governing equations are introduced in Section 3.1, and the finite element method and the solution procedure of the wave model are illustrated in Section 3.2. Section 3.3 presents four benchmark cases to verify and validate the model. Major findings in this chapter are summarized in Section 3.4.

3.1 Governing Equations

The governing equations for the depth-integrated non-hydrostatic wave model in the non-conservation form are given as

$$\frac{\partial \eta}{\partial t} + \frac{\partial (HU)}{\partial x} + \frac{\partial (HV)}{\partial y} = 0 \tag{3.1}$$

$$\frac{\partial U}{\partial t} + U\frac{\partial U}{\partial x} + V\frac{\partial U}{\partial y} = -g\frac{\partial \eta}{\partial x} - \frac{1}{2\rho H}\left(H\frac{\partial q}{\partial x} + q\left(\frac{\partial \eta}{\partial x} + \frac{\partial \zeta}{\partial x}\right)\right) \tag{3.2}$$

$$\frac{\partial V}{\partial t} + U\frac{\partial V}{\partial x} + V\frac{\partial V}{\partial y} = -g\frac{\partial \eta}{\partial y} - \frac{1}{2\rho H}\left(H\frac{\partial q}{\partial y} + q\left(\frac{\partial \eta}{\partial y} + \frac{\partial \zeta}{\partial y}\right)\right) \tag{3.3}$$

$$\frac{DW}{Dt} = \frac{q}{\rho H} \tag{3.4}$$

where U, V, and W are the depth-integrated velocity components in the x, y, and z directions, respectively; q is the non-hydrostatic pressure at the bed surface; $\eta(x, y, t)$ is the free surface elevation; $\zeta(x, y)$ is the bed elevation; the water depth is defined by $H(x, y, t) = \eta(x, y, t) - \zeta(x, y)$. Since the distribution of vertical velocity is unknown, it is approximated by $W = (w_\eta + w_\zeta)/2$ (Walters, 2005; Yamazaki et al., 2008). Due to the introduction of the non-hydrostatic pressure and the incompressibility of fluids, the aforementioned governing equations are solved together with the continuity equation (2.1) (Casulli and Stelling, 1998; Stelling and Zijlema, 2003).

3.2 Finite Element Discretization

In this section, the governing equations are solved on the basis of the existing implicit finite element flow model, CCHE2D. The partially staggered grid configuration is first introduced, and then the finite element method and its differential operators are detailed, finally the numerical formulation for the wave model is elaborated.

3.2.1 Grid configuration

The existing hydrostatic finite element model CCHE2D (Jia and Wang, 1999, 2001; Jia et al., 2002) uses a partially staggered grid. The collocation grid is used for the momentum equations, and the pressure field (free surface elevation) is solved on the staggered grid. Therefore, the horizontal velocities U and V are located at collocation nodes. On the other hand, the vertical velocities W, w_η, and w_ς, the free surface elevation η, and the non-hydrostatic pressure q are located at staggered nodes, as illustrated in Figure 3.1. This partially staggered grid takes advantage of the simplicity of the collocation grid for computing velocity and that of the staggered grid to eliminate oscillation. Because separate grids are used for the velocity and the free surface elevation, additional finite element differential operators have to be computed for the staggered grid.
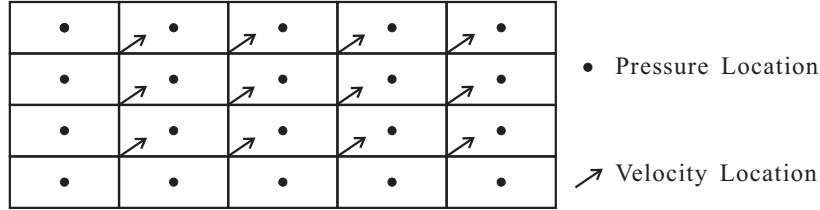
Figure 3.1. Definition sketch of the partially staggered grid used by CCHE2D.

3.2.2 Efficient Element Method

CCHE2D solves the NLSW equations with a special type of finite element method *Efficient Element Method* of Wang and Hu (1992). For clarity, some of the numerical details of this finite element based model are outlined.

In order to derive the interpolation function for a continuous variable f, the Taylor series expansion is applied to f in the neighborhood of $x = 0$ of a non-uniform one-dimensional (1D) element, the values of $f_1(x = -\Delta_1)$ and $f_3(x = \Delta_2)$ are approximated by

$$f_1 = f_2 - \frac{\mathrm{d}f}{\mathrm{d}x}\Delta_1 + \frac{1}{2}\frac{\mathrm{d}^2 f}{\mathrm{d}x^2}\Delta_1^2 \tag{3.5}$$

27

$$f_3 = f_2 + \frac{\mathrm{d}f}{\mathrm{d}x}\Delta_2 + \frac{1}{2}\frac{\mathrm{d}^2 f}{\mathrm{d}x^2}\Delta_2^2 \tag{3.6}$$

if $f_i(i = 1, 2, 3)$ are given, the derivatives $\frac{\mathrm{d}f}{\mathrm{d}x}$ and $\frac{\mathrm{d}^2 f}{\mathrm{d}x^2}$ can be calculated by Equations (3.5) and (3.6). A parabolic distribution of f in the physical space is constructed by the following quadratic interpolation function

$$f = \frac{1}{\Delta_1\Delta_2(\Delta_1 + \Delta_2)}\left[f_1\Delta_2 x(x - \Delta_2) - f_2(\Delta_1 + \Delta_2)(x + \Delta_1)(x - \Delta_2) + f_3\Delta_1 x(x + \Delta_1)\right] \tag{3.7}$$

To take advantage of the finite element method, one needs to find the interpolation function in terms of the coordinate in the logical space. For this purpose, a linear relationship between x and γ, the coordinate in the logical space, is assumed and according to Figure 3.2(a)

$$x = \Delta(\gamma + 1) - \Delta_1 \tag{3.8}$$

where $\Delta = (\Delta_1 + \Delta_2)/2$. The node in the logical space that corresponds to $x = 0$ in the physical space is $\gamma_0 = (\Delta_1 - \Delta_2)/(\Delta_1 + \Delta_2)$. The interpolation function defined in the logical space is obtained by substituting Equation (3.8) into Equation (3.7), one obtains

$$f = \varphi_1 f_1 + \varphi_2 f_2 + \varphi_3 f_3 \tag{3.9}$$

where

$$\varphi_1 = \frac{1}{2}\left(\frac{\Delta - \Delta_1}{\Delta_1} + \frac{\Delta}{\Delta_1}\gamma\right)(\gamma - 1)$$

$$\varphi_2 = -\frac{\Delta^2}{\Delta_1\Delta_2}\left(\gamma^2 - 1\right)$$

$$\varphi_3 = \frac{1}{2}\left(\frac{\Delta - \Delta_1}{\Delta_2} + \frac{\Delta}{\Delta_2}\gamma\right)(\gamma + 1)$$

Then the first-order derivative can be written as

$$\frac{\mathrm{d}f}{\mathrm{d}x} = \frac{\mathrm{d}}{\mathrm{d}x}\sum_{i=1}^{3}\varphi_i f_i = \sum_{i=1}^{3}\frac{\mathrm{d}}{\mathrm{d}x}\varphi_i f_i \tag{3.10}$$

Finally, the corresponding first-order differential operator is

$$\frac{\mathrm{d}}{\mathrm{d}x} = \sum_{i=1}^{3}\frac{\mathrm{d}}{\mathrm{d}x}\varphi_i \tag{3.11}$$

The interpolation function for the 2D finite element model is based on a nine-node quadrilateral element as shown in Figure 3.2(b), and it is constructed by using the 1D interpolation functions as

$$N_m = \varphi_i\varphi_j \ , \ \left(m = 1, 2, \cdots, 9; i = \mathrm{int}\left(\frac{m-1}{3}\right) + 1; j = m - 3(i-1)\right) \tag{3.12}$$

As pointed out by Jia and Wang (1999), the geometry of a physical element is in general irregular and asymmetric to the central node, and after the transformation into the logical space, it becomes very smooth and regular. The second-order interpolation function represents the physical geometry very well. The location of the central mesh node is transformed to the central node ($i = 2$, $j = 2$) in the logical space, which is in the position proportional to that in the physical space.
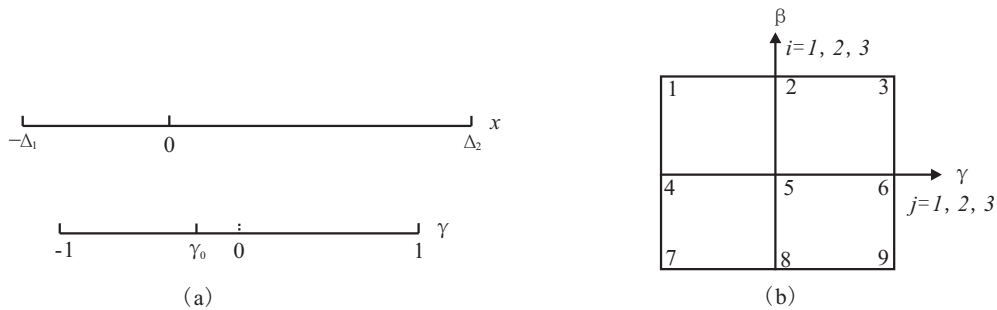
Figure 3.2. (a) Schematic sketch of 1D element in the physical and logical spaces; (b) Nine-node quadrilateral element in the logical space.

3.2.2.1   2D first and second order derivatives

In CCHE2D, the governing equations are solved in the physical space. Transformations are performed to obtain differential operators in the physical space, and then differential equations are converted to algebraic equation systems. The transformation of partial derivatives from the logical space to the physical space can be performed by using the following relation

$$\left\{ \begin{array}{c} \frac{\partial}{\partial x} \\ \frac{\partial}{\partial y} \end{array} \right\} = \frac{1}{D} \left[\begin{array}{cc} \frac{\partial y}{\partial \beta} & -\frac{\partial y}{\partial \gamma} \\ -\frac{\partial x}{\partial \beta} & \frac{\partial x}{\partial \gamma} \end{array} \right] \cdot \left\{ \begin{array}{c} \frac{\partial}{\partial \gamma} \\ \frac{\partial}{\partial \beta} \end{array} \right\} \tag{3.13}$$

where γ and β are the coordinates in the logical space corresponding to the coordinates x and y in the physical space, respectively. D is the determinant of transformation matrix:

$$D = \frac{\partial x}{\partial \gamma} \frac{\partial y}{\partial \beta} - \frac{\partial x}{\partial \beta} \frac{\partial y}{\partial \gamma} \tag{3.14}$$

The second-order finite element differential operators are given by

$$\frac{\partial^2}{\partial x^2} = \gamma_x^2 \frac{\partial^2}{\partial \gamma^2} + \beta_x^2 \frac{\partial^2}{\partial \beta^2} + 2\gamma_x \beta_x \frac{\partial^2}{\partial \gamma \partial \beta} \tag{3.15a}$$

$$\frac{\partial^2}{\partial y^2} = \gamma_y^2 \frac{\partial^2}{\partial \gamma^2} + \beta_y^2 \frac{\partial^2}{\partial \beta^2} + 2\gamma_y \beta_y \frac{\partial^2}{\partial \gamma \partial \beta} \tag{3.15b}$$

$$\frac{\partial^2}{\partial x \partial y} = \gamma_x \gamma_y \frac{\partial^2}{\partial \gamma^2} + \beta_x \beta_y \frac{\partial^2}{\partial \beta^2} + (\gamma_x \beta_y + \gamma_y \beta_x) \frac{\partial^2}{\partial \gamma \partial \beta} \tag{3.15c}$$

where

$$\left[\begin{array}{cc} \gamma_x & \beta_x \\ \gamma_y & \beta_y \end{array} \right] = \frac{1}{D} \left[\begin{array}{cc} \frac{\partial y}{\partial \beta} & -\frac{\partial y}{\partial \gamma} \\ -\frac{\partial x}{\partial \beta} & \frac{\partial x}{\partial \gamma} \end{array} \right]$$

The first-order derivatives obtained from Equation (3.13) do not take flow characteristics into account, because the interpolation functions are of Lagrangian, they are only related to mesh geometry. When a strongly advective flow is encountered, which is common for most open channel flows and coastal waves, these types of operators will cause node-to-node oscillations. To model physics more realistically, a physically bounded upwind scheme (Jia,

2013a,b) is used in this study. For all the non-advective physical phenomena, however, the operators in Equation (3.13) are capable of producing accurate results.

3.2.2.2 Four-node bilinear element
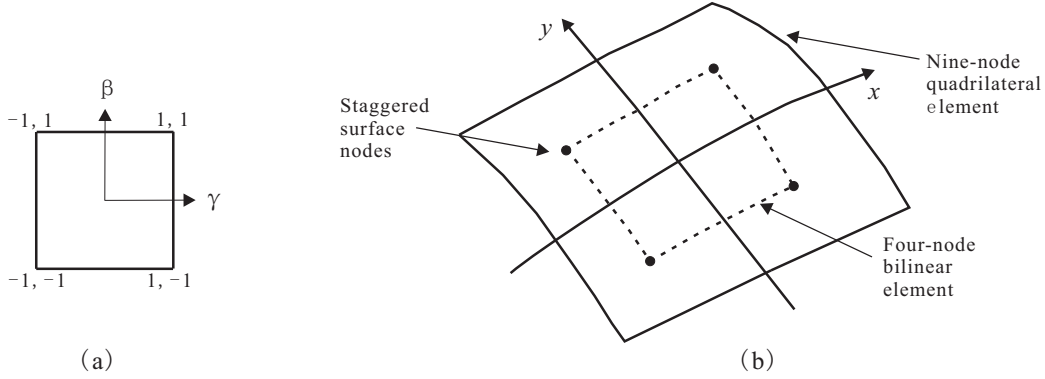
Figure 3.3. Definition sketch of the bilinear element for a collocation node: (a) logical space; (b) physical space.

Since the continuity equation is solved on the staggered grid, a four-node bilinear element is constructed to compute the pressure gradient at collocation nodes. Specifically, Figure 3.3 shows a four-node bilinear element which is centered at a collocation node used to calculate the free surface elevation and the non-hydrostatic pressure gradients when solving the momentum equations. Another set of four-node bilinear element, centered at a staggered node, is used to calculate flux gradient terms when solving the depth-integrated continuity equation. The first-order finite element differential operators based on the four-node bilinear element are computed in a way similar to those for the nine-node quadrilateral element. A classic interpolation function for this type of element is applied:

$$B_m = \frac{1}{4}(1 + \gamma\gamma_m)(1 + \beta\beta_m), (m = 1, 2, 3, 4) \tag{3.16}$$

The differential operators in the logical space are defined as derivatives of the interpolation

function as

$$\frac{\partial}{\partial\gamma} = \sum_{m=1}^{4} \frac{\partial B_m}{\partial\gamma} \tag{3.17a}$$

$$\frac{\partial}{\partial\beta} = \sum_{m=1}^{4} \frac{\partial B_m}{\partial\beta} \tag{3.17b}$$

Once the finite element differential operators in the logical space are obtained, the differential operators in the physical space can be easily calculated by the transformation equation (3.13).

3.2.2.3 Summary of finite element operators

Previous two subsections derived the finite element differential operators in detail. In summary, this study uses three kinds of differential operators defined in the physical space as follows (x_i or $x_j, i = 1, 2$ and $j = 1, 2$, are used to represent the coordinate axes (x, y) for simplicity in this section).

(1) Differential operators based on the nine-node quadrilateral element:

$$\frac{\partial}{\partial x_i} = \sum_{m=1}^{9} \frac{\partial N_m}{\partial x_i} \tag{3.18a}$$

$$\frac{\partial^2}{\partial x_i \partial x_j} = \sum_{m=1}^{9} \frac{\partial^2 N_m}{\partial x_i \partial x_j} \tag{3.18b}$$

(2) Differential operators based on the four-node bilinear element:

$$\frac{\partial}{\partial x_i} = \sum_{m=1}^{4} \frac{\partial B_m}{\partial x_i} \tag{3.19}$$

(3) Differential operators for advection terms based on the nine-node quadrilateral element:

$$\frac{\partial^u}{\partial x_i} = \sum_{m=1}^{9} \frac{\partial N_m^u}{\partial x_i} \tag{3.20a}$$

$$\frac{\partial^v}{\partial x_i} = \sum_{m=1}^{9} \frac{\partial N_m^v}{\partial x_i} \tag{3.20b}$$

where superscripts u and v indicate the differential operators computed for advection terms in the u and v momentum equations, respectively, because the interpolation functions for advection terms are related to velocity distributions.

3.2.3   Numerical method

In this study, the computation is accomplished in several steps similar to those used by Walters (2005) and Yamazaki et al. (2008). In the first step, the momentum equations without non-hydrostatic pressure terms are implicitly solved for the provisional velocity; in the second step, a Poisson equation formulated by the continuity equation is implicitly solved for the non-hydrostatic pressure, which is immediately used to correct the provisional velocity; finally the depth-integrated continuity equation is explicitly solved to update the free surface elevation for global mass conservation.
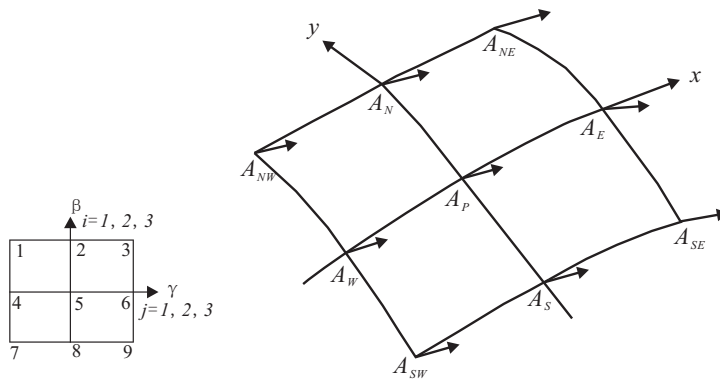
Figure 3.4. Notation of the algebraic equation for an element in the physical space.

3.2.3.1   First step

In the first step, the provisional velocities $\tilde{U}$ and $\tilde{V}$ are solved implicitly by the following momentum equations without considering the non-hydrostatic pressure terms

$$\frac{\partial U}{\partial t} + U\frac{\partial U}{\partial x} + V\frac{\partial U}{\partial y} = -g\frac{\partial \eta}{\partial x} \tag{3.21}$$

$$\frac{\partial V}{\partial t} + U\frac{\partial V}{\partial x} + V\frac{\partial V}{\partial y} = -g\frac{\partial \eta}{\partial y} \tag{3.22}$$

By using the finite element differential operators introduced in Section 3.2.2, the above equations are discretized as

$$\frac{\tilde{U}^{n+1} - U_5^n}{\Delta t} + U_5^n \sum_{m=1}^{9} \frac{\partial N_m^u \tilde{U}_m^{n+1}}{\partial x} + V_5^n \sum_{m=1}^{9} \frac{\partial N_m^u \tilde{U}_m^{n+1}}{\partial y} = -g \sum_{m=1}^{4} \frac{\partial B_m^c \eta_m^n}{\partial x} \tag{3.23}$$

$$\frac{\tilde{V}^{n+1} - V_5^n}{\Delta t} + U_5^n \sum_{m=1}^{9} \frac{\partial N_m^v \tilde{V}_m^{n+1}}{\partial x} + V_5^n \sum_{m=1}^{9} \frac{\partial N_m^v \tilde{V}_m^{n+1}}{\partial y} = -g \sum_{m=1}^{4} \frac{\partial B_m^c \eta_m^n}{\partial y} \tag{3.24}$$

where U^n and V^n are velocity solutions at the previous time step and n denotes the time level; the superscript c indicates that the four-node bilinear element differential operator is used to calculate the free surface elevation gradients at collocation nodes using the free surface elevations at surrounding staggered nodes; the subscript m is the nodal index in either the four-node bilinear element or the nine-node quadrilateral element, hereafter.

Since the information along two mesh lines (γ, β) passing the center of the element is dominant, and coefficients at the four corners of the nine-node quadrilateral element are usually very small, a five-diagonal algebraic equation system is therefore used. The notation of the algebraic equation is shown in Figure 3.4, and the final algebraic equation for $\tilde{U}^{n+1}$ is assembled as

$$A_{uP}\tilde{U}_P^{n+1} + A_{uW}\tilde{U}_W^{n+1} + A_{uE}\tilde{U}_E^{n+1} + A_{uN}\tilde{U}_N^{n+1} + A_{uS}\tilde{U}_S^{n+1} = S_u \tag{3.25}$$

where

$$A_{uP} = 1 + \Delta t U_5^n \frac{\partial N_5^u}{\partial x} + \Delta t V_5^n \frac{\partial N_5^u}{\partial y}$$

$$A_{uW} = \Delta t U_4^n \frac{\partial N_4^u}{\partial x} + \Delta t V_4^n \frac{\partial N_4^u}{\partial y}$$

$$A_{uE} = \Delta t U_6^n \frac{\partial N_6^u}{\partial x} + \Delta t V_6^n \frac{\partial N_6^u}{\partial y}$$

$$A_{uN} = \Delta t U_2^n \frac{\partial N_2^u}{\partial x} + \Delta t V_2^n \frac{\partial N_2^u}{\partial y}$$

$$A_{uS} = \Delta t U_8^n \frac{\partial N_8^u}{\partial x} + \Delta t V_8^n \frac{\partial N_8^u}{\partial y}$$

$$S_u = U_5^n - \Delta t U_5^n \sum_{m=1,3,7,9} \frac{\partial N_m^u U_m^n}{\partial x} - \Delta t V_5^n \sum_{m=1,3,7,9} \frac{\partial N_m^u U_m^n}{\partial y} - \Delta t g \sum_{m=1}^{4} \frac{\partial B_m^c \eta_m^n}{\partial x}$$

Similarly, the algebraic equation for $\tilde{V}^{n+1}$ is

$$A_{vP} \tilde{V}_P^{n+1} + A_{vW} \tilde{V}_W^{n+1} + A_{vE} \tilde{V}_E^{n+1} + A_{vN} \tilde{V}_N^{n+1} + A_{vS} \tilde{V}_S^{n+1} = S_v \qquad (3.26)$$

where

$$A_{vP} = 1 + \Delta t U_5^n \frac{\partial N_5^v}{\partial x} + \Delta t V_5^n \frac{\partial N_5^v}{\partial y}$$

$$A_{vW} = \Delta t U_4^n \frac{\partial N_4^v}{\partial x} + \Delta t V_4^n \frac{\partial N_4^v}{\partial y}$$

$$A_{vE} = \Delta t U_6^n \frac{\partial N_6^v}{\partial x} + \Delta t V_6^n \frac{\partial N_6^v}{\partial y}$$

$$A_{vN} = \Delta t U_2^n \frac{\partial N_2^v}{\partial x} + \Delta t V_2^n \frac{\partial N_2^v}{\partial y}$$

$$A_{vS} = \Delta t U_8^n \frac{\partial N_8^v}{\partial x} + \Delta t V_8^n \frac{\partial N_8^v}{\partial y}$$

$$S_v = V_5^n - \Delta t U_5^n \sum_{m=1,3,7,9} \frac{\partial N_m^v V_m^n}{\partial x} - \Delta t V_5^n \sum_{m=1,3,7,9} \frac{\partial N_m^v V_m^n}{\partial y} - \Delta t g \sum_{m=1}^{4} \frac{\partial B_m^c \eta_m^n}{\partial y}$$

3.2.3.2 Second step

In the second step, a Poisson equation is formulated by the momentum equations (3.2), (3.3), (3.4), and the bottom kinematic boundary condition (2.6), and it is implicitly solved for the non-hydrostatic pressure. The final velocity field is updated with the non-hydrostatic pressure.

The bottom kinematic boundary condition (2.6) is approximated by the provisional velocities as

$$w_\zeta^{n+1} = \bar{\tilde{U}}^{n+1} \sum_{m=1}^{4} \frac{\partial B_m^s \zeta_m}{\partial x} + \bar{\tilde{V}}^{n+1} \sum_{m=1}^{4} \frac{\partial B_m^s \zeta_m}{\partial y} \tag{3.27}$$

where $\bar{\tilde{U}}$ and $\bar{\tilde{V}}$ are the provisional horizontal velocities at a staggered node, they are interpolated from the provisional velocities at surrounding collocation nodes by the inverse distance weighting method; the superscript s indicates that the four-node bilinear element differential operator is used to calculate the gradient at a staggered node using information at surrounding collocation nodes.

In the vertical momentum equation (3.4), the non-hydrostatic pressure is determined by the depth-integrated vertical velocity, which is approximated by the vertical velocities at the free surface and the bed as $W = (w_\eta + w_\zeta)/2$. With this approximation, the vertical momentum equation becomes

$$w_\eta^{n+1} = w_\eta^n - w_\zeta^{n+1} + w_\zeta^n + \frac{2\Delta t q^{n+1}}{\rho H^n} \tag{3.28}$$

Comparing Equations (3.2) and (3.3) with Equations (3.21) and (3.22), the final horizontal velocities influenced by the non-hydrostatic pressure can be expressed as

$$U^{n+1} = \tilde{U}^{n+1} - \frac{\Delta t}{2\rho H^n} \left(H^n \frac{\partial q^{n+1}}{\partial x} + q^{n+1} \left(\frac{\partial \eta^n}{\partial x} + \frac{\partial \zeta}{\partial x} \right) \right) \tag{3.29}$$

$$V^{n+1} = \tilde{V}^{n+1} - \frac{\Delta t}{2\rho H^n} \left(H^n \frac{\partial q^{n+1}}{\partial y} + q^{n+1} \left(\frac{\partial \eta^n}{\partial y} + \frac{\partial \zeta}{\partial y} \right) \right) \tag{3.30}$$

36

To obtain a well-coupled solution of the velocity field and the non-hydrostatic pressure, the continuity equation (2.1) is directly applied for a depth-averaged water column (Stelling and Zijlema, 2003; Walters, 2005; Yamazaki et al., 2008) as

$$H^n \left(\frac{\partial U^{n+1}}{\partial x} + \frac{\partial V^{n+1}}{\partial y} \right) + \left(w_\eta^{n+1} - w_\zeta^{n+1} \right) = 0 \qquad (3.31)$$

Substitution of Equations (3.27), (3.28), (3.29), and (3.30) into the continuity equation (3.31) gives a Poisson equation for the non-hydrostatic pressure, and the discretized Poisson equation is in the form of a five-diagonal algebraic equation system as follows:

$$A_P q_P^{n+1} + A_W q_W^{n+1} + A_E q_E^{n+1} + A_N q_N^{n+1} + A_S q_S^{n+1} = S_q \qquad (3.32)$$

where

$$A_P = \frac{\Delta t}{2\rho} H^n \left(\frac{\partial^2 N_5}{\partial x^2} + \frac{\partial^2 N_5}{\partial y^2} \right) + \frac{\Delta t}{2\rho} \left(\frac{\partial N_5}{\partial x} \cdot grad_x + \frac{\partial N_5}{\partial y} \cdot grad_y \right) - \frac{2\Delta t}{\rho H^n}$$

$$A_W = \frac{\Delta t}{2\rho} H^n \left(\frac{\partial^2 N_4}{\partial x^2} + \frac{\partial^2 N_4}{\partial y^2} \right) + \frac{\Delta t}{2\rho} \left(\frac{\partial N_4}{\partial x} \cdot grad_x + \frac{\partial N_4}{\partial y} \cdot grad_y \right)$$

$$A_E = \frac{\Delta t}{2\rho} H^n \left(\frac{\partial^2 N_6}{\partial x^2} + \frac{\partial^2 N_6}{\partial y^2} \right) + \frac{\Delta t}{2\rho} \left(\frac{\partial N_6}{\partial x} \cdot grad_x + \frac{\partial N_6}{\partial y} \cdot grad_y \right)$$

$$A_N = \frac{\Delta t}{2\rho} H^n \left(\frac{\partial^2 N_2}{\partial x^2} + \frac{\partial^2 N_2}{\partial y^2} \right) + \frac{\Delta t}{2\rho} \left(\frac{\partial N_2}{\partial x} \cdot grad_x + \frac{\partial N_2}{\partial y} \cdot grad_y \right)$$

$$A_S = \frac{\Delta t}{2\rho} H^n \left(\frac{\partial^2 N_8}{\partial x^2} + \frac{\partial^2 N_8}{\partial y^2} \right) + \frac{\Delta t}{2\rho} \left(\frac{\partial N_8}{\partial x} \cdot grad_x + \frac{\partial N_8}{\partial y} \cdot grad_y \right)$$

$$S_q = H^n \left(\sum_{m=1}^{4} \frac{\partial B_m^s \tilde{U}_m^{n+1}}{\partial x} + \sum_{m=1}^{4} \frac{\partial B_m^s \tilde{V}_m^{n+1}}{\partial y} \right) + \left(w_\eta^n - 2w_\zeta^{n+1} + w_\zeta^n \right)$$
$$- \frac{\Delta t}{2\rho} H^n \left(\sum_{m=1,3,7,9} \frac{\partial^2 N_m q_m^n}{\partial x^2} + \sum_{m=1,3,7,9} \frac{\partial^2 N_m q_m^n}{\partial y^2} \right)$$
$$- \frac{\Delta t}{2\rho} \left(\sum_{m=1,3,7,9} \frac{\partial N_m q_m^n}{\partial x} \cdot grad_x + \sum_{m=1,3,7,9} \frac{\partial N_m q_m^n}{\partial y} \cdot grad_y \right)$$

Two constants in these coefficients are calculated by

$$grad_x = \sum_{m=1}^{4} \frac{\partial B_m^s (\eta_c^n)_m}{\partial x} + \sum_{m=1}^{4} \frac{\partial B_m^s \zeta_m}{\partial x} \tag{3.33a}$$

$$grad_y = \sum_{m=1}^{4} \frac{\partial B_m^s (\eta_c^n)_m}{\partial y} + \sum_{m=1}^{4} \frac{\partial B_m^s \zeta_m}{\partial y} \tag{3.33b}$$

where η_c, the free surface elevation at a collocation node, is interpolated from the free surface elevations at surrounding staggered nodes by the inverse distance weighting method. It is worth mentioning that although the free surface elevation η in Equation (3.33) and the bed elevation ζ in Equations (3.27) and (3.33) can be located at staggered nodes and the first-order differential operators in Equation (3.18a) can be used for the gradient approximation, when steep free surface elevation gradient and rapidly varying topography cases are considered, numerical tests showed that the four-node bilinear element differential operator gave a more stable solution with the free surface elevation and the bed elevation defined at surrounding collocation nodes.

Once the non-hydrostatic pressure is solved by Equation (3.32), the vertical velocity at free surface w_η and the horizontal velocities U, V are corrected by the non-hydrostatic pressure using Equations (3.28), (3.29), and (3.30), respectively.

3.2.3.3 Third step

In the last step, the free surface elevation is computed by the mass conservation equation (3.1) using the updated horizontal velocities by

$$\eta^{n+1} = \eta^n - \Delta t \left(\sum_{m=1}^{4} \frac{\partial B_m^s (H_c^n U^{n+1})_m}{\partial x} + \sum_{m=1}^{4} \frac{\partial B_m^s (H_c^n V^{n+1})_m}{\partial y} \right) \tag{3.34}$$

where H_c^n, the water depth at a collocation node, is interpolated from water depths at surrounding staggered nodes by the inverse distance weighting method.

3.2.3.4 Matrix solver

Compared with a previous depth-integrated non-hydrostatic model developed by Yamazaki et al. (2008), this model not only solves the non-hydrostatic pressure implicitly, but also the depth-integrated horizontal velocities. Because the governing equations are discretized on the basis of a structured grid, the final algebraic equation system is in the form of a five-diagonal matrix, which is efficiently solved by Stone's Strongly Implicitly Procedure (Stone, 1968).

3.3 Model Verification and Validation

In this section, we verify and validate the correctness and accuracy of the depth-integrated non-hydrostatic wave model by four benchmark cases. The first case demonstrates the importance of the non-hydrostatic pressure by simulating a standing wave oscillation in a closed basin. The second case is a solitary wave propagation along a constant water depth channel, since the solitary wave is not a solution of the NLSW equations, this case verifies the correct non-hydrostatic property of the wave model. The third case is regular wave propagation over a submerged bar, validating the model's capability for handling wave nonlinearity. The last case addresses wave propagation over an elliptic shoal on a sloped bottom, examining the ability of the model to simulate wave refraction, diffraction, and focusing over a varying topography in the coastal zone.

3.3.1 Standing wave oscillation in a closed basin

The first case is a standing short wave oscillation in a 2D vertical closed basin, the objective of this test is to show the importance of the non-hydrostatic pressure when a case involves the vertical velocity component. A standing wave in an 80 m long closed basin with water depth of 10 m is considered. Initially, the free surface elevation is given by

$$\eta(x) = a\cos\left(\frac{\pi x}{40}\right),\ 0 \le x \le 80 \tag{3.35}$$

where a is the standing wave amplitude, $a = 0.05$ m is used in this study. The wave length is equal to the basin length, and the water depth parameter $kH = \pi/4$. According to the linear wave theory, the wave period is $T \approx 8.84$ s. In the numerical simulation, the closed basin is discretized with mesh sizes $\Delta x = \Delta y = 1$ m and the total simulation time is one wave period with time step $\Delta t = 0.01$ s. Comparison of numerical results and analytical solutions is presented in Figure 3.5. The hydrostatic model, which is not able to consider the variation of flow field in the vertical direction, gives prediction with a significant wave damping even in one wave period. On the other hand, numerical results with the non-hydrostatic pressure match with analytical solutions very well. It could be concluded that the non-hydrostatic model, with only one-layer, can properly simulate the vertical structure of flows.
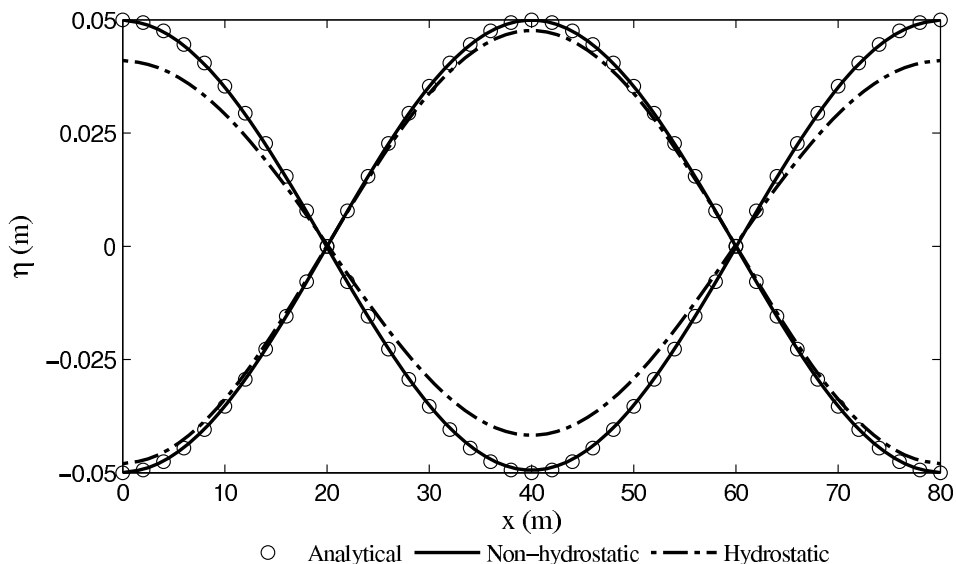
Figure 3.5. Comparison of simulated standing wave profiles with analytical solutions at $t = T/2$ and $t = T$.

3.3.2 Solitary wave propagation along a constant water depth channel

The solitary wave is a nonlinear wave with a finite amplitude, if the fluid is inviscid and the horizontal bottom is frictionless, the wave should maintain the shape and velocity during the propagation process. This case has been used to verify several non-hydrostatic models (e.g., Stelling and Zijlema, 2003; Zijlema and Stelling, 2005; Walters, 2005; Yamazaki

et al., 2008). In this study, we consider an 800 m long frictionless channel with a still water depth $h = 10$ m. The radiation boundary condition is specified at both inlet and outlet. The solitary wave is initially located at $x_0 = 100$ m with wave height $A = 2$ m. Mesh sizes are $\Delta x = \Delta y = 0.5$ m and the time step is $\Delta t = 0.025$ s, the Courant number in terms of wave celerity $Cr = \Delta t \sqrt{gh}/\Delta x \approx 0.5$. Analytical solutions of the free surface elevation and the horizontal velocity are given by

$$\eta(x,t) = \frac{A}{\cosh^2\left(k(x - x_0 - ct)\right)} \tag{3.36}$$

$$u(x,t) = \frac{\eta c}{\eta + h} \tag{3.37}$$

where the wave celerity $c = \sqrt{g(A + h)}$ and the wave number $k = \sqrt{3A/4h^3}$.

In Figure 3.6, the comparison of numerical results and analytical solutions of the time series of free surface elevations at two locations ($x = 100$ m and 200 m) are presented. Wave evolving processes are accurately predicted by the model. Figure 3.7 shows the initial solitary wave and the simulated waveforms along the channel at 10 s, 20 s, 30 s, and 40 s. There is a slight reduction of wave height at the beginning of simulation due to the initial condition approximated by the analytical solution, similar phenomena were reported by Walters (2005) and Yamazaki et al. (2008). Although minor trailing waves are observed, the wave shape and amplitude are well conserved during the simulation.

3.3.3 Regular wave propagation over a submerged bar

Beji and Battjes (1993) and Luth et al. (1994) conducted physical experiments of regular wave propagation over a submerged trapezoidal bar in a 37.7 m long, 0.8 m wide, and 0.75 m deep wave flume. Figure 3.8 shows the numerical setup of the experiment, the still water depth is 0.4 m, a 0.3 m high trapezoidal bar with an offshore slope 1:20 and a shoreward slope 1:10 is set between 6.0 m and 17.0 m in the flume, eight wave gauges were used to measure the free surface elevation. Incident waves with amplitude 1.0 cm and wave period
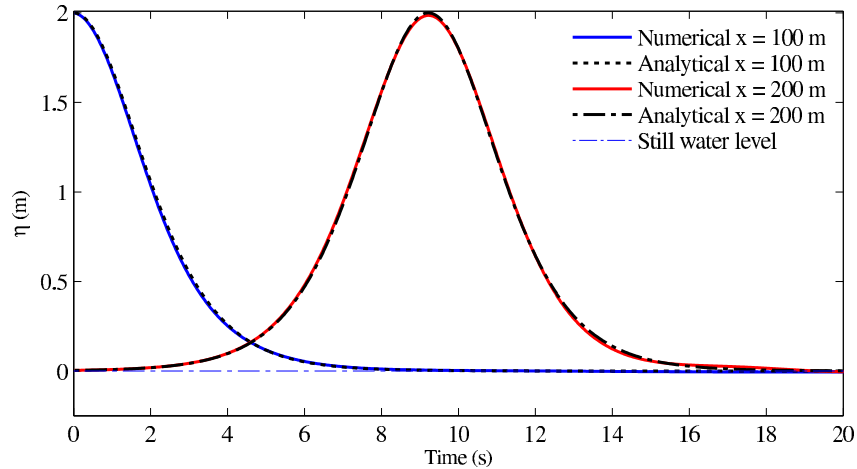
Figure 3.6. Comparison of numerical results and analytical solutions of time series of free surface elevations at $x = 100$ m and $x = 200$ m.
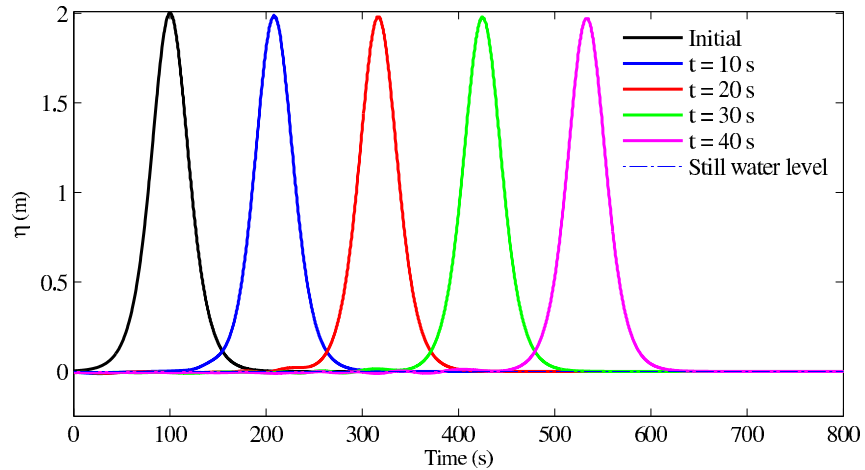
Figure 3.7. Simulated waveforms as the wave propagates at different simulation time steps.

2.02 s, corresponding to the water depth parameter $kH \approx 0.67$, are generated at the left side based on the linear wave theory. The wave absorber of the experiment, a 1:25 plane beach with coarse material at the right side, is modeled by an open flow area with the radiation boundary condition imposed (Stelling and Zijlema, 2003; Yamazaki et al., 2008). In the experiment, higher harmonics were generated during wave propagation over the offshore side of bar, and they accumulated as waves propagate over the horizontal crest, finally these higher harmonics were released as the water depth increases in the shoreward side (Beji and Battjes, 1993, 1994). This experiment has been widely used to investigate nonlinear and dispersive
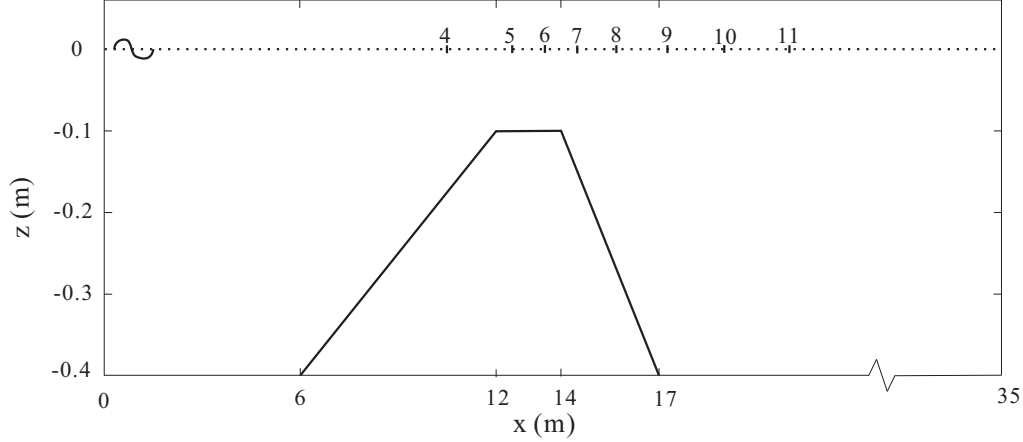
Figure 3.8. Numerical model setup of regular wave propagation over a submerged bar.

properties for both Boussinesq-type and non-hydrostatic wave models (e.g., Beji and Battjes, 1994; Casulli and Stelling, 1998; Stelling and Zijlema, 2003; Walters, 2005; Yamazaki et al., 2008; Roeber et al., 2010). In this study, the 35 m long computational domain is discretized with mesh sizes $\Delta x = \Delta y = 1.25$ cm. At the very beginning, the velocity and the free surface elevation are zero at all nodes; a small time step, e.g., $\Delta t = 0.001$ s is used to initiate wave smoothly with a ramp function. Once the waves are well formed in the computation domain, the time step is gradually increased to save computation time; because the free surface elevation is explicitly solved with Equation (3.34) in this model, the maximum time step is still controlled by a maximum Courant number $Cr = 0.5$.

Comparison of simulated and measured free surface elevations is shown in Figure 3.9. Wave shoaling process on the offshore side of bar (Gauges 4 and 5) and wave transformation from a low frequency dispersion zone (Gauge 6) to a high frequency dispersion zone (Gauge 8) are well predicted by this depth-integrated non-hydrostatic model. However, noticeable discrepancies appear between simulated and measured free surface elevations over the flat bottom behind the bar (Gauges 9, 10, and 11), where higher harmonics are released. A spectral analysis (Roeber et al., 2010) has showed that the water depth parameter kH ranges from 6 to 10 in this zone, these high dispersive waves are out of the applicable range of depth-integrated non-hydrostatic models (Walters, 2005; Yamazaki et al., 2008).
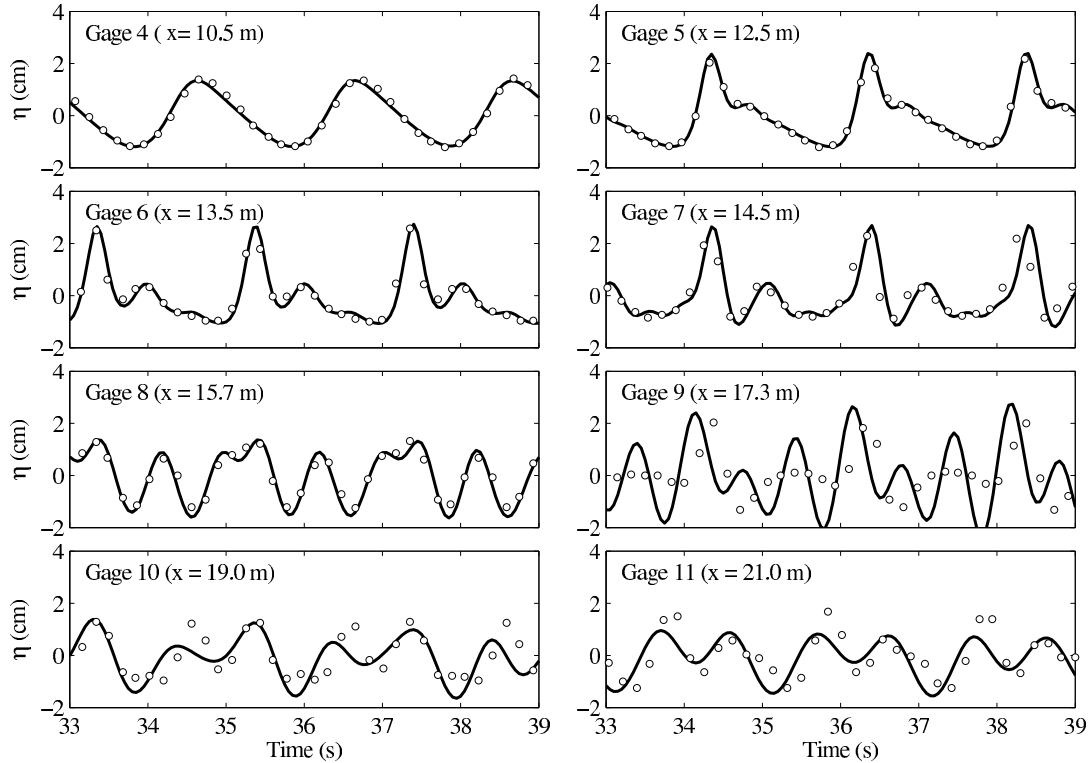
Figure 3.9. Comparison of simulated and measured free surface elevations at eight wave gauges. Experimental data (circles), numerical results (solid lines).

However, compared with the performance of the numerical model based on the classical Boussinesq equations (e.g., Beji and Battjes, 1994), our model produces slightly better results for those weakly dispersive waves (Gauges 7 and 8). Thanks to the physically bounded upwind scheme (Jia, 2013a,b), the simulated free surface elevations are still within a very reasonable range even at a highly dispersive wave zone.

3.3.4 Regular wave propagation over an elliptic shoal on sloped bottom

The last case is to test the model's capability of simulating wave refraction, diffraction, and focusing caused by wave propagation over a 3D uneven bottom. Numerical results are compared with experimental data from Berkhoff et al. (1982), in which regular wave propagation over an elliptic shoal located on a plane slope 1:50 was considered. This experiment has also been widely used to validate Boussinesq-type and non-hydrostatic wave models (e.g., Zijlema and Stelling, 2008; Stelling and Zijlema, 2003; Wei et al., 1999; Li and

44
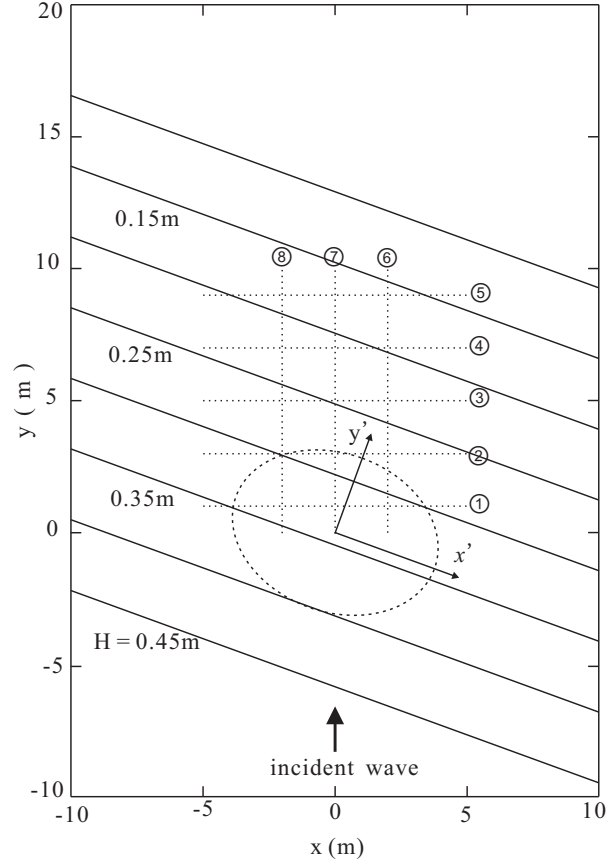
Figure 3.10. Bottom configuration corresponding to the experimental setup of Berkhoff et al. (1982).

Fleming, 2001; Yuan and Wu, 2004; Cui et al., 2012; Ma et al., 2012).

Figure 3.10 shows the bottom configuration of the experiment. A local coordinate system (x', y') is set at the elliptic shoal center, and it is related to the (x, y) coordinate system by means of rotation over $-20°$. The still water depth without the shoal is given in meters by

$$
H = \begin{cases}
0.45, & y' < -5.484 \\
\\
\max(0.10, 0.45 - 0.02(5.484 + y')), & y' \geq -5.484
\end{cases}
\tag{3.38}
$$

At the end of domain, the minimum water depth is 10 cm. The shape of the elliptic shoal is

45

given by

$$\left(\frac{x'}{4}\right)^2 + \left(\frac{y'}{3}\right)^2 = 1 \tag{3.39}$$

and the thickness of the shoal is

$$d = -0.3 + 0.5\sqrt{1 - \left(\frac{x'}{5}\right)^2 - \left(\frac{y'}{3.75}\right)^2} \tag{3.40}$$

Regular waves with wave height $h_0 = 4.64$ cm and wave period 1.0 s, corresponding to the water depth parameter $kH \approx 1.9$, are specified at the lower boundary based on the linear wave theory. At the end of the computational domain, the sponge layer boundary condition with a sponge layer length $L_s = 5$ m is employed to minimize wave reflection. The reflective wall boundary condition is assigned to both lateral walls. Mesh sizes in x and y directions are set to be $\Delta x = 0.1$ m and $\Delta y = 0.05$ m, respectively. The total simulation time is 35 s, and the time step setting strategy is the same as the previous test case.
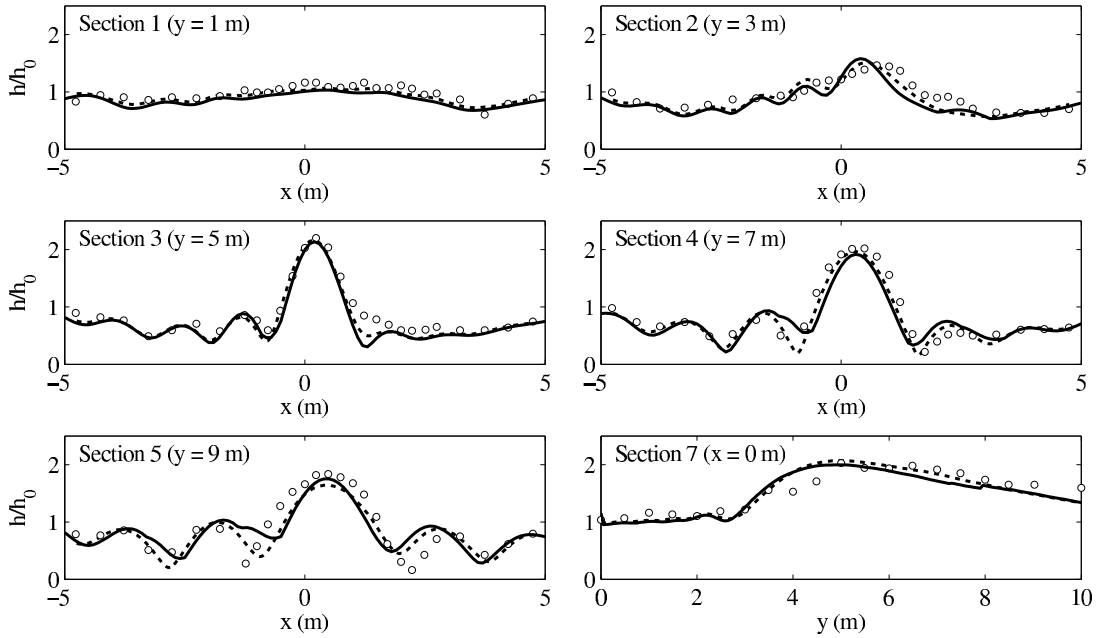
Figure 3.11. Comparison of simulated and measured relative wave heights at six cross sections. Experimental data (circles), numerical results (solid lines), SWASH (dotted lines).

This experiment with the same boundary condition and initial condition is also simulated by SWASH (Zijlema et al., 2011) using the depth-integrated mode and the MINMOD limiter for correcting water depth at velocity nodes (Stelling and Duinmeijer, 2003). Figure 3.11 shows the comparison of simulated and measured relative wave heights (h/h_0) at five transverse sections ($y =$1, 3, 5, 7, and 9 m) and one longitudinal section ($x = 0$ m). The simulated wave height by numerical models is obtained by taking the difference between the maximum and the minimum free surface elevations over the final five wave periods when the simulated wave form is permanent (Stelling and Zijlema, 2003). Due to the irregular topography, wave refraction, diffraction, and focusing are formed as the waves pass by the elliptic shoal. At the cross section 1, the waves propagate just over half of the elliptical shoal, the model slightly underpredicts the shoaling effect. At the cross section 2, only a minor discrepancy of wave height along x direction is observed, consistent with the numerical results in other studies (e.g., Wei et al., 1999; Li and Fleming, 2001; Stelling and Zijlema, 2003; Yuan and Wu, 2004; Ma et al., 2012). Wave focusing occurs behind the shoal with the maximum relative wave heights about 2.2, 2.0, and 1.7 at cross sections 3, 4, and 5, respectively, this model and SWASH give very similar predictions at the cross section 3, SWASH model shows a better maximum wave height prediction at the cross section 4, while this model captures the maximum wave height slightly better at the cross section 5. The cross section 7 represents wave focusing along the longitudinal section ($x = 0$ m), and both models give reasonable predictions. The capability of handling wave refraction, diffraction, and focusing is thus confirmed by this test case. It should be mentioned that SWASH gives slightly better predictions to the lower wave height distributions area at cross sections 4 and 5, which may be attributed to different numerical formulations implemented by two models.

3.4   Chapter Summary

In this chapter, a depth-integrated non-hydrostatic finite element wave model has been developed. The total pressure is decomposed into hydrostatic and non-hydrostatic

components, and the governing equations are solved in several steps. The hydrostatic component of this model is the existing depth-integrated finite element flow model, CCHE2D, which efficiently solves the NLSW equations using a partially staggered grid to eliminate the check-board oscillation. The newly developed non-hydrostatic component takes advantage of the incompressibility of fluids and solves the non-hydrostatic pressure implicitly.

Several benchmark tests were carried out to verify and validate the depth-integrated non-hydrostatic wave model. The capability of the model is equivalent to that of numerical models based on the classical Boussinesq-type equations for weakly dispersive waves, and it is evident that this model can properly handle the linear and nonlinear dispersive waves, wave shoaling, refraction, diffraction, and focusing. Because the hydrostatic platform, CCHE2D, is a generalized flow solver, the developed non-hydrostatic wave model can be applied to study real-life nearshore wave processes with minor modifications. In the future, the wave model will be enhanced by a wetting and drying algorithm for simulating wave run-up, a momentum conservation scheme for handling wave breaking, and a multi-layer technique for modeling highly dispersive waves.

CHAPTER 4

DEPTH-INTEGRATED MODEL FOR NEARSHORE WAVE PROCESSES

This chapter presents CCHE2D-NHWAVE, a depth-integrated non-hydrostatic finite element model for simulating nearshore wave processes. The governing equations are a depth-integrated vertical momentum equation and the shallow water equations including extra non-hydrostatic pressure terms, which enable the model to simulate relatively short wave motions, where both frequency dispersion and nonlinear effects play important roles. A special type of finite element method, which was previously developed for a well-validated depth-integrated free surface flow model CCHE2D, is used to solve the governing equations on a partially staggered grid using a pressure projection method. To resolve discontinuous flows, involving breaking waves and hydraulic jumps, a momentum conservation advection scheme is developed based on the partially staggered grid. Besides, the model is implemented with a simple but efficient wetting and drying algorithm to deal with the moving shoreline. The model is first verified by analytical solutions, and then validated by a series of laboratory experiments. The comparison shows that the developed wave model without the use of any empirical parameters is capable of accurately simulating a wide range of nearshore wave processes, including propagation, breaking, and run-up of nonlinear dispersive waves and transformation and inundation of tsunami waves.

In the following sections, the governing equations are reviewed in Section 4.1. Numerical formulation and solution procedure are described in Section 4.2. Next a series of analytical solutions and laboratory experiments are used to verify and validate the wave model in Section 4.3. Finally, conclusions for this work are drawn in Section 4.4.

49

4.1 Governing Equations

The depth-integrated governing equations in the conservation form have been derived in detail in Chapter 2, and they are directly given as follows

$$\frac{\partial H}{\partial t} + \frac{\partial (HU)}{\partial x} + \frac{\partial (HV)}{\partial y} = 0 \tag{4.1}$$

$$H\frac{\partial U}{\partial t} + \frac{\partial (HUU)}{\partial x} - U\frac{\partial (HU)}{\partial x} + \frac{\partial (HUV)}{\partial y} - U\frac{\partial (HV)}{\partial y} = -gH\frac{\partial \eta}{\partial x}$$
$$- \frac{1}{2\rho}\left(H\frac{\partial q}{\partial x} + q\left(\frac{\partial \eta}{\partial x} + \frac{\partial \zeta}{\partial x}\right)\right) - \frac{gn^2 U}{H^{1/3}}\sqrt{U^2 + V^2} + \left(\frac{\partial (HT_{xx})}{\partial x} + \frac{\partial (HT_{xy})}{\partial y}\right) \tag{4.2}$$

$$H\frac{\partial V}{\partial t} + \frac{\partial (HUV)}{\partial x} - V\frac{\partial (HU)}{\partial x} + \frac{\partial (HVV)}{\partial y} - V\frac{\partial (HV)}{\partial y} = -gH\frac{\partial \eta}{\partial y}$$
$$- \frac{1}{2\rho}\left(H\frac{\partial q}{\partial y} + q\left(\frac{\partial \eta}{\partial y} + \frac{\partial \zeta}{\partial y}\right)\right) - \frac{gn^2 V}{H^{1/3}}\sqrt{U^2 + V^2} + \left(\frac{\partial (HT_{yx})}{\partial x} + \frac{\partial (HT_{yy})}{\partial y}\right) \tag{4.3}$$

$$\frac{DW}{Dt} = \frac{q}{\rho H} \tag{4.4}$$

where U, V, and W are the depth-integrated velocity components in the x, y, and z directions, respectively; q is the non-hydrostatic pressure at the bed surface; $\eta(x, y, t)$ is the free surface elevation; $\zeta(x, y)$ is the bed elevation; the water depth is defined by $H(x, y, t) = \eta(x, y, t) - \zeta(x, y)$; n is the Manning roughness coefficient; T_{xx}, T_{xy}, T_{yx}, and T_{yy} are the depth-integrated normal and shear stresses (normalized by the water density), and their definitions are referred to Chapter 2.

4.2 Numerical Formulation and Solution

In this section, we discretize and solve the governing equations with the finite element method as presented in Chapter 3. In order to simulate wave breaking correctly, a momentum conservation scheme built on top of the partially staggered grid for the advection terms discretization is first presented, and then the pressure projection method of Stelling and Zijlema (2003) is employed to solve the momentum equations. Next, the free surface elevation is obtained by an explicit solution of the depth-integrated continuity equation. Finally, we

present a wetting and drying algorithm to deal with the moving shoreline.

4.2.1 Momentum conservation scheme for the advection terms discretization

As CCHE2D solves the governing equations in the physical space, the finite element differential operators are usually first constructed in the logical space, and then transformed back to the physical space. On the other hand, similar to other numerical models, the governing equations can also be directly solved on the physical space. In this section, the momentum conservation scheme is introduced based on the physical space.
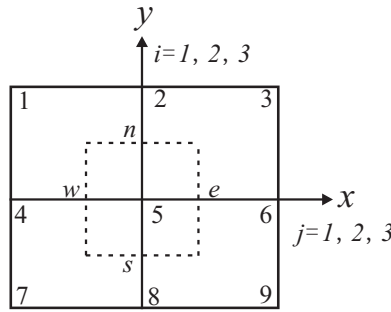
Figure 4.1. Control volume for momentum conservation scheme.

Figure 4.1 shows a control volume centered at a velocity node in the physical space. First of all, the flux at the interface is calculated by a simple central difference scheme (Zijlema and Stelling, 2005). At the interface e, it gives

$$Q_e^u = \frac{1}{2}(Q_5^u + Q_6^u) \tag{4.5}$$

where the flux terms $Q_5^u = HU_5$ and $Q_6^u = HU_6$ are calculated at collocation nodes. Other flux terms at the interfaces (Q_w^u, Q_n^v and Q_s^v) can be calculated accordingly.

In terms of approximation of the advection velocity $\hat{U}$ at the control volume interfaces, two different methods are implemented according to the interface location. (1), at the interfaces normal to the velocity direction (western and eastern interfaces for $\hat{U}$), their values are approximated by a one-side second-order upwind scheme (Zijlema and Stelling, 2008),

51

e.g., if the flux Q_e^u is positive at the interface e:

$$\hat{U}_e = \frac{3}{2}U_5 - \frac{1}{2}U_4 \tag{4.6}$$

(2), at the interfaces parallel to the velocity direction (northern and southern interfaces for $\hat{U}$), due to the lack of horizontal fluxes (i.e., Q_n^u and Q_s^u) at these interfaces, the above upwind scheme is not applicable anymore. The advection velocities are simply approximated by a central difference scheme, e.g.,

$$\hat{U}_n = \frac{1}{2}(U_2 + U_5) \tag{4.7}$$

Similarly, the advection velocity $\hat{V}$ can be obtained by the same method.

Once the advection velocity and flux are obtained, the advection terms are ready to be discretized in a control volume fashion. The advection terms in Equations (4.2) and (4.3) are first grouped as

$$ADV_x = \frac{\partial\left(HUU\right)}{\partial x} - U\frac{\partial(HU)}{\partial x} + \frac{\partial\left(HUV\right)}{\partial y} - U\frac{\partial(HV)}{\partial y} \tag{4.8}$$

$$ADV_y = \frac{\partial\left(HUV\right)}{\partial x} - V\frac{\partial(HU)}{\partial x} + \frac{\partial\left(HVV\right)}{\partial y} - V\frac{\partial(HV)}{\partial y} \tag{4.9}$$

At a typical node as shown in Figure 4.1, the x component in Equation (4.8) can be discretized as

$$\frac{\partial\left(HUU\right)}{\partial x} - U\frac{\partial(HU)}{\partial x} = \frac{Q_e^u\hat{U}_e - Q_w^u\hat{U}_w}{\Delta x} - U_5\frac{Q_e^u - Q_w^u}{\Delta x} \tag{4.10}$$

with the flux at the interface approximated by the averaged flux values of its neighboring collocation nodes by, e.g., Equation (4.5), Equation (4.10) can be further written as

$$\frac{\partial\left(HUU\right)}{\partial x} - U\frac{\partial(HU)}{\partial x} = \frac{U_5 - \hat{U}_w}{2\Delta x}Q_4^u + \frac{\hat{U}_e - \hat{U}_w}{2\Delta x}Q_5^u + \frac{\hat{U}_e - U_5}{2\Delta x}Q_6^u \tag{4.11}$$

similarly, the y component in Equation (4.8) can be discretized as

$$\frac{\partial\left(HUV\right)}{\partial y} - U\frac{\partial(HV)}{\partial y} = \frac{\hat{U}_n - U_5}{2\Delta y}Q_2^v + \frac{\hat{U}_n - \hat{U}_s}{2\Delta y}Q_5^v + \frac{U_5 - \hat{U}_s}{2\Delta y}Q_8^v \qquad (4.12)$$

The same method is applied to discretize the advection terms in Equation (4.9), and it gives

$$\frac{\partial\left(HUV\right)}{\partial x} - V\frac{\partial(HU)}{\partial x} = \frac{V_5 - \hat{V}_w}{2\Delta x}Q_4^u + \frac{\hat{V}_e - \hat{V}_w}{2\Delta x}Q_5^u + \frac{\hat{V}_e - V_5}{2\Delta x}Q_6^u \qquad (4.13)$$

$$\frac{\partial\left(HVV\right)}{\partial y} - V\frac{\partial(HV)}{\partial y} = \frac{\hat{V}_n - V_5}{2\Delta y}Q_2^v + \frac{\hat{V}_n - \hat{V}_s}{2\Delta y}Q_5^v + \frac{V_5 - \hat{V}_s}{2\Delta y}Q_8^v \qquad (4.14)$$

The above finite difference discretization using the control volume variables for the advection terms guarantees that the momentum is conserved. As a result, the model is able to simulate wave breaking without the use of any empirical parameters, as to be shown in Section 4.3.

4.2.2 Numerical procedures

To solve the velocity by utilizing the pressure projection method of Stelling and Zijlema (2003), one should first determine the non-hydrostatic pressure. For this purpose, the horizontal momentum equations (4.2) and (4.3) are semi-discretized as follows

$$\begin{aligned} H^n\frac{U^{n+1} - U^n}{\Delta t} + ADV_x^n = &-gH^n\frac{\partial\eta^n}{\partial x} - \frac{H^n}{2\rho}\frac{\partial q^{n+1}}{\partial x} - \frac{q^{n+1}}{2\rho}\left(\frac{\partial\eta^n}{\partial x} + \frac{\partial\zeta}{\partial x}\right) \\ &-\frac{gn^2}{(H^n)^{1/3}}U^n\sqrt{(U^n)^2 + (V^n)^2} + \left(\frac{\partial(HT_{xx})^n}{\partial x} + \frac{\partial(HT_{xy})^n}{\partial y}\right) \end{aligned} \qquad (4.15)$$

$$\begin{aligned} H^n\frac{V^{n+1} - V^n}{\Delta t} + ADV_y^n = &-gH^n\frac{\partial\eta^n}{\partial y} - \frac{H^n}{2\rho}\frac{\partial q^{n+1}}{\partial y} - \frac{q^{n+1}}{2\rho}\left(\frac{\partial\eta^n}{\partial y} + \frac{\partial\zeta}{\partial y}\right) \\ &-\frac{gn^2}{(H^n)^{1/3}}V^n\sqrt{(U^n)^2 + (V^n)^2} + \left(\frac{\partial(HT_{yx})^n}{\partial x} + \frac{\partial(HT_{yy})^n}{\partial y}\right) \end{aligned} \qquad (4.16)$$

where ADV_x^n and ADV_y^n are the discretized advection terms using the finite difference scheme introduced in Section 4.2.1.

Since the distribution of the vertical velocity is unknown, it is assumed to be linear, and the depth-integrated vertical velocity is approximated by $W = (w_\eta + w_\zeta)/2$ (Walters, 2005; Yamazaki et al., 2008). With this assumption, the vertical velocity at the free surface is calculated by the vertical momentum equation (4.4) by

$$w_\eta^{n+1} = w_\eta^n - w_\zeta^{n+1} + w_\zeta^n + \frac{2\Delta t q^{n+1}}{\rho H^n} \tag{4.17}$$

Meanwhile, the vertical velocity at the bed surface is computed by using the bottom kinematic boundary condition (2.6):

$$w_\zeta^{n+1} = \bar{U}^n \sum_{m=1}^{4} \frac{\partial B_m^s \zeta_m}{\partial x} + \bar{V}^n \sum_{m=1}^{4} \frac{\partial B_m^s \zeta_m}{\partial y} \tag{4.18}$$

where $\bar{U}^n$ and $\bar{V}^n$ are previous time level velocity solutions at a staggered node, and they are interpolated from velocities at the surrounding collocation nodes by the inverse distance weighting method; the superscript s indicates that the four-node bilinear element differential operator is used to calculate the gradient at a staggered node using information at surrounding collocation nodes.

Because of the assumption of fluid incompressibility, there is no explicit equation (e.g., Equation of State) for the pressure. Under this circumstance, the non-hydrostatic pressure is calculated through the condition that the velocity field is divergence-free (Casulli and Stelling, 1998; Stelling and Zijlema, 2003). In the case of a depth-integrated formulation, the divergence-free velocity field condition requires

$$H^n \left(\frac{\partial U^{n+1}}{\partial x} + \frac{\partial V^{n+1}}{\partial y} \right) + \left(w_\eta^{n+1} - w_\zeta^{n+1} \right) = 0 \tag{4.19}$$

Substitution of Equations (4.15), (4.16), (4.17), and (4.18) into Equation (4.19) gives a Poisson equation for the non-hydrostatic pressure at the new time level. Due to the structured grid, the discretized Poisson equation is of a five-diagonal linear algebraic equation system,

which can be efficiently solved by the Strong Implicitly Procedure (Stone, 1968). The algebraic equation system for q^{n+1} is similar to the one presented in Chapter 3. Readers are referred to it for details.

Once the non-hydrostatic pressure q^{n+1} is obtained, the vertical velocity at the free surface w_η^{n+1} is updated by Equation (4.17), and the horizontal velocities U^{n+1} and V^{n+1} are calculated by the following discretized momentum equations

$$
\begin{aligned}
H_c^n \frac{U^{n+1} - U^n}{\Delta t} + ADV_x^n &= -gH_c^n \sum_{m=1}^4 \frac{\partial B_m^c \eta_m^n}{\partial x} \\
&- \frac{H_c^n}{2\rho} \sum_{m=1}^4 \frac{\partial B_m^c q_m^{n+1}}{\partial x} - \frac{q^{n+1}}{2\rho} \left(\sum_{m=1}^4 \frac{\partial B_m^c \eta_m^n}{\partial x} + \sum_{m=1}^4 \frac{\partial B_m^c \zeta_m}{\partial x} \right) \\
&- \frac{gn^2 U^{n+1}}{(H_c^n)^{1/3}} \sqrt{(U^n)^2 + (V^n)^2} + \left(\sum_{m=1}^9 \frac{\partial N_m (HT_{xx})_m^n}{\partial x} + \sum_{m=1}^9 \frac{\partial N_m (HT_{xy})_m^n}{\partial x} \right)
\end{aligned}
\tag{4.20}
$$

$$
\begin{aligned}
H_c^n \frac{V^{n+1} - V^n}{\Delta t} + ADV_y^n &= -gH_c^n \sum_{m=1}^4 \frac{\partial B_m^c \eta_m^n}{\partial y} \\
&- \frac{H_c^n}{2\rho} \sum_{m=1}^4 \frac{\partial B_m^c q_m^{n+1}}{\partial y} - \frac{q^{n+1}}{2\rho} \left(\sum_{m=1}^4 \frac{\partial B_m^c \eta_m^n}{\partial y} + \sum_{m=1}^4 \frac{\partial B_m^c \zeta_m}{\partial y} \right) \\
&- \frac{gn^2 V^{n+1}}{(H_c^n)^{1/3}} \sqrt{(U^n)^2 + (V^n)^2} + \left(\sum_{m=1}^9 \frac{\partial N_m (HT_{yx})_m^n}{\partial y} + \sum_{m=1}^9 \frac{\partial N_m (HT_{yy})_m^n}{\partial y} \right)
\end{aligned}
\tag{4.21}
$$

where H_c is the water depth at a collocation node, and it is interpolated from water depths at the surrounding staggered nodes by the inverse distance weighting method; the superscript c indicates the four-node bilinear element differential operator is used to calculate the gradient at a collocation node using information from the surrounding staggered nodes. It is different from the semi-discretized Equations (4.15) and (4.16) that the friction terms in the above equations are treated implicitly to improve numerical stability.

Up to this point, the horizontal velocity solution is only first-order accuracy in time, it is well-known that the first-order scheme suffers from numerical diffusion, which may bring

unwanted wave damping into the solution. To improve the accuracy, a defect correction method (Zijlema et al., 2011) using the advection terms is further implemented to correct the horizontal velocities, e.g., U^{n+1} by

$$U^{n+1} = U^{n+1} - \frac{\Delta t}{H_c^n} \left(\frac{\hat{U}_e^*}{2\Delta x} Q_6^u + \frac{\hat{U}_e^* - \hat{U}_w^*}{2\Delta x} Q_5^u - \frac{\hat{U}_w^*}{2\Delta x} Q_4^u \right) \tag{4.22}$$

where $\hat{U}_e^*$ and $\hat{U}_w^*$ are the advection velocity corrections at the interfaces, e.g., $\hat{U}_e^*$ is calculated by

$$\hat{U}_e^* = \begin{cases} \frac{1}{2} \psi_{r-} \left(U_6^n - U_{6e}^{n+1} \right), & Q_e^n < 0 \\ \\ \frac{1}{2} \psi_{r+} \left(U_5^{n+1} - U_4^n \right), & Q_e^n \geq 0 \end{cases} \tag{4.23}$$

where ψ_{r-} and ψ_{r+} are the flux limiters, the Superbee limiter (Hirsch, 2007) is used, and U_{6e} denotes the (unshown) eastern neighbor of the node 6 in Figure 4.1.

In this study, the bed is assumed fixed, so the depth-integrated continuity equation (4.1) can also be written in terms of the free surface elevation by

$$\frac{\partial \eta}{\partial t} + \frac{\partial (HU)}{\partial x} + \frac{\partial (HV)}{\partial y} = 0 \tag{4.24}$$

as a result, the solution of the free surface elevation is obtained by the following discretization form of Equation (4.24) as

$$\eta^{n+1} = \eta^n - \Delta t \left(\sum_{m=1}^{4} \frac{\partial B_m^s (\hat{H}_c^n U^{n+1})_m}{\partial x} + \sum_{m=1}^{4} \frac{\partial B_m^s (\hat{H}_c^n V^{n+1})_m}{\partial y} \right) \tag{4.25}$$

Because of the partially staggered grid configuration, the water depth at a collocation node $(\hat{H}_c)$ in Equation (4.25) is not uniquely defined. Following Stelling and Duinmeijer (2003), a first-order upwind scheme is adapted to determine the water depth at collocation nodes. In Figure 4.2, a collocation node is surrounded by four cells and each of them is centered at a staggered node, and therefore, the water depth at a collocation node is simply copied from
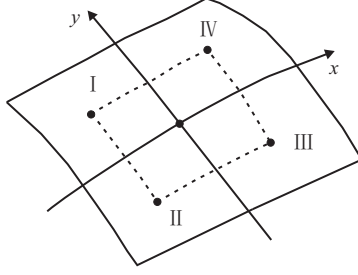
Figure 4.2. Schematic sketch of the water depth calculation at a collocation node using a first-order upwind method.

the water depth at the staggered node (H_s) in the upwind direction. The basic rules can be summarized as follows

(1) If the water flows into Zone I, $\hat{H}_c = H_s^{III}$;

(2) If the water flows into Zone II, $\hat{H}_c = H_s^{IV}$;

(3) If the water flows into Zone III, $\hat{H}_c = H_s^{I}$;

(4) If the water flows into Zone IV, $\hat{H}_c = H_s^{II}$;

where the superscripts (i.e., I, II, III, and IV) denote the water depth (H_s) at the corresponding zones. As demonstrated by Stelling and Duinmeijer (2003), Zijlema and Stelling (2008) and Zijlema et al. (2011), the water depth H_s^n is non-negative at every time step if the time step is chosen to satisfy the following condition

$$\Delta t < \min \left\{ \Delta x / U^n, \ \Delta y / V^n \right\} \tag{4.26}$$

Equation (4.26) implies that the flooding never happens faster than one grid size per time step. For this reason, no complicated wetting and drying algorithms are needed. To improve the computation efficiency, the model will not solve the momentum equation for the velocity field when $\hat{H}_c$ is lower than a threshold value (5×10^{-4} m is used in this study).

4.3   Model Verification and Validation

In this section, the model described above is verified and validated by several bench-
mark cases. The first three cases with analytical solutions examine the correctness of non-
hydrostatic pressure implementation, the efficiency of the wetting and drying algorithm, and
the well-balanced property of the model, respectively. And then the following four sets of
laboratory experiments whose wave and flow features (e.g., wave breaking and run-up) are
expected to be encountered in the nearshore zone are used to evaluate the model's capability
for nearshore wave processes modeling.

4.3.1   Solitary wave propagation along a constant depth channel

A standard benchmark case to verify the dispersion characteristics for Boussinesq-
type and non-hydrostatic models is the propagation of a solitary wave along a frictionless
channel with a constant water depth (e.g., Casulli and Stelling, 1998; Stelling and Zijlema,
2003; Roeber et al., 2010). To conserve the wave amplitude and speed, the numerical model
must handle nonlinearity and frequency dispersion correctly. In this study, we consider an
800 m long frictionless channel with a still water depth $h = 10$ m. The radiation boundary
condition is specified at both inlet and outlet, and the initial solitary wave is located at
$x_0 = 200$ m with an initial height $A = 2$ m. The analytical solutions of the free surface
elevation, the horizontal velocity, and the vertical velocity at the free surface are given by

$$\eta(x,t) = \frac{A}{\cosh^2\left(k(x - x_0 - ct)\right)} \tag{4.27}$$

$$u(x,t) = \frac{\eta c}{\eta + h} \tag{4.28}$$

$$w_s(x,t) = -z\frac{\partial u}{\partial x} \tag{4.29}$$

where the wave celerity $c = \sqrt{g(A+h)}$ and the wave number $k = \sqrt{3A/4h^3}$.

In the numerical simulation, mesh sizes are $\Delta x = \Delta y = 0.5$ m and the time step is
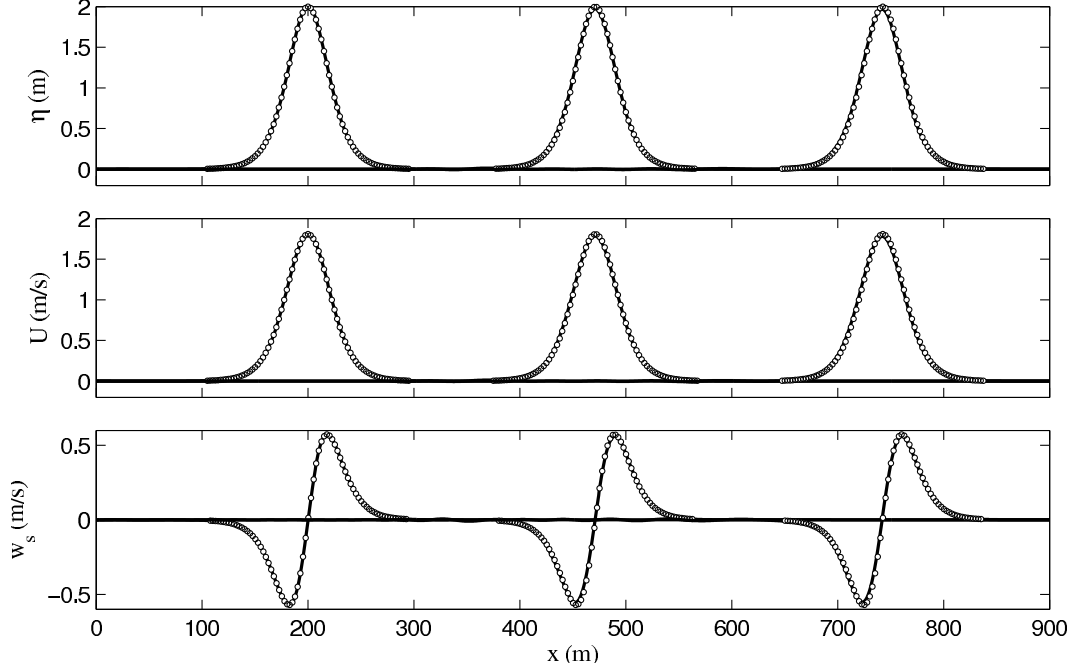
Figure 4.3. Comparison of numerical results and analytical solutions of free surface elevations (top panel), horizontal velocities (middle panel), and vertical velocities at the free surface (bottom panel) at t=0, 25, and 50 s. Analytical solutions (circles), numerical results (solid lines).

$\Delta t = 0.005$ s. Figure 4.3 shows the comparison of numerical results and analytical solutions of free surface elevations, horizontal velocities, and vertical velocities at t = 0 s, 25 s, and 50 s. Excellent agreements with the analytical solution have been obtained for all variables. Especially, the vertical velocity at the free surface is determined by the non-hydrostatic pressure using Equation (4.17), good agreement of the vertical velocity profile indicates that the non-hydrostatic pressure has been well simulated by the depth-integrated model. With this case, the non-hydrostatic property of the model is therefore verified.

4.3.2   Parabolic flood wave propagation over a dry bed

Thacker (1981) derived several exact solutions of the NLSW equations by taking into account different initial conditions and domain geometries, these cases have been widely used to verify wetting and drying algorithms of numerical models (e.g., Kroon, 2009; Zijlema et al., 2011). In this study, we consider a 2D parabolic mound of water spreading over a frictionless

horizontal surface. The analytical solution of the parabolic flood wave surface elevation is

$$\eta(x, y, t) = A \left(\frac{T^2}{t^2 + T^2} - \frac{x^2 + y^2}{R_0^2} \left(\frac{T^2}{t^2 + T^2} \right)^2 \right) \tag{4.30}$$

where A and R_0 are the initial height and the initial radius of water mass, respectively. Following Kroon (2009), $A = 0.5$ m and $R_0 = \sqrt{10}$ m are used. Besides, $T = R_0 / \sqrt{2gA}$ is the time corresponding to the central height reduced to $A/2$.

In the numerical simulation, we consider a 15 m × 15 m domain, which is discretized by mesh sizes $\Delta x = \Delta y = 0.1$ m, and the numerical time step is $\Delta t = 0.005$ s. Figure 4.4 presents the comparison of numerical results and analytical solutions of free surface elevations during the parabolic flood wave propagation process. Although steep gradients exist at the wetting and drying interfaces and the flooding process happens in a very fast way, numerical results still match with the analytical solution fairly well, no spurious free surface elevations are observed. And therefore, the efficiency of the wetting and drying algorithm is validated.
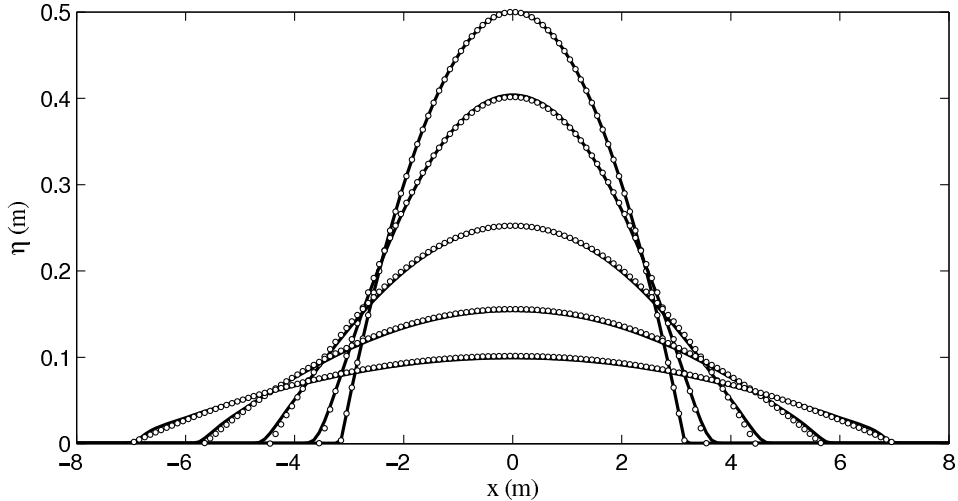
Figure 4.4. Comparison of numerical results and analytical solutions of free surface elevations at t=0, 0.5, 1.0, 1.5, and 2.0 s. Analytical solutions (circles), numerical results (solid lines).

4.3.3 Preservation of still water surface at a surface-piercing hump

The well-balanced criteria require a numerical model to preserve a still free surface elevation in a frictionless flow over a varying bathymetry. Liang and Marche (2009) presented a numerical model verification case with still water level at a surface-piercing hump involving wetting and drying interfaces. Inside a 1.0 m long frictionless closed basin, a hump with the bed elevation defined by

$$\zeta(x) = \max\left(0, 0.25 - 5(x - 0.5)^2\right) \tag{4.31}$$

is located at the center of the basin. The initial free surface elevation is given by $\eta(x) = \max\left(0.1, \zeta(x)\right)$, resulting in two wetting and drying interfaces near the hump.

In the numerical simulation, the domain is discretized with 100 cells with the wall boundary condition specified at both ends, and the time step is $\Delta t = 0.005$ s. It is found that the water surface remains tranquil during the simulation time 200 s, and there is no spurious phenomenon observed near the wetting and drying interfaces as shown in Figure 4.5.
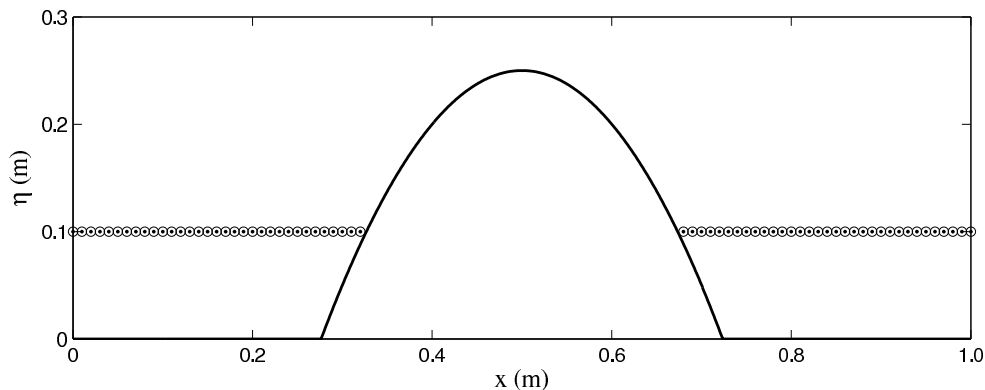
Figure 4.5. Comparison of numerical results and analytical solutions of the free surface elevation at t=200 s. Analytical solutions (dots), bed profile (solid line), numerical results (circles).

4.3.4 Regular wave propagation over an elliptic shoal

The Berkhoff Shoal case (Berkhoff et al., 1982), in which regular wave propagation over an elliptic shoal located on a 1:50 plane slope, has become an accepted test case for validating Boussinesq-type and non-hydrostatic models' capability of simulating wave refraction, diffraction, and focusing (e.g., Wei et al., 1999; Zijlema and Stelling, 2008). For this test, we not only evaluate the model's performance of predicting nonlinear dispersive wave transformation, but also we demonstrate that the defect correction method is able to reduce wave damping caused by numerical diffusion. This case has been used to validate the previous wave propagation model presented in Chapter 3, readers are referred to it for the bottom configuration.

In the numerical simulation, incident waves with wave height $h_0 = 4.64$ cm and wave period 1.0 s, corresponding to the water depth parameter $kH \approx 1.9$, are specified at the offshore boundary based on the linear wave theory. At the end of the computational domain, a sponge layer boundary condition with 5 m width is employed to minimize wave reflection. The reflective boundary condition is assigned to both lateral walls. Mesh sizes in x and y directions are set to be $\Delta x = 0.1$ m and $\Delta y = 0.05$ m, respectively. The total simulation time is 35 s, and the time step is $\Delta t = 0.01$ s.

Figure 4.6 shows the comparison of simulated and measured relative wave heights at six cross sections. First of all, in all cross sections the numerical model with the defect correction method gives much better predictions than the one without this method, these improvements confirm the importance of the defect correction method for reducing numerical diffusion. From now on, we compare the results produced by the defect correction method with experimental data. At the cross section 1, the waves just propagate over half of the shoal, relative wave heights are slightly underpredicted. Due to the irregular topography, wave diffraction, refraction, and focusing are formed at the lee side of the shoal. At the cross section 2, the model gives a minor discrepancy along x direction, which was also reported by other studies (e.g., Stelling and Zijlema, 2003; Ma et al., 2012). At cross sections 3, 4,
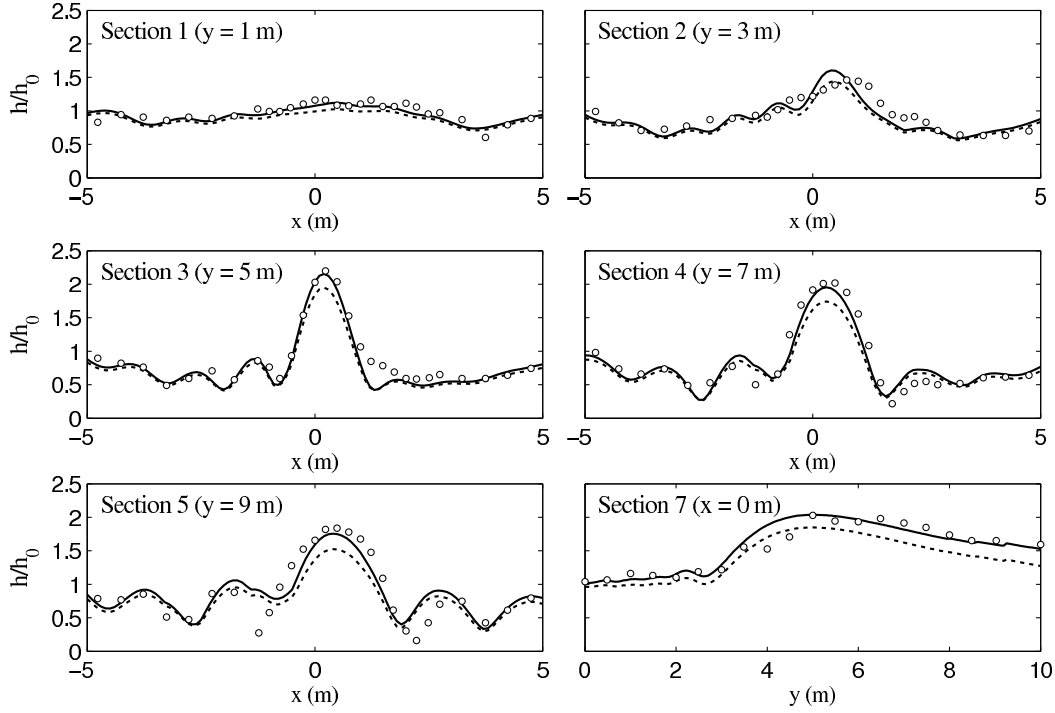
Figure 4.6. Comparison of simulated and measured relative wave heights at six cross sections. Experimental data(circles), numerical results with the defect correction method (solid lines), numerical results without the defect correction method (dotted lines).

and 5, wave focusing becomes pronounced, the numerical model captures the maximum wave height at the cross section 3 very well, and gives reasonable predictions at cross sections 4 and 5. Finally the cross section 7 shows wave focusing profile computed by the model in the longitudinal direction. Compared with the numerical results computed by an extended Boussinesq equations model (Wei et al., 1999) and multi-layer non-hydrostatic models (e.g., Zijlema and Stelling, 2008; Ai et al., 2010; Ma et al., 2012), It is noticed that our model is able to properly predict the peak of wave focusing, but slightly overpredicts the secondary peaks as presented at cross sections 4 and 5, see also the numerical results in Chapter 3. This is due to the fact that the capabilities of depth-integrated non-hydrostatic models (e.g., Stelling and Zijlema, 2003; Walters, 2005; Yamazaki et al., 2008) are comparable with or slightly better than those of numerical models based on the classical Boussinesq equations for weakly dispersive waves. When relatively highly dispersive waves are considered, a better dispersion relation or more layers in the vertical direction should be implemented. At last,

63
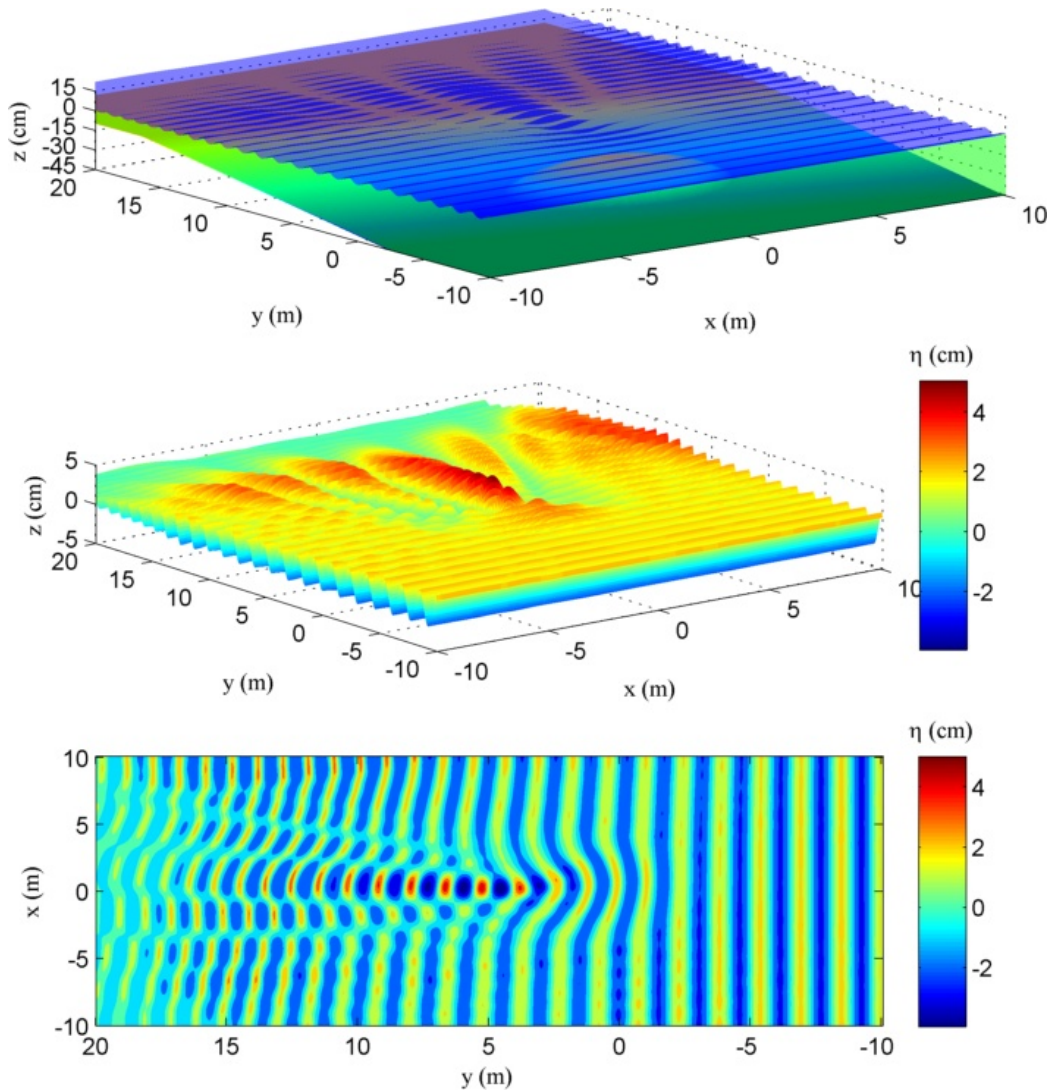
Figure 4.7. A stationary wave field at t = 35 s. Overview (top panel), 3D view of the surface profile (middle panel), 2D view of the surface profile (bottom panel).

a stationary wave field at the end of simulation time is shown in Figure 4.7. In general, the model has simulated nonlinear dispersive wave propagation fairly well.

4.3.5 Solitary wave run-up on a plane beach

In this section, we examine the model's capability to handle wave breaking and wave run-up. Titov and Synolakis (1995) presented a solitary wave with wave height $A/h = 0.3$ (where A is the solitary wave height and h is the still water depth) ran up a beach with slope 1:19.85 as shown in Figure 4.8. The objective of this test is twofold. Firstly, we show

that the model is able to predict wave run-up properly with the simple but efficient wetting and drying algorithm and secondly, we demonstrate that wave breaking process can be well simulated without the use of any empirical parameters, and the result is compared with that computed by the hydrostatic front approximation (HFA) scheme of Smit et al. (2013). In the numerical simulation, mesh sizes are $\Delta x/h = \Delta y/h = 0.125$, a Manning coefficient $n = 0.01$ is used to define the bed surface roughness, and the initial solitary wave is at half of the wave length (L) from the beach toe with L defined by

$$L = \frac{2}{k} \operatorname{arccosh}\left(\sqrt{\frac{1}{0.05}}\right) \tag{4.32}$$

where the wave number $k = \sqrt{3A/4h^3}$.
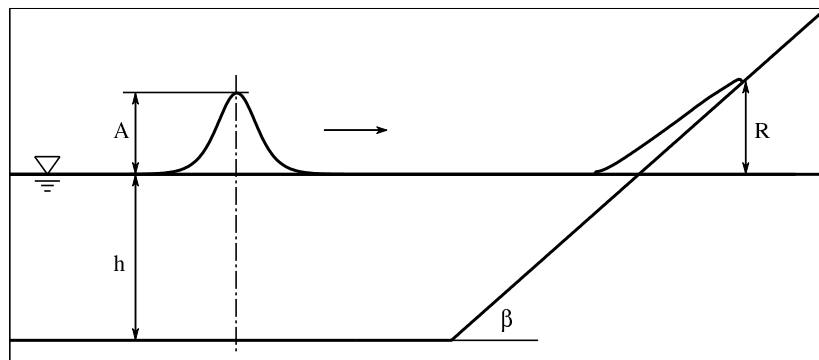
Figure 4.8. Definition sketch of a solitary wave run-up on a plane beach.

Figure 4.9 shows the comparison of simulated and measured free surface elevations. As the wave propagates over the sloped beach, the wave front starts to skew, numerical results with and without the HFA scheme are identical, and both match with experimental data well. As the wave breaks around $t\left(g/h\right)^{1/2} = 20$, these two wave breaking options perform differently, the numerical model without the use of any empirical parameters still preserves a steep wave front, while the model with the HFA scheme already initiated the onset of wave breaking, the wave front has evolved into a bore-like shape. Because of volume conservation, numerical results with two options become similar again when wave breaking stops at $t\left(g/h\right)^{1/2} = 25$. And then the broken wave gradually runs up to the beach till the

65
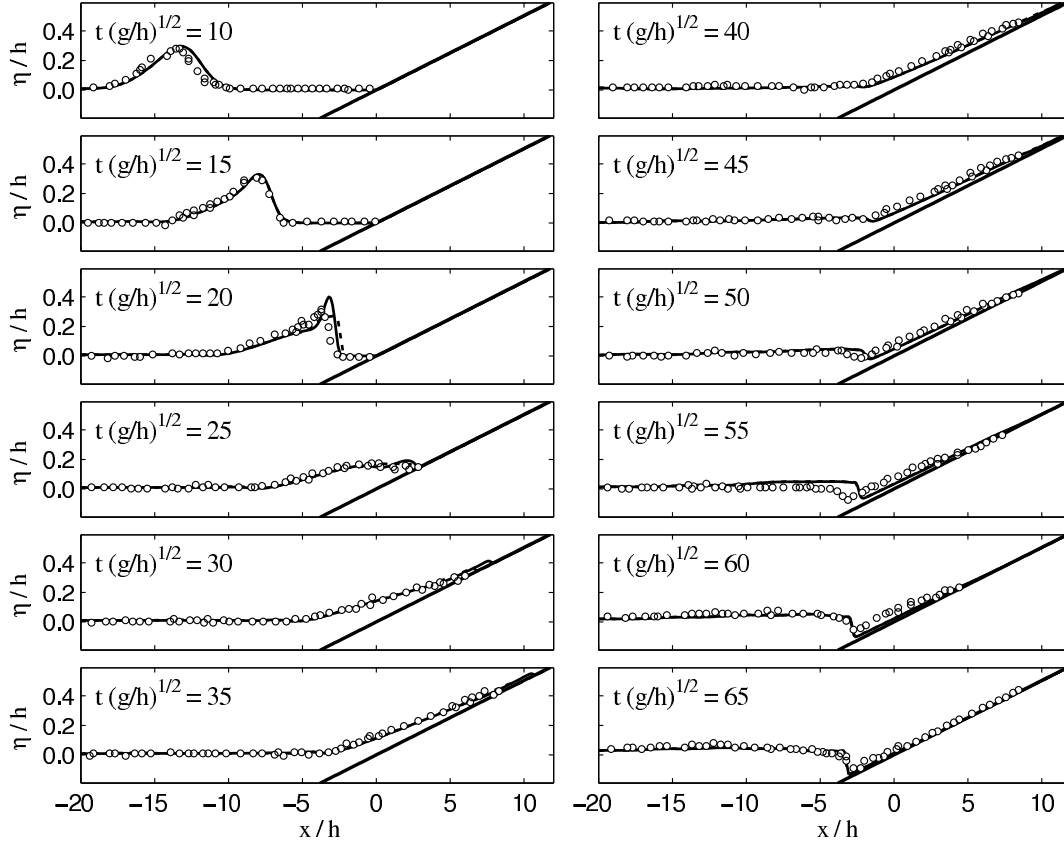
Figure 4.9. Comparison of simulated and measured free surface profiles of a solitary wave run-up on a 1:19.85 plane beach. Experimental data (circles), numerical results with the HFA scheme (dotted lines), numerical results without the HFA scheme (solid lines).

maximum height around $t\,(g/h)^{1/2} = 45$, the run-up process is simulated very well. When the wave retreats from the beach, a hydraulic jump is formed, discrepancies between numerical results and experimental data are observed at $t\,(g/h)^{1/2} = 55$, this may be attributed to the complex 3D vertical flow structure that cannot be captured by the depth-integrated formulation (Yamazaki et al., 2008; Roeber et al., 2010). After this, good agreements are obtained again till the end of retreat process.

4.3.6   Solitary wave propagation over a fringing reef

The existence of fringing reefs in the coastal zone makes nearshore wave processes more complicated. To obtain correct predictions, numerical models must be able to appropriately deal with nonlinear wave dispersion and wave bore propagation. In this section,

66

we simulate a solitary wave transformation over a fringing reef, two series of laboratory experiments on solitary wave transformation over idealized fringing reefs at the O.H. Hinsdale Wave Research Laboratory of Oregon State University, USA, were reported by Roeber et al. (2010) and Roeber and Cheung (2012). The experiment tested in this study was conducted in a 48.8 m long, 2.16 m wide, and 2.1 m high flume. The flume bed configuration includes an offshore flat, a fore reef with a 1:5 slope beginning at $x = 17$ m and a flat reef. The considered case involves a solitary wave of wave height $A = 0.5$ m and a still water depth h = 1.0 m resulting in $A/h = 0.5$ and a dry reef flat. In the numerical simulation, mesh sizes are $\Delta x = \Delta y = 0.05$ m, and the time step is $\Delta t = 0.0025$ s, a Manning coefficient $n = 0.01$ is used to approximate the bed surface roughness.

Figure 4.10 shows the comparison of simulated and measured free surface profiles as the solitary wave propagates across the flume. The initially symmetric wave form begins to skew as the wave approaches the toe of the slope at $x = 17$ m, and gradually the wave front becomes steeper. As the wave surges over the reef, it undergoes transitions from subcritical to supercritical flows starting around $t\,(g/h)^{1/2} = 56$, the numerical model has correctly simulated this process without any difficulties, and also wave fronts are captured reasonably well. After the wave rushes over the dry bed, it forms a sheet flow without producing a distinguishable leading edge with a bore-like shape. Due to wave refraction in the offshore side, the reef edge is exposed as the water level falls down (Roeber et al., 2010). Overall, good agreements between numerical results and experimental data indicate that the wave model has simulated wave shoaling, wave bore propagation, and wave refraction very well.

4.3.7   Tsunami wave propagation and run-up experiments

To better understand the important physical parameters involved in 3D tsunami wave run-up, a series of large-scale tsunami wave experiments funded by the National Science Foundation were conducted during 1992 and 1995 (Briggs et al., 1995; Yeh et al., 1996), these experiments have become benchmark tests for validating numerical models (e.g., Fuhrman
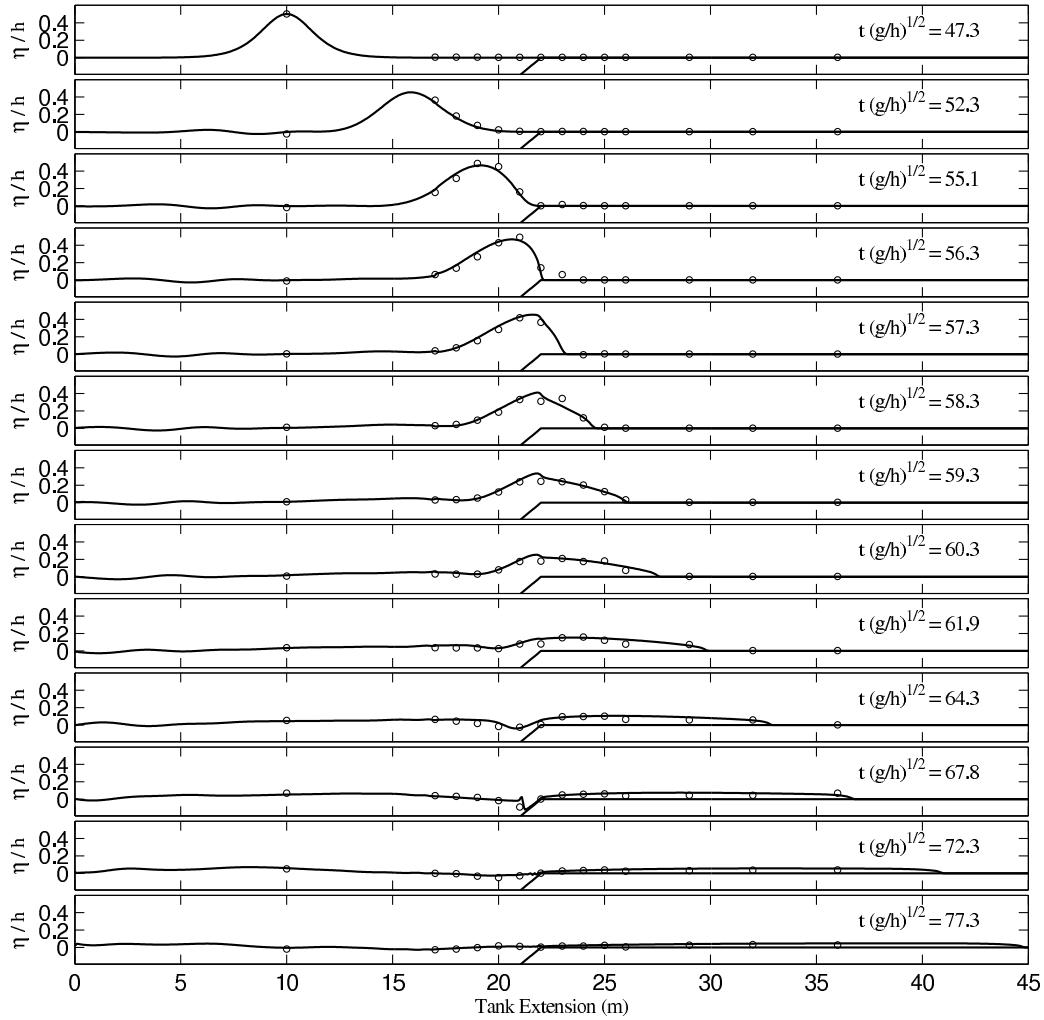
Figure 4.10. Comparison of simulated and measured free surface elevations for a solitary wave propagation over a dry reef flat. Experimental data (circles), numerical results (solid lines).

and Madsen, 2008; Zijlema et al., 2011). In this study, two of them are used to evaluate the developed non-hydrostatic wave model performance.

4.3.7.1   Solitary wave run-up on a vertical wall

The schematic sketch of the 2D flume experiment of a solitary wave run-up on a vertical wall is shown in Figure 4.11. The flume is 23.23 m long and 0.45 m wide, and the compound-slope, fixed-bed bathymetry consists of three different slopes (1:53, 1:150, and 1:13) and a flat section in the deep end. The vertical wall is located at the landward end

68

of the 1:13 slope. The still water depth in the flat section of the flume is $h = 21.8$ cm. 10 capacitance wave gauges were used to measure the free surface elevations along the central line of the flume. Two cases denoted as I and II, with relative wave heights $A/h = 0.039$ and 0.246, respectively, are considered. Case I is a small wave which doesn't become steep enough to break; Case II is a larger wave which breaks just before hitting the wall (Briggs et al., 1996).
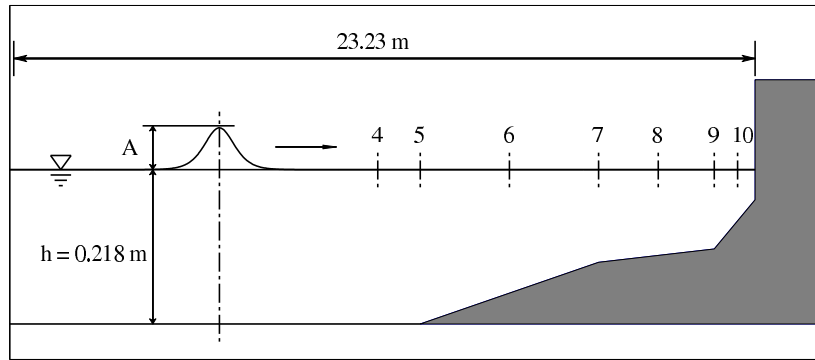
Figure 4.11. Schematic sketch of a solitary wave run-up on a vertical wall.

This benchmark case has been tested by many numerical models as presented in the 2nd International Workshop on Long-wave Run-up Models (Yeh et al., 1996). Because of lack of dispersion, those NLSW models predicted steeper wave fronts than measurements, and eventually lead to premature breaking. This phenomenon was more pronounced for the highly nonlinear wave in Case II. Besides, phase difference between numerical results and measurements was also clearly observed (e.g., Watson et al., 1996). In this study, the grid resolution is determined by the wave length to ensure that each of the waves is approximated by at least one hundred cells, and therefore, mesh sizes $\Delta x = \Delta y = 0.05$ m and 0.02 m are used for Cases I and II, respectively. Correspondingly, time steps $\Delta t = 0.01$ s and 0.005 s are used for Cases I and II, respectively.

Figure 4.12 shows the comparison of simulated and measured wave profiles for both cases. The measured data at Gauge 5 provide a reference for adjustment of timing of the simulated wave forms. For Case I with a small relative wave height, good agreements between
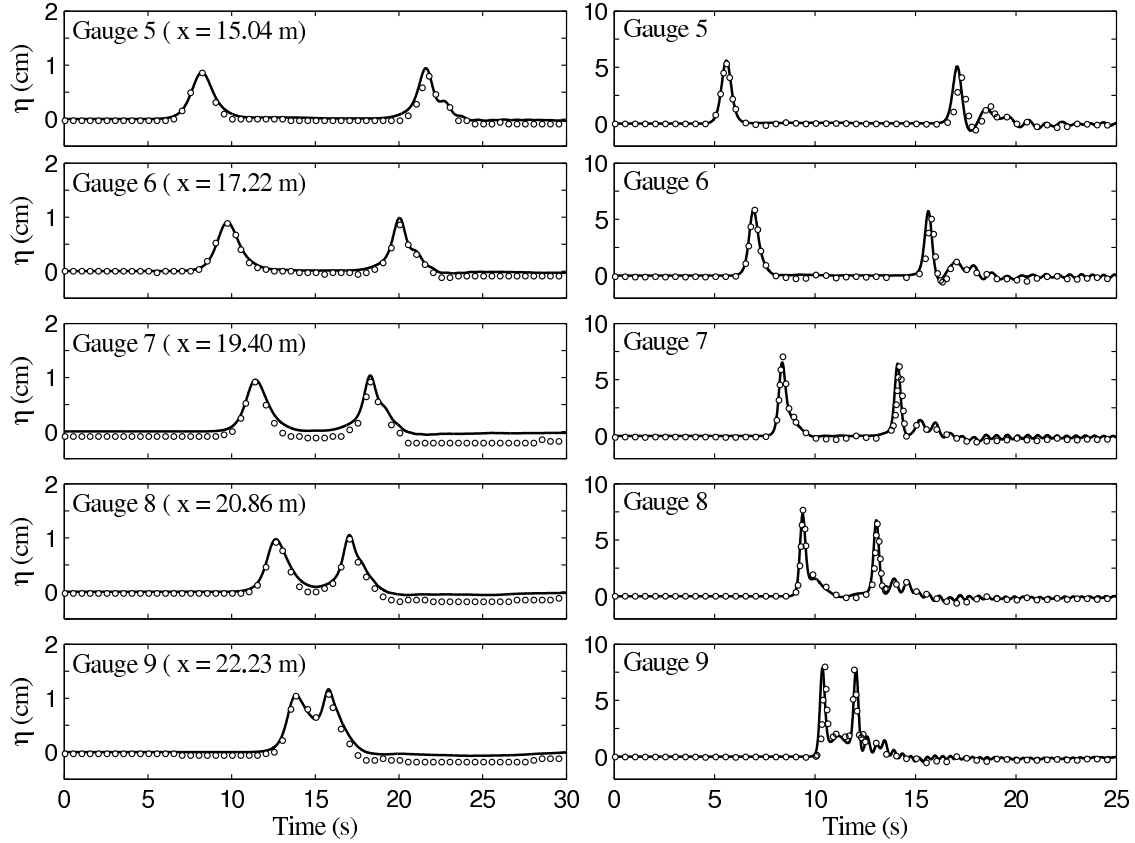
Figure 4.12. Comparison of simulated and measured free surface elevations for a solitary wave run-up on a vertical wall: $A/h = 0.039$ (left panel), $A/h = 0.246$ (right panel). Experimental data (circles), numerical results (solid lines).

numerical results and measured data for both incoming and reflected waves are obtained as shown in the left panel, small zero offsets (≈ 3 mm) of the experimental data as shown in Gauges 7, 8, and 9 might be due to the experiment setup[1]. In the right panel, numerical results for Case II are presented, although the wave breaks near the wall, the numerical model is able to run through it without the use of any empirical parameters, and satisfactory predictions are also obtained. It is noted that simulated reflected wave peaks are higher than measurements at Gauges 5 and 6, while minor discrepancies of wave phase are also observed at these two gauges. Since a higher wave travels faster, the phase difference may be attributed to the higher wave predicted by the model.

---

[1]Personal communication with Dr. Michael J. Briggs (2013), who conducted this experiment.
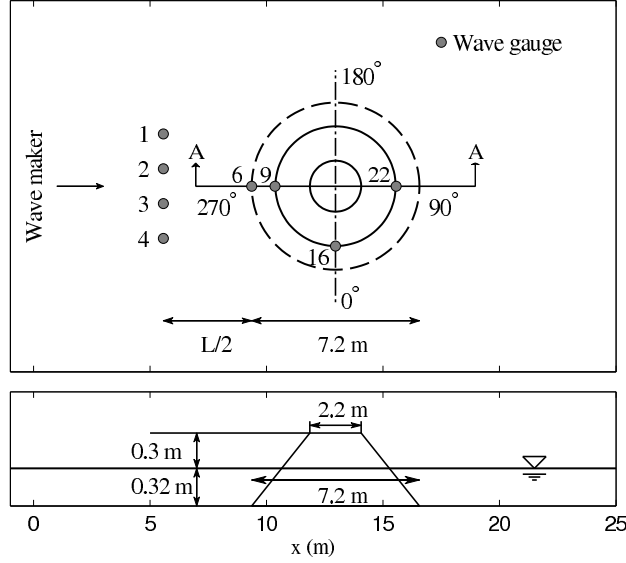
Figure 4.13. Schematic sketch of a solitary wave run-up on a conical island. Plane view (top panel), side view (bottom panel).

4.3.7.2   Solitary wave run-up on a conical island

The other tsunami wave experiment considered in this study is a solitary wave run-up on a conical island (Briggs et al., 1995). The experiment was conducted in a 30 m wide and 25 m long flat bottom basin as shown in Figure 4.13. The center of the island is located at $x = 12.96$ m and $y = 13.80$ m, and the shape of the island is a truncated circular cone with diameters of 7.2 m at the toe and 2.2 m at the crest. The vertical height of the island is about 62.5 cm, with a 1:4 beach face. Wave absorbers are placed at all sides of the basin. 27 capacitance wave gauges were used to measure the free surface elevations, and the maximum vertical run-up heights were also recorded around the perimeter of the island using rod and transit. Different still water depths and relative wave heights were tested in the experiment. In this study, we only consider the still water depth $h = 32$ cm and three cases denoted as I, II, and III with relative wave heights $A/h = 0.045$, 0.096, and 0.181, respectively. This set of experiment has been widely tested by NLSW models (e.g., Liu et al., 1995; Wei et al., 2006), Boussinesq-type models (e.g., Lynett et al., 2002; Fuhrman and Madsen, 2008), and non-hydrostatic models (e.g., Yamazaki et al., 2008; Zijlema et al., 2011).

71
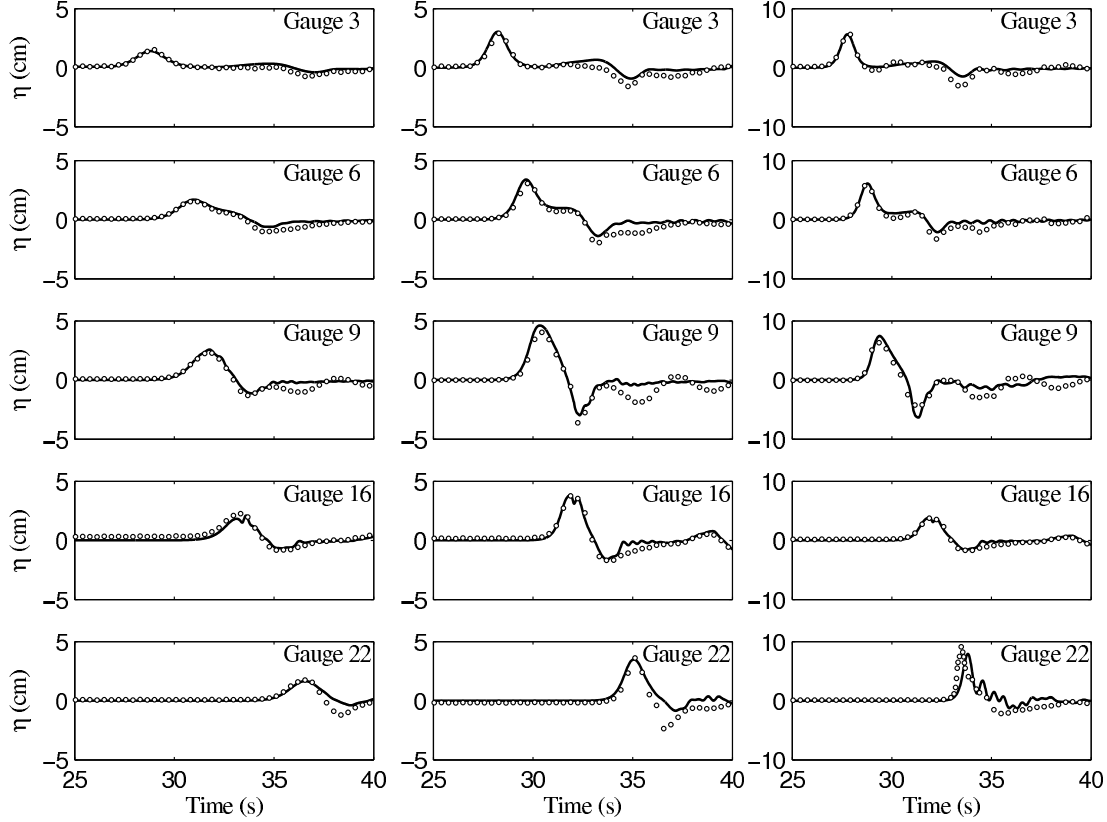
Figure 4.14. Comparison of simulated and measured surface elevations for a solitary wave run-up on a conical island: $A/h = 0.045$ (left panel), $A/h = 0.096$ (middle panel), $A/h = 0.181$ (right panel). Experimental data (circles), numerical results (solid lines).

In the numerical simulation, the solitary wave propagates from the western boundary toward the island; the radiation boundary condition is applied at the eastern boundary; the lateral walls are treated as fully reflective boundaries. The basin is discretized with mesh sizes $\Delta x = \Delta y = 0.05$ m, and the time step is $\Delta t = 0.01$ s, the bed surface friction is assumed zero as the surface of the island and basin were constructed with smooth concrete. Figure 4.14 shows the comparison of simulated and measured free surface elevations at selected wave gauges for all three cases. The measured data at Gauge 3 provide a reference for adjustment of timing of the simulated wave forms. For Case I with a small relative wave height $A/h = 0.045$, good agreements between numerical results and measurements are obtained including the depression following leading wave that was not adequately captured in previous studies (e.g., Lynett et al., 2002). For Case II with a medium relative wave
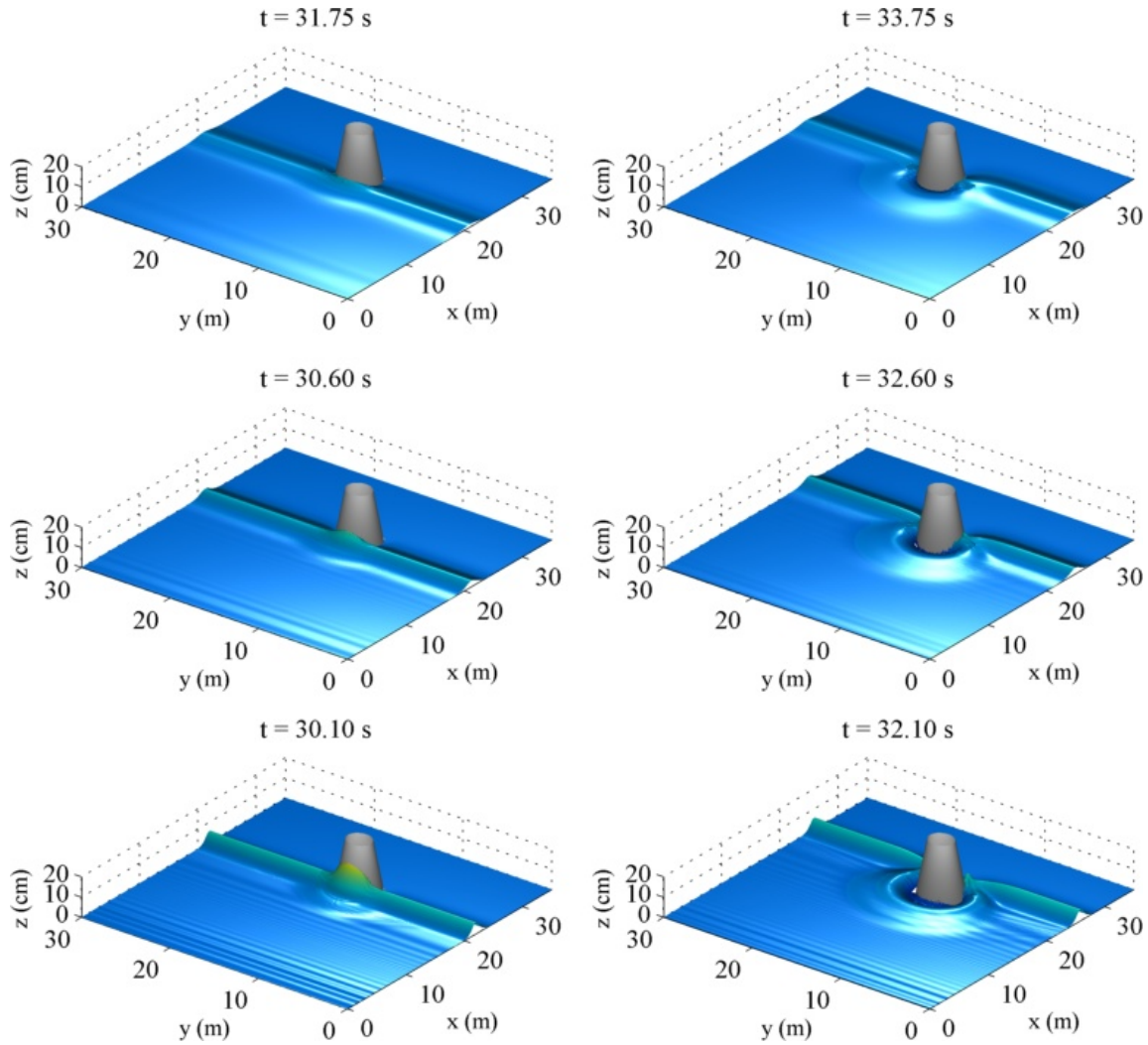
Figure 4.15. Wave transformation in front of the conical island: $A/h = 0.045$ (top panel), $A/h = 0.096$ (middle panel), $A/h = 0.181$ (bottom panel).

height $A/h = 0.096$, overall agreements are also very good, although the numerical model slightly underpredicts the wave depression at Gauge 22. For Case III with a large relative wave height $A/h = 0.181$, wave breaking was observed at Gauge 22 in the experiment, the numerical model without the use of any empirical parameters, again, successfully handles the breaking process without any difficulties, the wave peak is slightly underpredicted, and the model gives a minor phase difference, which was also predicted by other models (e.g., Yamazaki et al., 2008; Zijlema et al., 2011). We also ran the model with the HFA scheme, similar results have been obtained (not shown here). Next, the wave-structure interaction
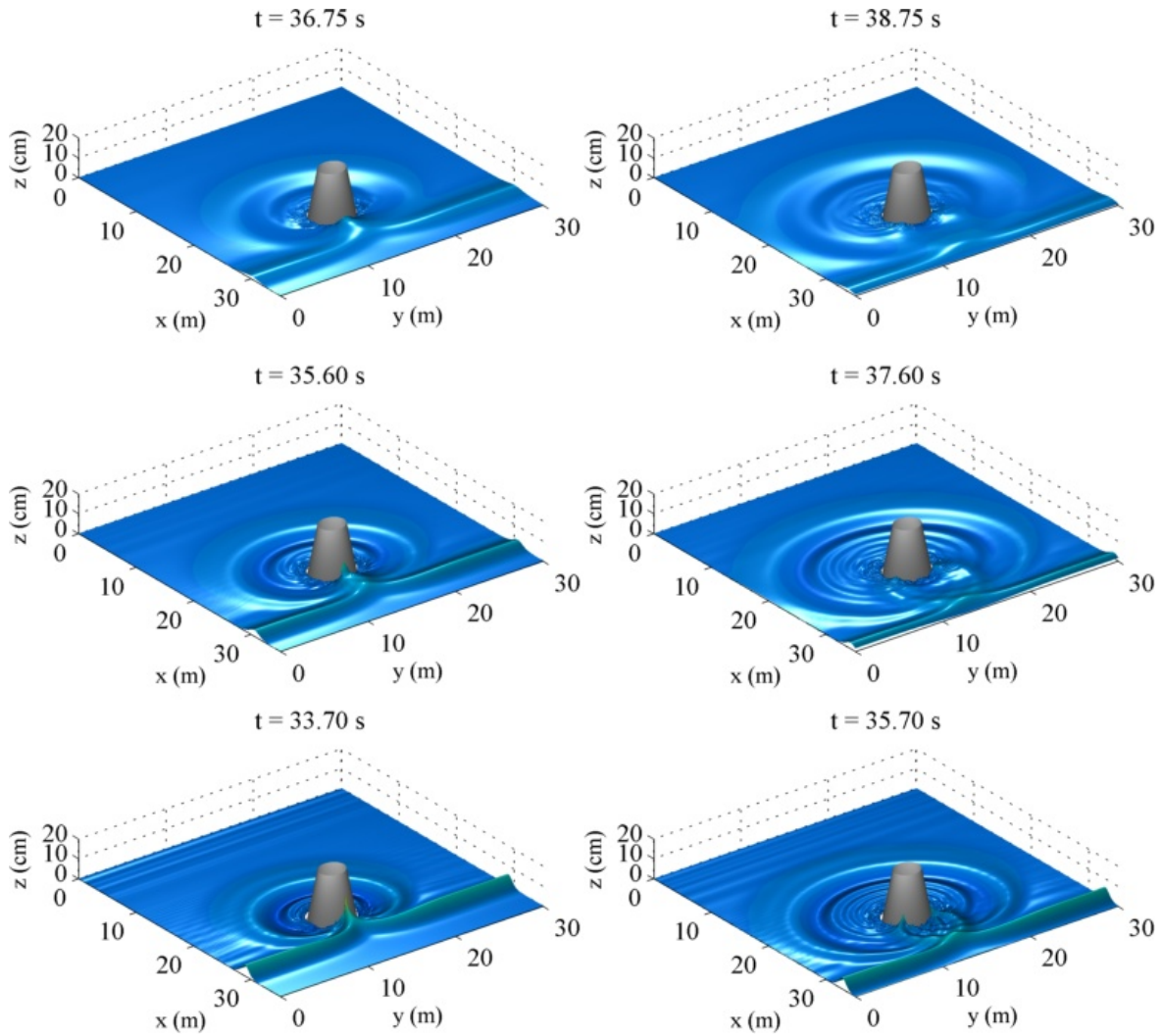
Figure 4.16. Wave transformation at the lee side of the conical island: $A/h = 0.045$ (top panel), $A/h = 0.096$ (middle panel), $A/h = 0.181$ (bottom panel).

phenomenon during solitary wave transformation is presented in Figures 4.15 and 4.16. In the left panel of Figure 4.15, the waves approximately reach the maximum run-up at the front side of the conical island, and the right panel shows the waveforms after 2 seconds, wave refraction and diffraction are clearly observed. Because of the existence of the island, the solitary wave is separated into two branches. Once the wave transforms around the island, they hit each other at the lee side of the island and then the waves approximately reach the maximum run-up as shown in the left panel of Figure 4.16. For Case II, the wave breaks locally at the lee side, and wave breaking occurs everywhere around the island for
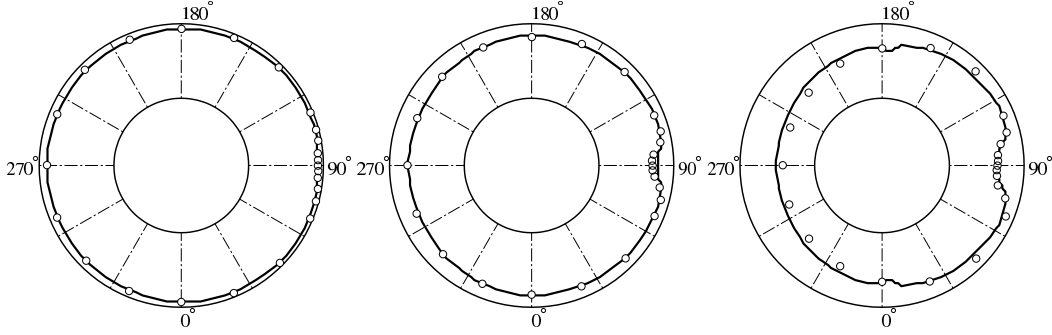
Figure 4.17. Comparison of simulated and measured maximum vertical run-up heights for a solitary wave run-up on a conical island: $A/h = 0.045$ (left panel), $A/h = 0.096$ (middle panel), $A/h = 0.181$ (right panel). Experimental data (circles), numerical results (solid lines).

Case III (Titov and Synolakis, 1998). The right panel of Figure 4.16 shows the wave field after 2 seconds, the trapped waves pass by each other and evolve around the island. Finally, the maximum vertical run-up heights are shown in Figure 4.17. Excellent agreements of the maximum inundation positions for Case I have been obtained. For Case II, overall agreements are also very good; run-up heights at the lee side are slightly underpredicted. For Case III, inundation positions at the lee side are correctly predicted, but underpredictions are observed in the front side, and this phenomenon was also reported in aforementioned papers.

4.4   Chapter Summary

This chapter has presented the formulation, verification, and validation of a depth-integrated non-hydrostatic finite element model, CCHE2D-NHWAVE, for simulating nearshore wave processes, involving nonlinear wave shoaling, diffraction, refraction, focusing, breaking, and run-up. The depth-integrated formulation is equipped with weakly dispersive properties by incorporating the non-hydrostatic pressure. As a result, it is able to simulate relatively short free surface waves to a certain extent. To capture discontinuous flows, a momentum conservation advection scheme has been built on top of the partially staggered grid, and it enables the model to simulate breaking waves without the use of empirical relations. Fi-

75

nally, a simple and efficient wetting and drying algorithm has been developed to describe the moving shoreline.

A series of numerical tests have been carried out to verify and validate the developed model. The first three cases with analytical solutions have demonstrated that the non-hydrostatic wave model is well-balanced and efficient for modeling moving boundaries. The following four sets of laboratory experiments, which present several nearshore wave phenomena (e.g., nonlinear dispersive wave propagation, breaking, and run-up), have been used to evaluate the model's capability for simulating real-life and large-scale wave motions. Good agreements between numerical results and experimental data proved that the depth-integrated non-hydrostatic model is applicable to resolve a wide range of wave processes in the nearshore zone. In the future, the model will be extended with more layers, so that highly dispersive waves can be well represented and the vertical structure of flows will be better approximated.

CHAPTER 5

MULTI-LAYER MODEL FOR WAVE PROPAGATION

This chapter presents a multi-layer non-hydrostatic model for simulating wave propagation. The computation domain is vertically split by several strictly horizontal layers, and the horizontal momentum equations are obtained by vertical integration inside each layer. The vertical momentum equation is approximated by the Keller-Box scheme. The governing equations are solved in several steps. First of all, the provisional velocity field is calculated without considering the non-hydrostatic pressure contribution. Then the non-hydrostatic pressure is obtained through the divergence-free velocity condition. Next the velocity is updated by including the non-hydrostatic pressure. Finally, the free surface elevation is computed using the depth-integrated continuity equation. The model is verified and validated by several analytical solutions and experimental data, the good agreement between numerical results and experimental data shows that the multi-layer model demonstrates a better capability than that of the depth-integrated non-hydrostatic model for modeling highly dispersive waves and highly nonlinear waves.

In the following sections, the governing equations are presented in Section 5.1. And then the numerical formulation with detailed numerical procedures is described in Section 5.2. Next, we verify and validate the multi-layer non-hydrostatic model with several benchmark cases in Section 5.3. Finally, we summarize the findings in this work in Section 5.4.

5.1 Governing Equations

The governing equations of the multi-layer non-hydrostatic wave model in the conservation form have been derived in detail in Chapter 2. We start from the simplified governing equations without considering the shear stress and turbulent stress terms as follows

$$h_k \frac{\partial u_k}{\partial t} + \left[\frac{\partial (huu)_k}{\partial x} - u_k \frac{\partial (hu)_k}{\partial x} \right] + \left[\frac{\partial (huv)_k}{\partial y} - u_k \frac{\partial (hv)_k}{\partial y} \right] + \left(u_{k+1/2} w_{k+1/2} - u_{k-1/2} w_{k-1/2} \right) =$$
$$-gh_k \frac{\partial \eta}{\partial x} - \frac{1}{\rho} \left(\frac{\partial h_k q_k}{\partial x} - q \frac{\partial z}{\partial x} \Big|_{z_{k-1/2}}^{z_{k+1/2}} \right) \tag{5.1}$$

$$h_k \frac{\partial v_k}{\partial t} + \left[\frac{\partial (huv)_k}{\partial x} - v_k \frac{\partial (hu)_k}{\partial x} \right] + \left[\frac{\partial (hvv)_k}{\partial y} - v_k \frac{\partial (hv)_k}{\partial y} \right] + \left(v_{k+1/2} w_{k+1/2} - v_{k-1/2} w_{k-1/2} \right) =$$
$$-gh_k \frac{\partial \eta}{\partial y} - \frac{1}{\rho} \left(\frac{\partial h_k q_k}{\partial y} - q \frac{\partial z}{\partial y} \Big|_{z_{k-1/2}}^{z_{k+1/2}} \right) \tag{5.2}$$

$$\frac{\partial (hw)_{k-1/2}}{\partial t} + \frac{\partial (hw)_{k+1/2}}{\partial t} = -\frac{2}{\rho} \left(q_{k+1/2} - q_{k-1/2} \right) \tag{5.3}$$

where k is the layer index, u, v, and w are velocity components in x, y, and z directions, respectively; h is the layer thickness; q is the non-hydrostatic pressure.

Similar to previous two chapters, the aforementioned governing equations are solved together with the local continuity equation (2.1) for determining the non-hydrostatic pressure. In the following sections, Efficient Element Method (see, e.g., Chapter 3 for details) is still applied to solve the horizontal momentum equations, while the finite difference method is applied in the vertical momentum equation.

5.2 Numerical Formulation

In this study, the computation is accomplished in several steps similar to those presented in Chapter 3. In the first step, the momentum equations without non-hydrostatic pressure terms are solved for a provisional velocity field; in the second step, the non-hydrostatic

78

pressure is implicitly solved by ensuring the divergence-free velocity condition, and the non-hydrostatic pressure is used to update the provisional velocity; finally, the depth-integrated continuity equation is explicitly solved to update the free surface elevation for global mass conservation.

5.2.1 First step

In the first step, the provisional velocities, $\tilde{u}$, $\tilde{v}$, and $\tilde{w}$ are solved explicitly by the following momentum equations without considering non-hydrostatic pressure terms:

$$h_k \frac{\partial u_k}{\partial t} + ADV u_k + \left(u_{k+1/2} w_{k+1/2} - u_{k-1/2} w_{k-1/2} \right) = -g h_k \frac{\partial \eta}{\partial x} \tag{5.4}$$

$$h_k \frac{\partial v_k}{\partial t} + ADV v_k + \left(v_{k+1/2} w_{k+1/2} - v_{k-1/2} w_{k-1/2} \right) = -g h_k \frac{\partial \eta}{\partial y} \tag{5.5}$$

$$\frac{\partial (hw)_{k-1/2}}{\partial t} + \frac{\partial (hw)_{k+1/2}}{\partial t} = 0 \tag{5.6}$$

Where $ADV u_k$ and $ADV v_k$ represent the grouped advection terms in the u and v momentum equations, which could be approximated by the momentum conservation scheme introduced in Chapter 4. In the case that the bed friction is considered, the Manning equation is included in the bottom layer and the horizontal momentum equations are solved semi-implicitly in the bottom layer.

By using the finite element operators introduced in Chapter 3, Equations (5.4), (5.5), and (5.6) are discretized as

$$\frac{\tilde{u}_k^{n+1} - u_k^n}{\Delta t} + \frac{ADV u_k^n}{h_k^n} + \frac{\left(u_{k+1/2}^n w_{k+1/2}^n - u_{k-1/2}^n w_{k-1/2}^n \right)}{h_k^n} = -g \sum_{m=1}^{4} \frac{\partial B_m^c \eta_m^n}{\partial x} \tag{5.7}$$

$$\frac{\tilde{v}_k^{n+1} - v_k^n}{\Delta t} + \frac{ADV v_k^n}{h_k^n} + \frac{\left(v_{k+1/2}^n w_{k+1/2}^n - v_{k-1/2}^n w_{k-1/2}^n \right)}{h_k^n} = -g \sum_{m=1}^{4} \frac{\partial B_m^c \eta_m^n}{\partial y} \tag{5.8}$$

$$\tilde{w}_{k+1/2}^{n+1} - w_{k+1/2}^n + \frac{h_{k-1/2}^n}{h_{k+1/2}^n} \left(\tilde{w}_{k-1/2}^{n+1} - w_{k-1/2}^n \right) = 0 \tag{5.9}$$

where u^n, v^n, and w^n are velocity solutions at the previous time level n. To calculate the provisional vertical velocity using Equation (5.9), the vertical velocity at the bottom should be first determined, and it is approximated by using the kinematic boundary condition at the bottom of Equation (2.6).

5.2.2 Second step

In the second step, the momentum equations (5.4), (5.5), and (5.6) including the non-hydrostatic pressure are considered as follows

$$h_k \frac{\partial u_k}{\partial t} = -\frac{1}{\rho} \left(\frac{\partial h_k q_k}{\partial x} - q \frac{\partial z}{\partial x} \Big|_{z_{k-1/2}}^{z_{k+1/2}} \right) \tag{5.10}$$

$$h_k \frac{\partial v_k}{\partial t} = -\frac{1}{\rho} \left(\frac{\partial h_k q_k}{\partial y} - q \frac{\partial z}{\partial y} \Big|_{z_{k-1/2}}^{z_{k+1/2}} \right) \tag{5.11}$$

$$\frac{\partial (hw)_{k+1/2}}{\partial t} = -\frac{2}{\rho} \left(q_{k+1/2} - q_{k-1/2} \right) \tag{5.12}$$

where the non-hydrostatic pressure at the middle of a vertical layer q_k is approximated by $q_k = (q_{k+1/2} + q_{k-1/2})/2$. Because a strictly horizontal layer interface is used in this study, there is no horizontal gradient of layer interface at internal nodes, i.e., $\frac{\partial z}{\partial x} = 0$ and $\frac{\partial z}{\partial y} = 0$. As a result, the above momentum equations are discretized by

$$h_k^n \frac{u_k^{n+1} - \tilde{u}_k^{n+1}}{\Delta t} = -\frac{1}{2\rho} \left(\sum_{m=1}^{4} \frac{\partial B_m^c h_{k+1/2,m}^n q_{k+1/2,m}^{n+1}}{\partial x} + \sum_{m=1}^{4} \frac{\partial B_m^c h_{k-1/2,m}^n q_{k-1/2,m}^{n+1}}{\partial x} \right) \tag{5.13}$$

$$h_k^n \frac{v_k^{n+1} - \tilde{v}_k^{n+1}}{\Delta t} = -\frac{1}{2\rho} \left(\sum_{m=1}^{4} \frac{\partial B_m^c h_{k+1/2,m}^n q_{k+1/2,m}^{n+1}}{\partial y} + \sum_{m=1}^{4} \frac{\partial B_m^c h_{k-1/2,m}^n q_{k-1/2,m}^{n+1}}{\partial y} \right) \tag{5.14}$$

$$\frac{w_{k+1/2}^{n+1} - \tilde{w}_{k+1/2}^{n+1}}{\Delta t} = -\frac{2}{\rho h_{k+1/2}^n} \left(q_{k+1/2}^{n+1} - q_{k-1/2}^{n+1} \right) \tag{5.15}$$

To calculate the non-hydrostatic pressure at the new time level $n+1$ by enforcing a divergence-free velocity field, the local continuity equation (2.1) is applied to each horizontal

layer in the following form

$$\left(\frac{\partial u_k^{n+1}}{\partial x} + \frac{\partial v_k^{n+1}}{\partial y}\right) + \frac{\left(w_{k+1/2}^{n+1} - w_{k-1/2}^{n+1}\right)}{h_k^n} = 0 \qquad (5.16)$$

Substitution of Equations (5.13), (5.14), and (5.15) into Equation (5.16) gives a Poisson equation involving the non-hydrostatic pressure variables at layer interfaces $k+1/2$ and $k-1/2$. The discretized Poisson equation is in the form of a ten-diagonal algebraic equation system, which is solved by using the BiCGSTAB solver (Van der Vorst, 1992) with a preconditioner of the incomplete LU factorization, as implemented in SPARSKIT by Saad (2005).

Once the non-hydrostatic pressure is solved, the horizontal velocities u_k^{n+1} and v_k^{n+1}, and the vertical velocity $w_{k+1/2}^{n+1}$ are corrected by using Equations (5.13), (5.14), and (5.15), respectively.

5.2.3 Third step

In the last step, the free surface elevation is calculated by using the depth-integrated equation with the updated horizontal velocities by

$$\eta^{n+1} = \eta^n - \Delta t \left(\sum_{m=1}^{4} \frac{\partial B_m^s (H^n U^{n+1})_m}{\partial x} + \sum_{m=1}^{4} \frac{\partial B_m^s (H^n V^{n+1})_m}{\partial y}\right) \qquad (5.17)$$

where H is the total water depth at collocation nodes, and the depth-integrated horizontal velocity is calculated by, e.g., $U = \sum_{k=1}^{K} h_k u_k / H$ with K the total number of vertical layers.

5.3 Model Verification and Validation

In this section, we verify and validate the multi-layer non-hydrostatic wave model for wave propagation by using analytical solutions and experimental data. Although more layers could be adopted, a two-layer non-hydrostatic model is used in all cases. Its capability for modeling highly dispersive waves and highly nonlinear waves is confirmed by comparing

its numerical result with that predicted by the depth-integrated non-hydrostatic model. Regarding the layer interface between the top layer and the bottom layer, it is usually located at the upper part of the domain to provide a better prediction for the non-hydrostatic pressure at the bottom of the top layer. However, special attention is also paid to avoid that the free surface penetrates the layer interface.

5.3.1 Head-on collision of two solitary waves
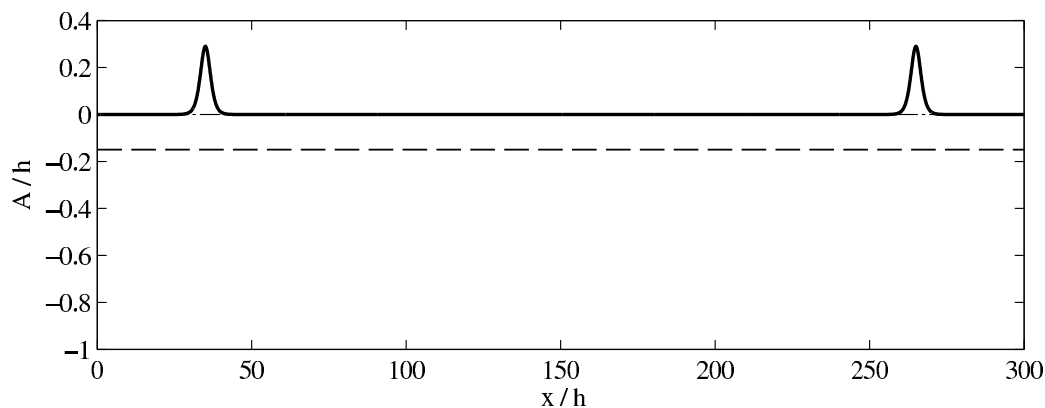
Figure 5.1. Initial setup of the two solitary waves head-on collision. Layer interface of the two-layer model (dashed line).

The solitary wave represents a good balance between frequency dispersion and non-linearity. It has been widely used to verify and validate the correct implementation of Boussinesq-type and non-hydrostatic models (e.g., Wei and Kirby, 1995; Stelling and Zijlema, 2003). In this section, we consider the head-on collision of two highly nonlinear solitary waves in a constant water depth channel. The depth of the frictionless channel is $h = 10$ m, and each of solitary waves has a wave height of $A = 3$ m. The total length of the channel is $300 \times h$ long, and the initial locations for two opposing solitary waves are at $x = 35 \times h$ and $265 \times h$. The computation domain is discretized with mesh sizes $\Delta x = \Delta y = 1.0$ m, and a numerical time step $\Delta t = 0.02$ s is used. For the two-layer simulation, the computation domain is split by a horizontal layer interface into two with a ratio 15:85, as indicated in Figure 5.1.
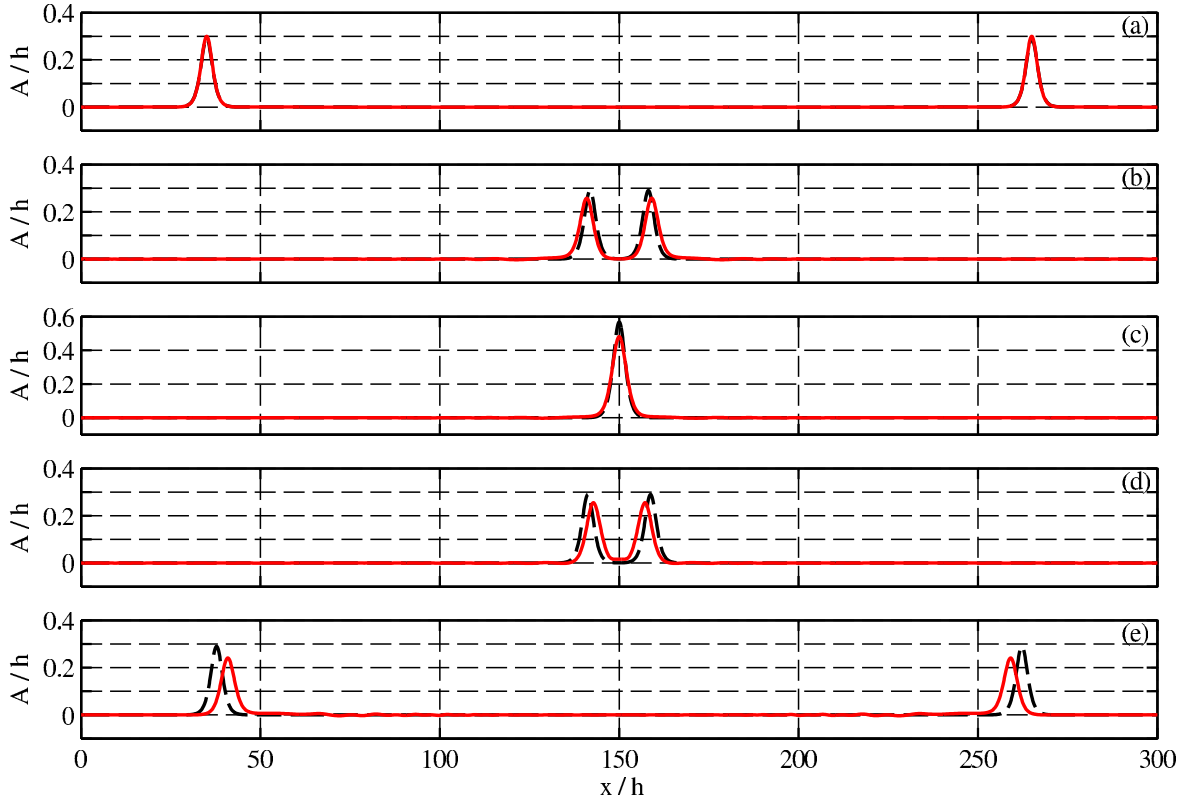
Figure 5.2. Free surface profiles of two solitary waves with $A/h = 0.3$ propagating in opposite directions in a channel of constant depth using a depth-integrated non-hydrostatic model. Analytical solution (dashed lines), numerical result (solid lines). (a) $t\,(g/h)^{1/2} = 0$, (b) $t\,(g/h)^{1/2} = 94$, (c) $t\,(g/h)^{1/2} = 101.5$, (d) $t\,(g/h)^{1/2} = 109$, and (e) $t\,(g/h)^{1/2} = 200$.

Figures 5.2 and 5.3 show the free surface profile as the two solitary waves head toward each other at several time levels predicted by a depth-integrated model and a two-layer non-hydrostatic model, respectively. It has been tested in previous two chapters that the depth-integrated model is able to simulate correct waveform and wave phase for a solitary wave with a relative wave height $A/h = 0.2$. When it comes to a higher nonlinear solitary wave considered in this test, it suffers from underprediction of wave height and an apparent phase lag even before the collision, as shown in Figure 5.2.

From the numerical result of the two-layer model as presented in Figure 5.3, the waveform is correctly conserved as the wave propagates from its initial location to the middle of channel at $t\,(g/h)^{1/2} = 94$. At $t\,(g/h)^{1/2} = 101.5$, two waves collide each other and the

83
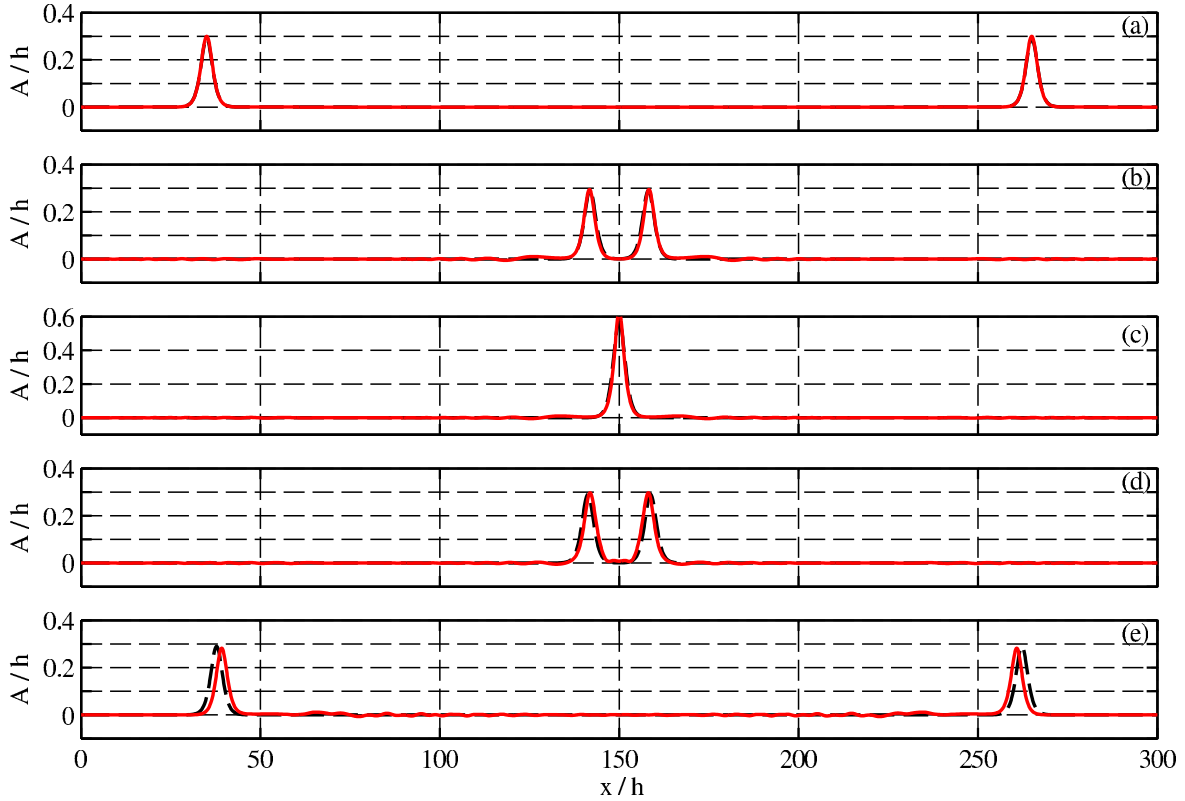
Figure 5.3. Free surface profiles of two solitary waves with $A/h = 0.3$ propagating in opposite directions in a channel of constant depth using a two-layer non-hydrostatic model. Analytical solution (dashed lines), numerical result (solid lines). (a) $t\,(g/h)^{1/2} = 0$, (b) $t\,(g/h)^{1/2} = 94$, (c) $t\,(g/h)^{1/2} = 101.5$, (d) $t\,(g/h)^{1/2} = 109$, and (e) $t\,(g/h)^{1/2} = 200$.

wave reaches a relative wave height of $A/h = 0.6$. After the collision, two waves continue to propagate toward their original directions, there is a slight phase lag of numerical results observed at $t\,(g/h)^{1/2} = 109$. Finally, they arrive at the initial location of the other wave at $t\,(g/h)^{1/2} = 200$. After traveling a long distance, the phase lag becomes more apparent, and this has also been previously reported by Maxworthy (1976) using a physical experiment and by Roeber et al. (2010) using a Boussinesq-type model. In addition, wave height reduction has been observed in the numerical results of both depth-integrated and two-layer models. It is found that there is about 6% wave height reduction predicted by the two-layer model, however, the depth-integrated model gives a much larger reduction around 20%. From this comparison, it can also be concluded that a multi-layer model is able to better preserve a

high nonlinear wave propagation.

5.3.2   Standing wave oscillation in a closed basin
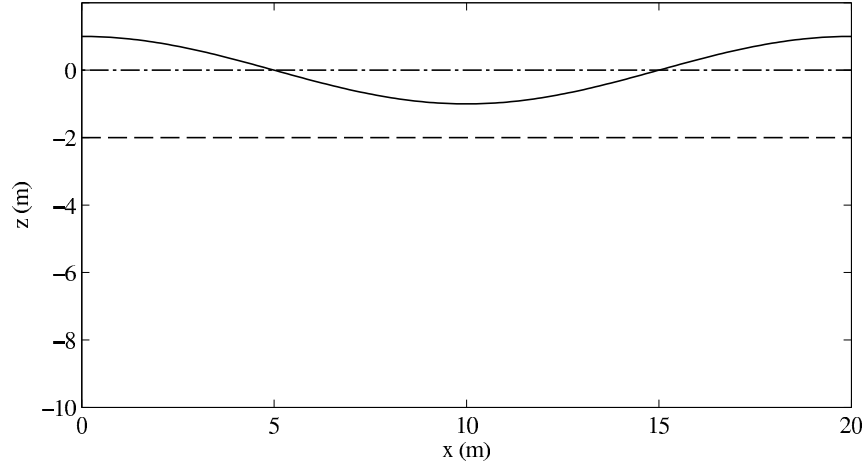
Figure 5.4. Definition sketch of a standing wave oscillation in a closed basin. Layer interface of the two-layer model (dashed line). Note: the initial standing wave profile is not drawn in the true scale.

One of the benchmark cases in literature to test the dispersive properties of both Boussinesq-type and non-hydrostatic models is a standing linear wave oscillation in a closed basin (e.g., Casulli and Stelling, 1998; Stelling and Zijlema, 2003). The analytical solution of a standing wave is given by (Sorensen, 2006)

$$\eta(x,t) = a\cos(kx)\cos(\omega t) \tag{5.18}$$

where a is the amplitude of the standing wave; k is the wave number; ω is the angular frequency. For a sufficiently small a, the relation between k and ω is determined by the linear wave theory through the linear dispersion relation:

$$\omega^2 = gk\tanh(kH) \tag{5.19}$$

where g is the gravitational acceleration, and H is the local water depth.

In this study, we consider a closed basin with length of 20 m and water depth of 10 m. The initial condition for the standing wave with an amplitude $a = 0.1$ m is specified by

$$\eta(x, 0) = a \cos\left(\frac{\pi x}{10}\right), 0 \leq x \leq 20 \tag{5.20}$$

This setup implies that the wave length is the same with the basin length of 20 m, and we could obtain the water depth parameter $kH = \pi$, which indicates the wave is highly dispersive. Furthermore, from Equation (5.19), we calculate the wave period of $T = 3.59$ s.

In the numerical simulation, the closed basin is discretized with mesh sizes $\Delta x = \Delta y = 0.5$ m, and a numerical time step $\Delta t = 0.01$ s is used. For the two-layer simulation, the depth ratio between the top layer and the bottom layer is 1:4, as indicated in Figure 5.4. At two wall sides of the basin, the velocity is zero, and the free surface elevation satisfies the Neumann boundary condition with a zero gradient.
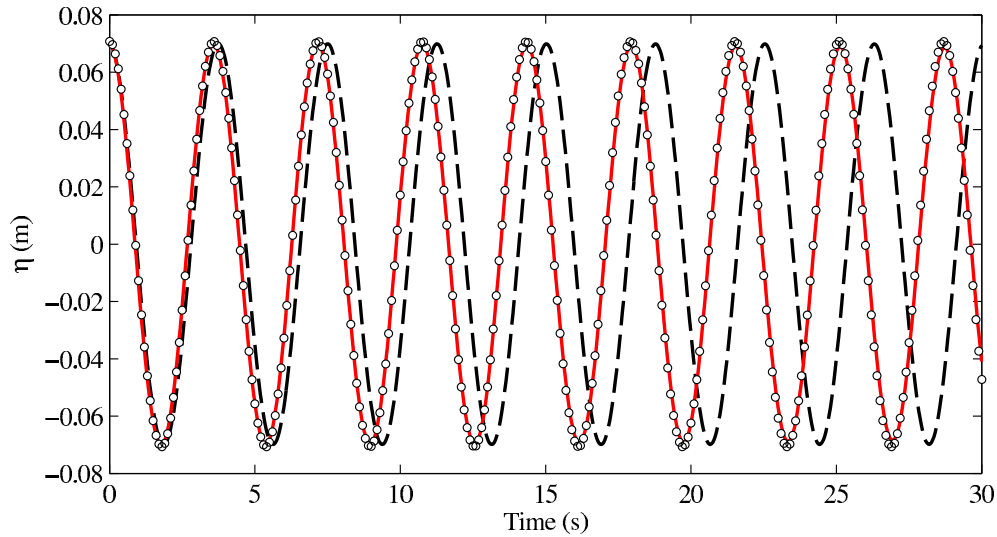
Figure 5.5. Comparison of simulated and analytical solution of time series free surface elevation at $x =$17.5 m. Analytical solution (circles), numerical results with a depth-integrated model (dashed line), numerical results with a two-layer model (solid line).

In this study, we compare the time series free surface elevation at the location of $x =$17.5 m with the analytical solution generated by Equation (5.18). First of all, the computation is carried out by using a depth-integrated model, and the result is presented in

Figure 5.5. The comparison shows that the computed free surface elevation has a longer wave period than that of $T = 3.59$ s, which indicates that the depth-integrated model predicts the wave celerity in deep water erroneously. To resolve the hyperbolic profile of the vertical velocity, more than one layer should be employed. Next, we rerun the simulation with a two-layer model, and also present the numerical result in Figure 5.5. It shows that a perfect agreement with the analytical solution is clearly obtained with a two-layer model. And therefore, this case verifies the superiority of a multi-layer model over a depth-integrated model for simulating highly dispersive waves.

5.3.3   Wave propagation over a submerged bar
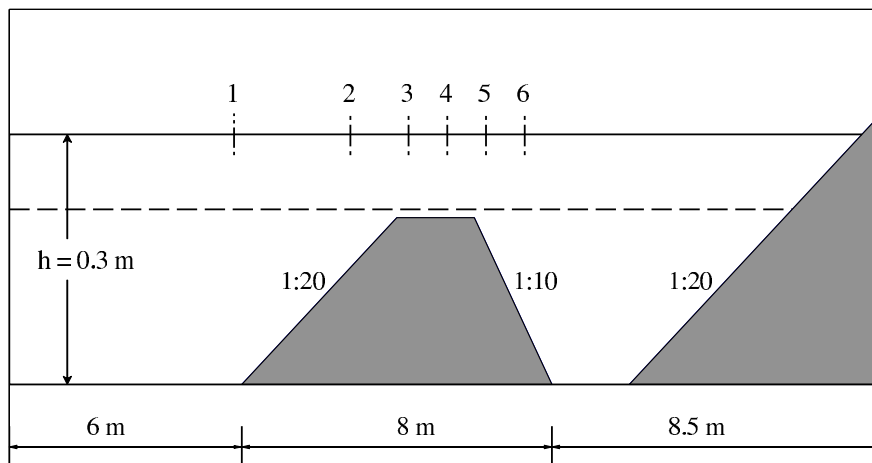
Figure 5.6. Bottom geometry of the wave flume and gauge locations in the experiment of Nadaoka et al. (1994). Layer interface of the two-layer model (dashed line).

The physical experiments of wave propagation over a submerged bar (e.g., Beji and Battjes, 1993; Nadaoka et al., 1994) have been widely used to examine the performance of Boussinesq-type and non-hydrostatic models for simulating nonlinear and dispersive waves (e.g., Stelling and Zijlema, 2003; Roeber et al., 2010). In this study, we verify the improved capability of a two-layer non-hydrostatic model over a depth-integrated non-hydrostatic model using the experiment of Nadaoka et al. (1994). A 0.3 m high trapezoidal bar with an offshore slope 1:20 and a shoreward slope 1:10 is located between 6 and 14 m

in the flume. The incident sinusoidal waves with wave height of 0.02 m and wave period of 1.5 s are generated at the offshore boundary based on the linear wave theory. The time series of free surface elevations were recorded at several gauges. For the two-layer simulation, the horizontal layer interface is located at $z = -0.09$ m, as indicated in Figure 5.6. In the numerical simulation, the computation domain is discretized with mesh sizes $\Delta x = \Delta y = 1.25$ cm, and a numerical time step $\Delta t = 0.005$ s is used. The shoreward wave absorbing plane beach in their experiment is replaced by a radiation boundary condition to minimize the wave reflection at the outlet. The numerical simulation is run long enough to obtained a steady wave field.
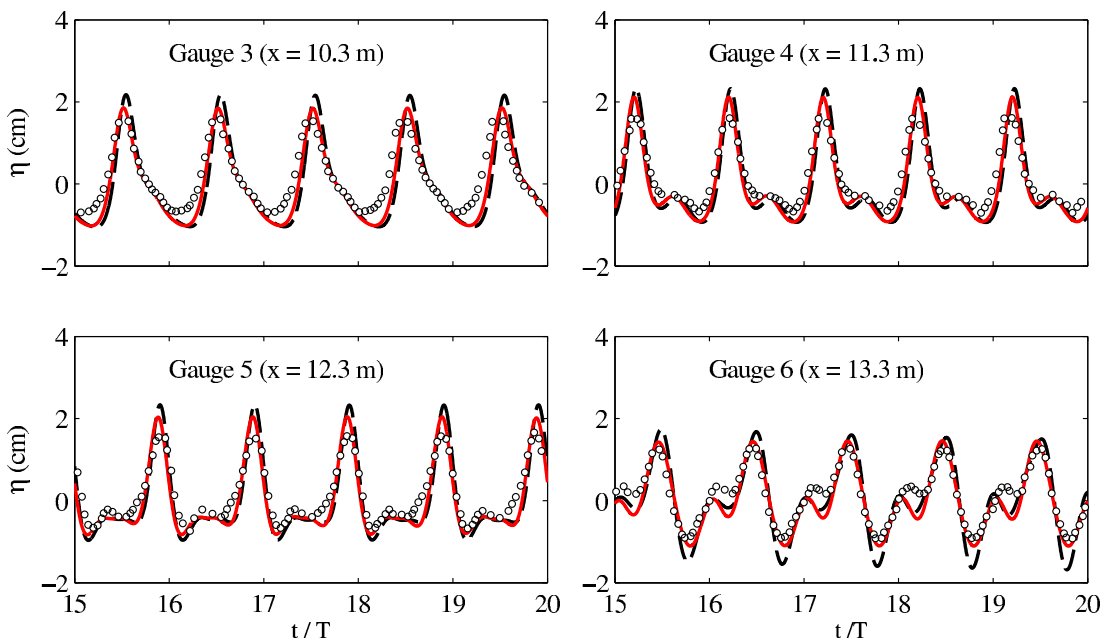
Figure 5.7. Comparison of simulated and measured time series of free surface elevations in the experiment of Nadaoka et al. (1994). Experimental data (circles), numerical results with a depth-integrated model (dashed lines), numerical results with a two-layer model (solid lines)

Figure 5.7 shows the comparison of simulated and measured time series of free surface elevations in five wave periods at four wave gauges. For the numerical simulation, both a depth-integrated model and a two-layer non-hydrostatic wave models are used. As the wave propagates over the offshore slope, the wave shoaling effect is observed. At the top of the

submerged bar, the waveform has a steeper offshore slope and a minor wave trail, which is presented in Gauges 3 and 4. Numerical models correctly capture this phenomenon, and the two-layer model shows a slight improvement on the wave height prediction. Once the wave propagates over the horizontal top of the bar and reaches the lee side of the slope, the waveform changes as the wave depth increases. As a result, it has a steeper shoreward slope and a wave trail in the offshore side, and the wave trail becomes more obvious as the water becomes deeper. At Gauges 5 and 6, although both models capture the correct shape of the waveform, the two-layer model gives a better prediction of wave height than the depth-integrated model does. This is particularly true at Gauge 6, where the trapped wave transforms into a higher dispersive wave.

5.4   Chapter Summary

This chapter has presented the formulation, verification, and validation of a multi-layer non-hydrostatic model. In the current implementation, the multi-layer model was extended from the depth-integrated non-hydrostatic model with several strictly horizontal vertical layers. A provisional velocity field is first obtained without considering the non-hydrostatic pressure, and then the divergence-free velocity condition is enforced by computing non-hydrostatic pressure, which is immediately used to correct the provisional velocity. Finally, the free surface elevation is solved by satisfying global mass conservation.

Several benchmark tests were carried out to verify and validate the improved capability of the multi-layer model over that of the depth-integrated model. Overall, comparison of numerical results with analytical solutions and experimental data shows the former is able to provide a better prediction when highly nonlinear waves and highly dispersive waves are considered.

89

CHAPTER 6

NON-HYDROSTATIC MODEL APPLICATIONS

This chapter presents the application of the depth-integrated non-hydrostatic finite element model, CCHE2D-NHWAVE, for simulating several types of coastal wave processes. Specifically, the model is applied to (1) predict the swash zone hydrodynamics involving wave bore propagation, (2) resolve wave propagation, breaking, and overtopping in fringing reef environments, (3) study the vegetation effect on wave height reduction through both submerged and emergent vegetation zones using the drag force term technique, and (4) simulate tsunami wave breaking in the nearshore zone and inundation in the coastal area. Satisfactory agreement between numerical results and benchmark data shows that the non-hydrostatic model is capable of modeling a wide range of coastal wave processes. Furthermore, thanks to its simple numerical formulation, the non-hydrostatic model also demonstrates a better computation efficiency when comparing with other numerical models.

In the following sections, we present numerical investigations of four types of coastal wave processes using CCHE2D-NHWAVE. Each of the sections is structured as follows. A brief introduction presenting the importance of the physical process analyzed is given first. Then the physical experiment and numerical model setup is described. Next, the numerical results are presented and compared with existing experimental data. Finally, a short conclusion is drawn for the test case.

6.1 Bore-driven Swash Hydrodynamics

The swash zone is the upper part of the beach between the backbeach and the surf zone, in which the beach face changes rapidly. In general, the swash process consists of two phases: uprush (onshore flow) and backwash (offshore flow). The uprush is mainly generated by a broken wave, and it is in the form of a collapsed bore on the beach slope. Usually the uprush velocity can be very high, up to 5 m/s according to Hughes (1992), and the wave run-up can reach several meters along the slope. Several field investigations (e.g., Puleo et al., 2000; Austin and Masselink, 2006) showed that the swash zone of steep beaches is a highly dynamic and complex regime as the flow is turbulent, unsteady, and non-uniform, and the sediment flux is high and varying along it. To better understand the fundamental processes of hydrodynamics and sediment transport in the swash zone, several well controlled physical experiments were carried out to measure the velocity, shear stress, and subsurface process; see Barnes et al. (2009) and O'Donoghue et al. (2010), among others. In this study, we simulate a flume experiment on a bore-driven swash hydrodynamic process reported by O'Donoghue et al. (2010).

6.1.1 Experimental and numerical setup
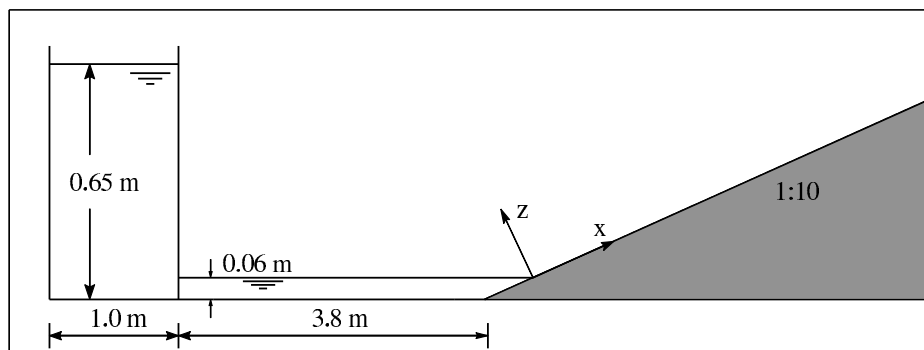
Figure 6.1. Definition sketch of bore-driven swash hydrodynamics experiment.

The experiment was carried out in the Fluid Mechanics Laboratory at the University of Aberdeen, UK. The experiment rig was built into an existing 20 m long, 0.9 m high and 0.45 m wide, glass-sided flume. A 0.65 m high and 1.0 m long water reservoir was placed at

91

one end of the flume with a gate that can be lifted at a high speed to generate a bore. And then the bore, which mimics the broken wave from the surf zone, propagates over a 3.8 m long shallow water region with a water depth of 0.06 m. Finally it runs up a 1:10 slope at the other end of the flume (see Figure 6.1). In the experiment, two types of slopes were considered. For the "smooth" beach experiment, the slope consisted of clear perspex panels fixed onto a rigid aluminum frame with good sealing between the panels and the glass sides of the flume. For the "rough" beach experiment, the slope was made by uniformly gluing a layer of well-sorted, rounded pebbles with a size range from 5 to 6 mm onto the perspex panels. For both cases, velocity and water depth were measured at five locations along the slope.

In the numerical simulation, the computation domain is discretized with mesh sizes $\Delta x = \Delta y = 0.01$ m. The numerical simulation starts from the initial gate opening, and the total simulation time is about 12 s with a numerical time step $\Delta t = 0.001$ s. With respect to the numerical boundary condition, the reflective wall boundary condition is applied at the reservoir wall side, and the radiation boundary condition is applied at the slope end. It is well-known that the hydrodynamic (non-hydrostatic) pressure is only dominant at the initial stage of dam breaking flows, and the propagation of the resulting broken wave could be well simulated by a NLSW model (e.g., Stansby et al., 1998; Zhou et al., 2004). Therefore, we apply CCHE2D-NHWAVE with the hydrostatic pressure approximation to simulate the bore-driven swash hydrodynamics for this test.

Previously, O'Donoghue et al. (2010) simulated this set of experiments with a 1D shock-capturing NLSW model. A momentum "sink" term with an adjustable parameter was introduced to represent the lumped effect of momentum loss due to the bed shear stress, streamwise turbulent momentum diffusion, and depth-wise non-uniformity of the velocity. In this study, there are two terms that are able to account for the momentum loss and the energy dissipation in the governing equations, one is the bed friction term using the Manning coefficient, the other is the turbulent stress term with a turbulent kinematic viscosity con-

sidering the horizontal exchange of momentum, see Chapter 4 for details. Initial numerical simulation showed that the presence of the turbulence stress term almost has no effect on the numerical result, since (1) the turbulence may not fully develop in so short of time, and (2) the turbulent kinematic viscosity is much smaller than the Manning coefficient. As a result, similar to the work of O'Donoghue et al. (2010), we parameterize the total momentum loss through the bed friction term and with a calibrated parameter in the form of the Manning coefficient. Under this assumption, the only difference between the smooth slope case and the rough slope case in the numerical model is the calibrated friction parameter.

6.1.2   Smooth slope

For the smooth slope case, the flume bottom and the slope were made of perspex, resulting in a Manning coefficient $n \approx 0.01$ (Munson et al., 2002). First of all, we present the comparison of the numerical result using $n = 0.01$ with the experimental data in Figure 6.2. It shows that numerical simulation is able to predict the arrival time of the bore at the first gauge since the roughness of the shallow water region is correctly implemented. However, the predicted arrival time at the rest of gauges is earlier than the measurement. This is because the model doesn't consider the momentum loss beyond that part due to the bed friction. Next, we use a calibrated friction parameter $n = 0.02$ by considering the overall agreement between the numerical result and the measurement and present the comparison of simulated and measured water depth and velocity in Figure 6.2. The numerical model with $n = 0.02$ captures several important features during the uprush and backwash processes. First of all, from the water depth comparison, the arrival time of the bore at all gauges is correctly predicted by the model. In addition, the transition from the uprush to the backwash (i.e., the velocity changes its sign from positive to negative) is also well simulated.
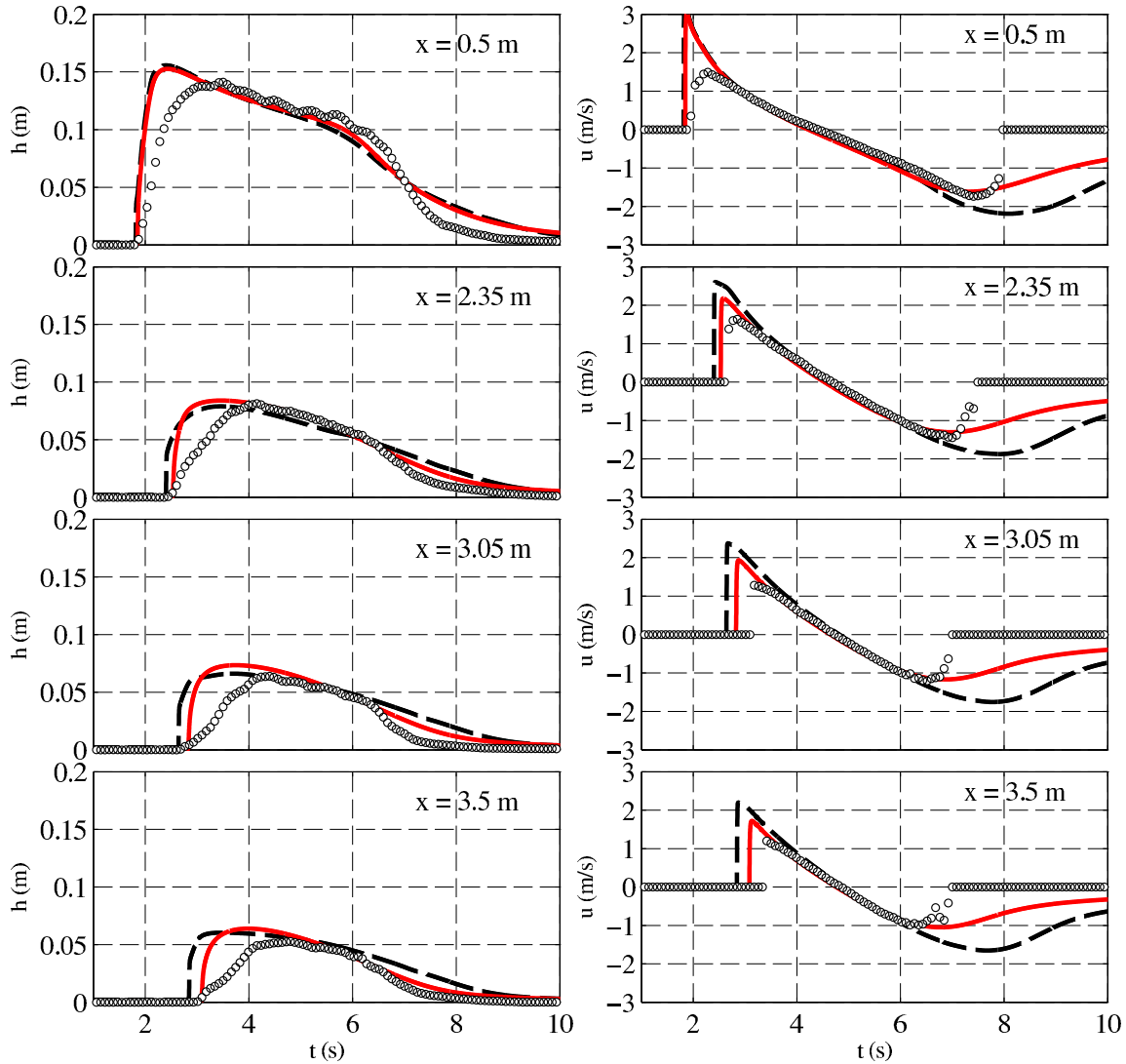
Figure 6.2. Comparison of simulated and measured water depth (left panel) and velocity (right panel) for a bore collapse on a steep smooth beach. Experimental data (circles), numerical results with $n = 0.02$ (solid lines), numerical results with $n = 0.01$ (dashed lines).

However, there are also several significant differences between the simulation and the measurement. The most obvious one is the increase rate of water depth and velocity at that time when the bore arrives at the gauges. The predicted water depth increases faster than the measurement does, and the predicted velocity is also larger than the measurement. These discrepancies are mainly due to two reasons. The first one is related to the numer-

94

ical approximation of the momentum loss in the governing equation. A constant friction parameter has been used in the numerical model for the whole computation domain and at all stages of bore propagation. Although the model successfully describes the momentum and energy loss during most of the swash process, it may underestimate the momentum loss at the arrival time of the bore. Furthermore, the difference may also be attributed to the experiment measurement. As pointed out by O'Donoghue et al. (2010), due to high velocities, high turbulence levels, and high percentage of air entrainment at the bore front, the experiment measurements are less reliable than the data measured in a normal condition. Another difference between the simulation and the measurement is the velocity profile in the period of backwash. The numerical model predicts a gradual decay process of velocity while the measurement decreases rapidly. In the physical experiment, the water depth is very small at the backwash stage, and therefore, it might be too shallow to measure the velocity (O'Donoghue et al., 2010).

6.1.3 Rough slope

For the rough slope case, the slope was covered by well-sorted pebbles with the size range from 5 to 6 mm, and the Manning coefficient of the rough bed could be estimated by the following formula (Wu, 2007):

$$n = \frac{d^{1/6}}{A_n} \tag{6.1}$$

where d is the pebble size in meter, and A_n is a roughness parameter, $A_n = 20$ is used in this study. From Equation (6.1), we obtain the converted Manning coefficient $n \approx 0.021$. Next, we compare the numerical result with this value with the measurement in Figure 6.3. Similar to the smooth bed case, the arrival time at the gauges along the slope is not correctly predicted. And then we parameterize the lumped momentum loss by using another calibrated friction parameter $n = 0.028$ and rerun the simulation. The comparison between the simulated and measured water depth and velocity is also shown in Figure 6.3. In general, the observations summarized in the smooth slope case are applicable to the rough one. An

extra discrepancy is that the velocity during the uprush and backwash processes is slightly underpredicted.
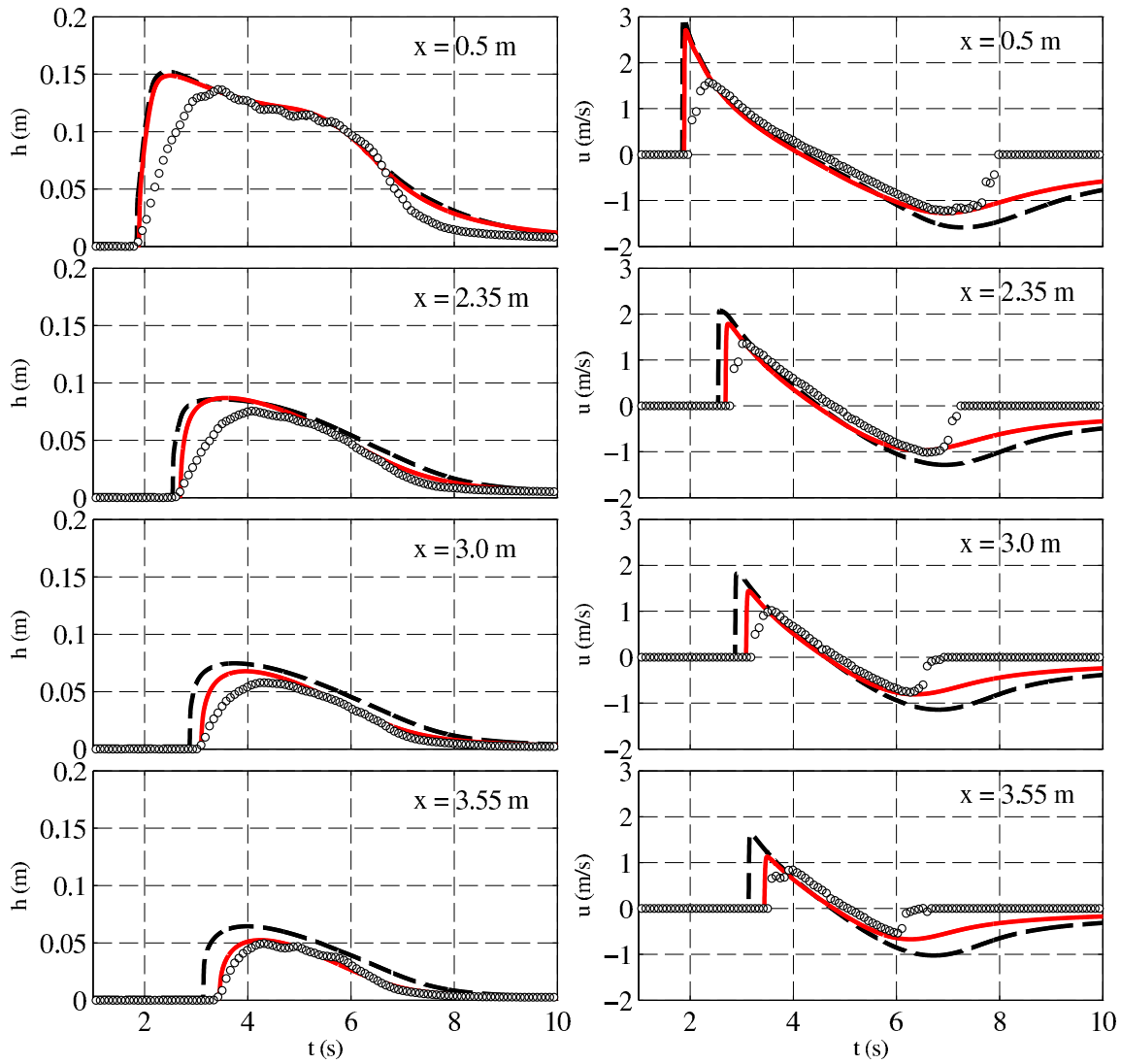
Figure 6.3. Comparison of simulated and measured water depth (left panel) and velocity (right panel) for a bore collapse on a steep rough beach. Experimental data (circles), numerical results with $n = 0.028$ (solid lines), numerical results with $n = 0.021$ (dashed lines).

In summary, the hydrostatic version of CCHE2D-NHWAVE, i.e., a NLSW model with mass and momentum conservation, has successfully simulated a bore-driven swash hydrodynamic event with a simple calibrated friction coefficient to approximate the momentum

loss. In general, the numerical result presented here is comparable to that of O'Donoghue et al. (2010). Because a constant parameter may not realistically represent the momentum and energy loss in different time periods and wave propagation stages, the depth-integrated model overpredicted the water depth and the velocity at that time when the bore arrives at the gauges. However, several important physical processes (e.g., the arrival time of the bore, and the transition from the uprush to the backwash) have been well captured.

6.2 Wave Transformation in Fringing Reef Environments

Fringing reef is one of the most common type of coral reefs found in the tropical and sub-tropical regions over the world. It is usually characterized by a steep seaward reef face and an inshore shallow reef flat extending toward the coastline. As the wave propagates over the fringing reef, wave energy is dissipated by wave breaking at the front of the reef face, and the wave could be further attenuated by the rough reef flat before approaching the coastal area (Lugo-Fernández et al., 1998; Brander et al., 2004). As a consequence, the fringing reef is a great natural barrier to reduce wave action on coastal structures and coastal inundation.

In the past decades, considerable efforts have been made to improve the understanding of the physical process of wave transformation over fringing reefs. When the numerical model is applied to address this issue, there are several challenges. First of all, to obtain the correct prediction of wave transformation from deep water to shallow water through the steep reef slope, the numerical model has to deal with the nonlinearity and frequency dispersion properly (Roeber et al., 2010). In addition, as the wave breaks energetically over the fringing reef, it also requires the numerical model to be able to handle discontinuous flows (Roeber and Cheung, 2012). In this study, we evaluate the capability of CCHE2D-NHWAVE for simulating wave transformation over fringing reefs by comparing numerical results with experimental data obtained in a large-scale wave flume.
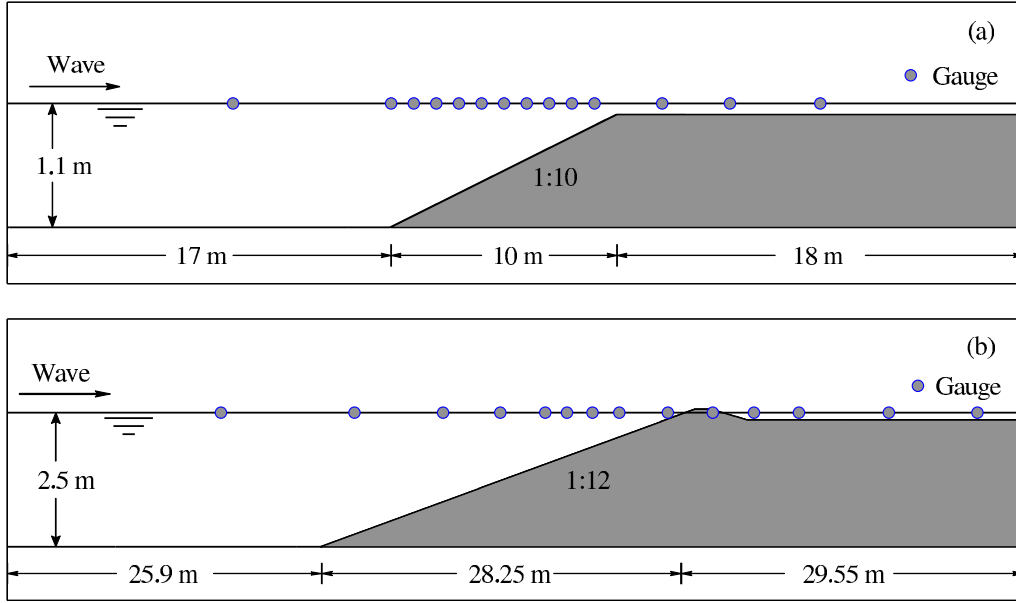
Figure 6.4. Definition sketch of wave transformation over a fringing reef experiment. (a) wet reef flat, and (b) exposed reef crest.

6.2.1 Experimental and numerical setup

Two series of laboratory experiments on solitary wave transformation over idealized fringing reefs were reported by Roeber et al. (2010) and Roeber and Cheung (2012). The experimental data was collected at the O. H. Hinsdale Wave Research Laboratory of Oregon State University, USA, in 2007 and 2009. This study considers two cases which were conducted in two separate wave flumes. The first case was conducted in a 48.8 m long, 2.16 m wide, and 2.1 m high flume with an effective length of 45 m. The flume bed configuration included an offshore flat, a fore reef with a 1:10 slope beginning at $x = 17.0$ m, and a flat reef. The considered case involves a solitary wave of wave height $A = 0.1$ m, a still water depth h $= 1.1$ m resulting in $A/h = 0.09$, and a wet reef flat (see Figure 6.4(a)). The other case was conducted in a 104 m long, 3.66 m wide, and 4.57 m high flume with an effective length of 83.7 m. The flume bed configuration consisted of an offshore flat, a fore reef with a 1:12 slope beginning at $x = 25.9$ m, and a 0.2 m high reef crest. The test condition includes a solitary wave of wave height $A = 0.75$ m, a still water depth $h = 2.5$ m resulting in $A/h = 0.3$, an exposed reef crest by 6 cm, and a lagoon with a water depth of 14 cm (see Figure 6.4(b)).

98

In the numerical simulation, the computational domain of both cases is discretized with mesh sizes $\Delta x = \Delta y = 0.05$ m. The numerical time step is $\Delta t = 0.005$ s, and the bed surface roughness is approximated by a Manning coefficient $n = 0.012$ for the wet reef flat case and $n = 0.016$ for the exposed reef crest case.

6.2.2   Wet reef flat
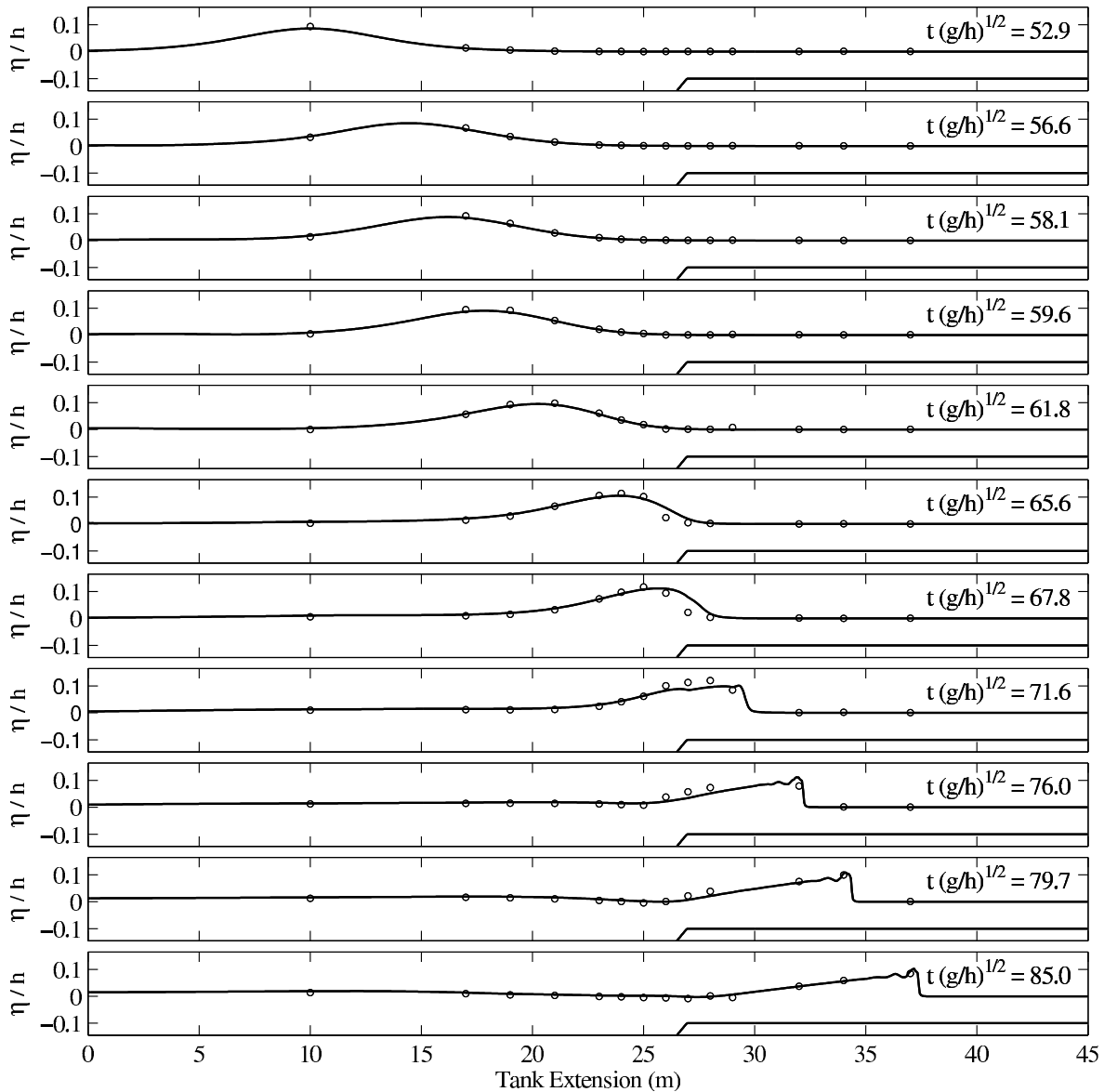
Figure 6.5. Comparison of simulated and measured free surface elevations for a solitary wave propagation over a wet reef flat. Experimental data (circles), numerical results (solid lines).

Figure 6.5 shows the comparison of simulated and measured free surface elevations for a solitary wave propagation over a wet reef flat. Before the wave reaches the reef slope, it maintains a constant wave height, and the agreement between the simulation and the measurement is very good. Once the wave approaches the slope, the initially symmetric wave form begins to skew, and the wave front becomes steeper. The numerical model successfully captures the transition process with a slight overprediction at the wave front. As the wave surges over the reef flat, it decays into a train of short undulations and only breaks further back over the reef flat. When a numerical model is applied to this case and other similar data sets, the challenging part is to correctly reproduce the waveform without showing a phase shift (i.e., the waveform is predicted correctly but the phase of the numerical result lags behind that of the measurement [1]). It is recognized that CCHE2D-NHWAVE predicts the waveform fairly well, especially, the wave front is correctly captured as the wave propagates toward the wall.

6.2.3 Exposed reef crest

For the exposed reef crest case, the solitary wave breaks energetically as it propagates over the reef crest, and therefore CCHE2D-NHWAVE is applied together with the hydrostatic front approximation (HFA) scheme of Smit et al. (2013) to locally switch the numerical model from the non-hydrostatic model to a NLSW model at the breaking wave front. Figure 6.6 shows the comparison of simulated and measured free surface elevations for a solitary wave propagation over a fringing reef with an exposed reef crest. As the wave propagates over the reef slope, the wave front becomes steeper and gradually develops into a near vertical profile to break around $t\,(g/h)^{1/2} = 67$. In the experiment, a subsequent overturning of the free surface is observed, and a plunging breaker develops on top of the reef crest. The jet from the breaking wave hits the water surface and forms an elliptical air cavity around $t\,(g/h)^{1/2} = 70$ that shortly collapses and produces extensive air entrainment in the flow (Roeber et al.,

---

[1]Personal communication with Dr. Volker Roeber (2013), who conducted this experiment and evaluated other numerical models' performance on the same data set.

2010). In the numerical simulation, the depth-integrated model mimics the wave breaking process as a collapsing bore, and it ensures the correct free surface elevation prediction at the end of the wave breaking process by conserving mass and momentum in the formulation.
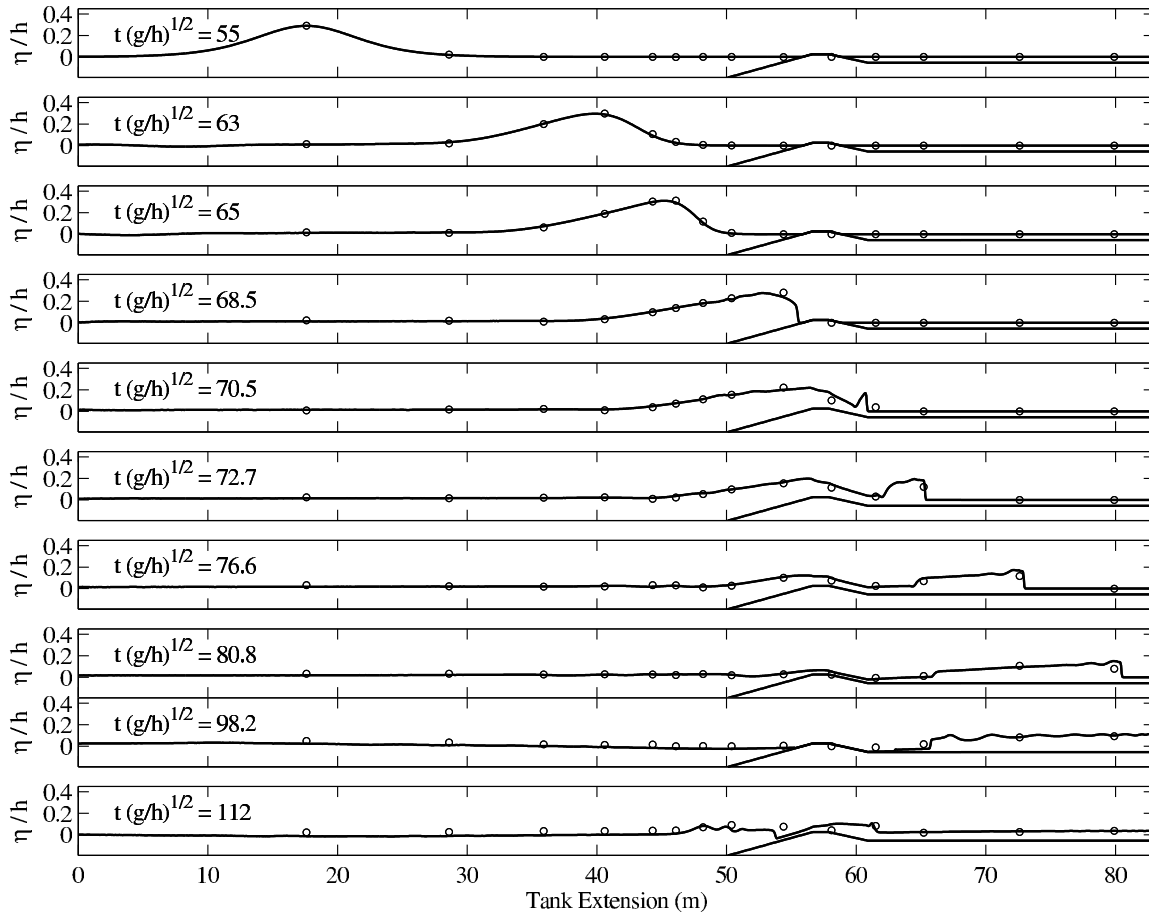
Figure 6.6. Comparison of simulated and measured free surface elevations for a solitary wave propagation over an exposed reef crest. Experimental data (circles), numerical results (solid lines).

Once the broken wave overtops the reef crest, it travels down the lee side of the slope and generates a supercritical flow, displacing the still water in the lagoon at $t\,(g/h)^{1/2} = 70.5$, and then a bore is generated as the supercritical flow transits into the subcritical flow in the form of a hydraulic jump (Roeber et al., 2010). The numerical model successfully resolves the whole process and gives satisfactory prediction. Gradually, the hydraulic jump diminishes with the flow and travels toward the wall at the end of the flume. The numerical model

101

correctly predicts the diminishing process and captures the evolution of the wave front fairly well. Around $t\,(g/h)^{1/2} = 83$, the flow reaches the wall and it is reflected back to the lagoon in the form of a bore. The bore continues to propagate toward the exposed reef crest and overtops it again. The backward flow process is also well simulated by the numerical model. In Figure 6.7, we show the time series of free surface elevations comparison between the numerical model and the measurement at several wave gauges across the flume, the fairly good agreement confirms the correct numerical prediction of the solitary wave propagation, breaking, and reflection, as illustrated above.
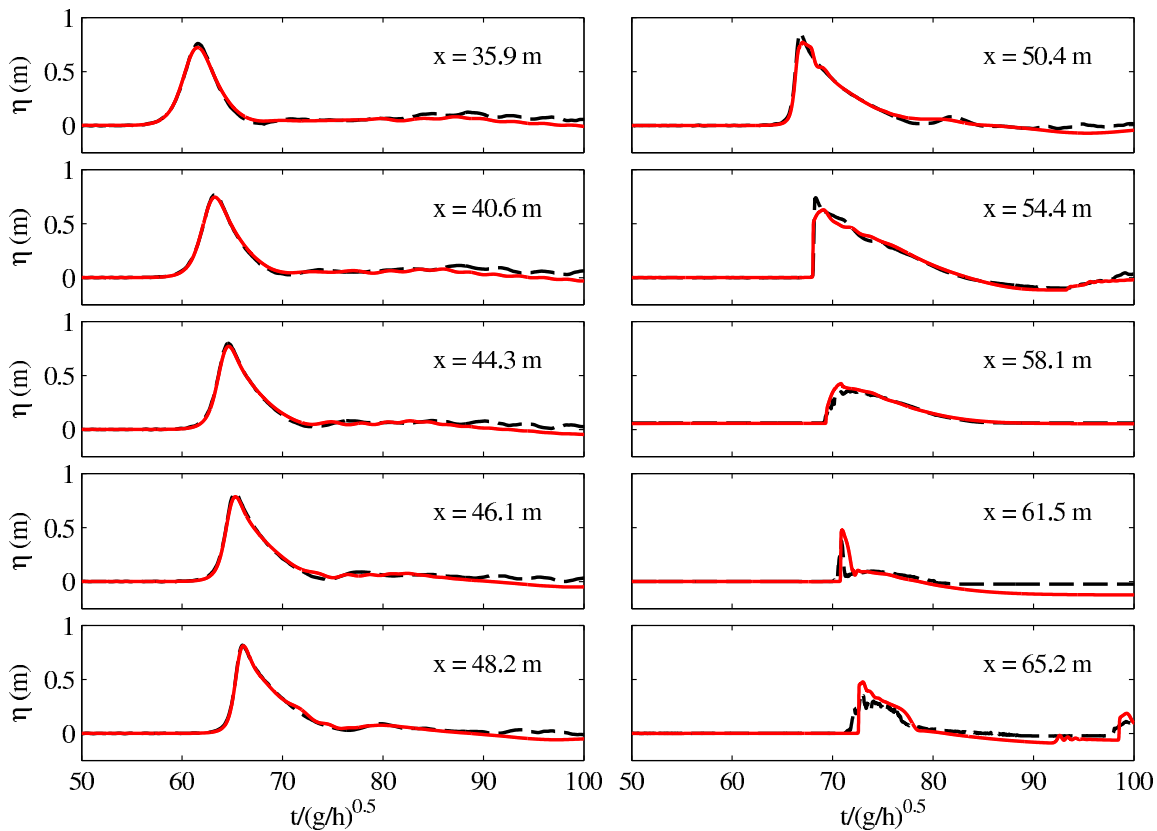
Figure 6.7. Comparison of simulated and measured time series free surface elevations for a solitary wave propagation over an exposed reef crest. Experimental data (dashed lines), numerical results (solid lines).

In summary, the capability of CCHE2D-NHWAVE for simulating wave transformation over fringing reefs with steep slopes is validated by comparing with experimental data collected in a large-scale wave flume. The use of the non-hydrostatic pressure is important to

resolve the wave dispersion, and conservation of mass and momentum is essential to ensure correct prediction of discontinuous flows (e.g., wave breaking). Furthermore, the efficiency of the wetting and drying algorithm is also verified.

6.3   Wave Attenuation by Vegetation

Traditionally, coastal protection typically has involved construction of hard structures, such as levees, floodgates, jetties, and breakwaters. Although these structures can significantly reduce wave damage on the coastal area, they may also change the regional hydrodynamic process, coastal morphology, and even cause aquatic system disasters. Recently, the role of vegetation in reducing wave hazard in the coastal zone has received more and more attention because vegetation is able to provide sustainable and non-intrusive protection. So far, considerable efforts have been made to study the interaction between vegetation and waves (see, e.g., Dalrymple et al., 1984; Asano et al., 1988; Li and Yan, 2007; Wu et al., 2012; Maza et al., 2013, among others), but the detailed mechanics of wave attenuation by vegetation is still not well understood due to the dynamic nature of wave forcing and spatial and temporal variations of vegetation distribution during the interaction. In this study, we enhance CCHE2D-NHWAVE to simulate wave attenuation by vegetation.

When it comes to numerical investigations of wave attenuation by vegetation, one important thing is to quantify the resistance of vegetation on current and waves in the governing equations. A widely adopted approach is to represent the vegetation effect in the momentum equation by adding extra drag and inertia forces (e.g., Li and Yan, 2007; Wu et al., 2012; Maza et al., 2013) in the following form:

$$\frac{\partial u}{\partial t} + \cdots = -\frac{1}{\rho}(F_D + F_i) \tag{6.2}$$

where t is the time; u is the flow velocity; ρ is the water density; F_D is the drag force; F_i is the inertia force. Since the inertia force is usually much smaller than the drag force, it is
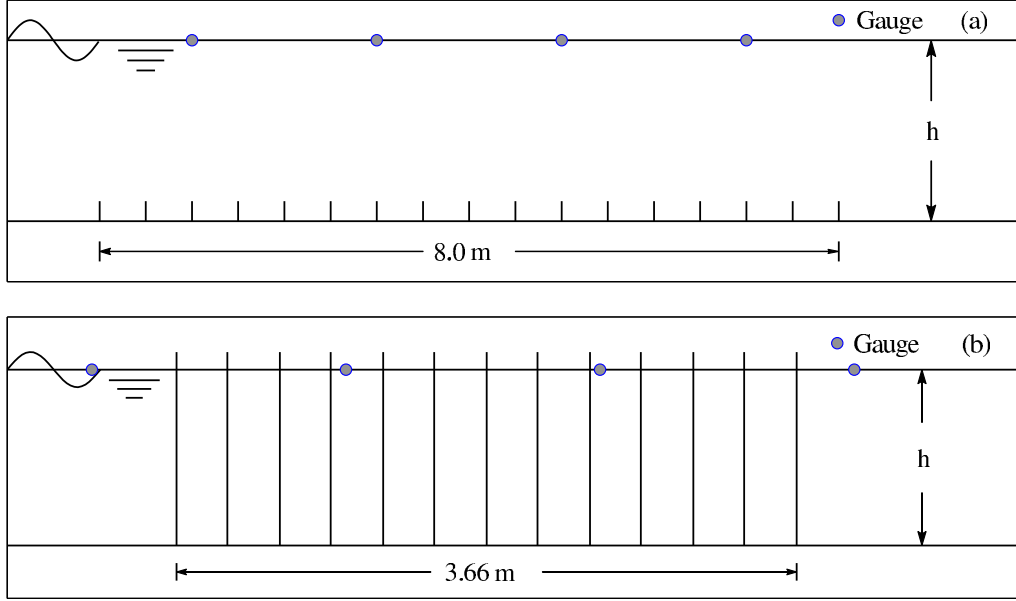
Figure 6.8. Definition sketch of wave attenuation by vegetation experiment. (a) experiment of Asano et al. (1988), and (b) experiment of Wu et al. (2012).

ignored in this study. And the drag force is defined by

$$F_D = \frac{1}{2}\rho C_D N_v A_v u \, |u| \tag{6.3}$$

where C_D is the drag coefficient, N_v is the vegetation density defined as the number of vegetation elements per unit horizontal area, and A_v is the projection width (or area per unit height) of each vegetation stem, defined as the frontal width of a vegetation element projected to the plane normal to the streamwise flow direction (Wu et al., 2012).

To solve Equation (6.2), the drag coefficient C_D needs to be determined. Although several factors, e.g., (1) turbulence of the flow, (2) non-uniform velocity profile, (3) free surface, (4) blockage, and (5) vegetation density, were identified to influence the determination of C_D (e.g., Li and Shen, 1973; Nepf, 1999), the drag coefficient is usually determined by calibration using experimental data in the numerical model. As a result, the drag coefficient value used varies from one model to another. In this study, we avoid this by using a single C_D among different cases when their experimental setups are similar, and the results show

Table 6.1. Experimental condition of Asano et al. (1988).

NO.	Wave condition			Vegetation			C_D	
	h (m)	T (s)	H (m)	h_v (mm)	N_v (1/m^2)	A_v (m)	This work	Maza et al. (2013)
a	0.45	1.43	0.134	0.03	1490	0.052	0.035	0.11
b	0.45	1.43	0.084	0.03	1490	0.052	0.035	0.15
c	0.45	2.0	0.039	0.03	1100	0.052	0.048	0.23
d	0.45	2.0	0.063	0.03	1100	0.052	0.048	0.16

that satisfactory agreement can also be obtained.

6.3.1 Experimental and numerical setup

Two laboratory experiments on wave attenuation by vegetation are used to validate the numerical model. The first one was carried out by Asano et al. (1988) in a 27 m long, 0.5 m wide and 0.7 m high flume. Vegetation was mimicked by polypropylene strips with a specific gravity of 0.9. Each of the strips was 25 cm long, 5.2 cm wide and its thickness is h_v= 0.03 mm. The total length of the artificial vegetation zone was 8 m (see Figure 6.8(a)). Several water depths were tested in their experiment, here we only consider the one with $h = 0.45$ m. As a result, the vegetation is submerged. Furthermore, two kinds of vegetation density are considered. Four cases total with different wave conditions are simulated in this study, as listed in Table 6.1.

The other set of experiments considered was reported by Wu et al. (2012). The experiment was carried out in a 20.6 m long, 0.69 m wide, and 1.22 m deep wave flume at the USDA-ARS National Sedimentation Laboratory in Oxford, Mississippi, USA. Several types of vegetation were tested in their experiment. Here we only consider the rigid model vegetation made of birch dowels with a diameter of 9.4 mm, and a stem height $h_v = 0.63$ m. The total length of the vegetation zone is 3.66 m (see Figure 6.8(b)). The numerical model considers two water depths, $h = 0.5$ m and 0.7 m. As a result, the vegetation is emergent for the lower water depth case and submerged for the higher one. We also test two kinds

Table 6.2. Experimental condition of Wu et al. (2012).

NO.	Wave condition			Vegetation			C_D	
	h (m)	T (s)	H (m)	h_v (m)	N_v ($1/m^2$)	A_v (mm)	This work	Wu et al. (2012)
a	0.5	1.0	0.1	0.63	350	9.4	3.0	2.0
b	0.5	1.0	0.1	0.63	623	9.4	3.0	2.05
c	0.7	1.2	0.052	0.63	350	9.4	3.0	1.35
b	0.7	1.2	0.052	0.63	623	9.4	3.0	2.3
e	0.7	1.1	0.117	0.63	350	9.4	3.0	1.8
f	0.7	1.1	0.117	0.63	623	9.4	3.0	1.9

of vegetation density in the second experiment. In this study, six cases with different wave conditions are simulated, as listed in Table 6.2.

In the numerical simulation, the computation domain of both experiments is discretized with mesh sizes $\Delta x = \Delta y = 0.02$ m, and the numerical time step is $\Delta t = 0.002$ s. The numerical model is run long enough to obtain a steady solution, and the wave height is calculated using the last ten wave periods.

6.3.2   Experiment of Asano et al. (1988)

Figure 6.9 shows the comparison of simulated and measured wave height across the vegetation zone of the experiment of Asano et al. (1988). The four cases considered can be roughly categorized into two groups based on their wave periods and vegetation densities. As a result, a $C_D = 0.035$ is used for the first group and another $C_D = 0.048$ is used for the second group by evaluating the overall agreement between the numerical results and the measurements. The model provides a reasonable estimate for the amount of wave height attenuated by the vegetation for a wide range of incident wave heights.

6.3.3   Experiment of Wu et al. (2012)

Figure 6.10 shows the comparison of simulated and measured wave height across the vegetation zone of the experiment of Wu et al. (2012). Since the height of the stem used is about 0.63 m, the vegetation in the first two cases is emergent, and the vegetation in
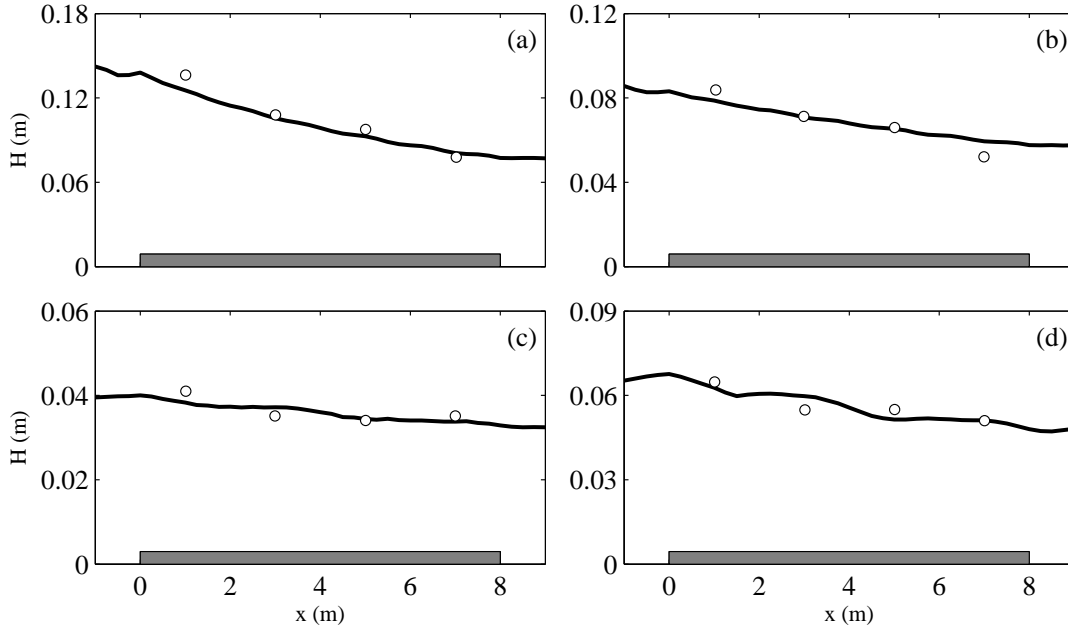
Figure 6.9. Comparison of simulated and measured wave height of experiment of Asano et al. (1988). Experimental data (circles), numerical results (solid lines), vegetation zone (gray area).

the last four cases is submerged. It is observed that there is no large variation of incident wave periods, and the differences of vegetation density are also not significant, so this study only uses $C_D = 3.0$ for all cases. The numerical model reproduces the experiment fairly well. A slight reflection is predicted by the numerical model in all cases, and the amount of reflection depends on the incident wave conditions and the vegetation properties. This phenomenon was also reported by Wu et al. (2012) using a vertical 2D RANS model with the Volume-of-Fluid method (Hirt and Nichols, 1981) for free surface tracking.

In summary, with the implementation of the drag force term technique, CCHE2D-NHWAVE has successfully predicted the wave attenuation by vegetation collected in two large-scale wave flumes. This study shows two improvements over previous research. The first one is the determination of the drag coefficient. Compared with widely used case-by-case drag coefficients, e.g., those used in Maza et al. (2013) and Wu et al. (2012) and reproduced in Tables 6.1 and 6.2, this model attempts to use a single drag coefficient in view of the similarity of incident wave conditions and vegetation properties among different cases. The
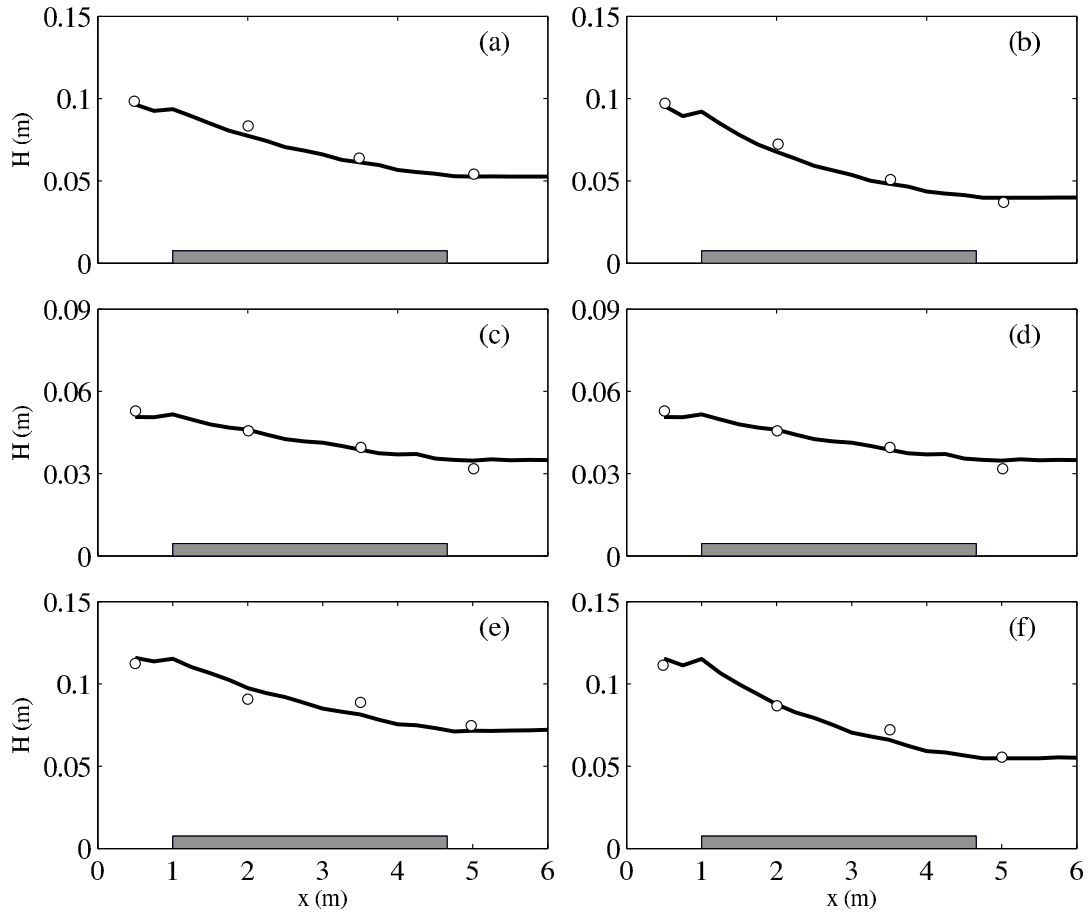
Figure 6.10. Comparison of simulated and measured wave height of experiment of Wu et al. (2012). Experimental data (circles), numerical results (solid lines), vegetation zone (gray area).

other improvement is related to simulation of short waves using the non-hydrostatic model. Previously, a very fine vertical resolution (e.g., 0.02 m used in the RANS models of Maza et al. (2013) and Wu et al. (2012)) was needed to obtain satisfactory results, however, the non-hydrostatic model is able to provide comparable results with only one vertical layer.

6.4 Tsunami Wave Breaking on a 3D Reef

A tsunami is a relatively long period wave generated by a variety of underwater disturbances including earthquakes, landslides, and volcanic eruptions. It is among the deadliest natural disasters in human history, e.g., the 2004 Indian Ocean tsunami, which killed almost 230,000 people in eleven countries across the Indian Ocean. Although a tsunami

is usually generated in the deep ocean, its impact is mainly limited to coastal areas in the form of coastal erosion and inundation. To reduce tsunami damage, there is an urgent need to better understand the tsunami wave process and impact in the nearshore and coastal zones.

Owing to the nature of a tsunami event, it is very difficult to directly observe it in the field. In the past, analytical solution (e.g., Carrier and Greenspan, 1958; Carrier et al., 2003), laboratory experiment (e.g., Briggs et al., 1995; Enet and Grilli, 2007; Swigler, 2009), and numerical simulation (e.g., Titov and Synolakis, 1998; Fuhrman and Madsen, 2009; Zijlema et al., 2011) have been widely used to study the full process of a tsunami wave, including its generation in the deep ocean, propagation in the continental shelf, breaking in the nearshore zone, and inundation in the coastal area. Usually, the analytical solution is only applicable to simplified problems, and the laboratory experiment is able to reproduce some specific processes (e.g., generation, propagation, and run-up) of a tsunami in a well controlled condition, while the numerical model is able to deal with more realistic wave forms and bathymetries, and even a real-life tsunami (e.g., Grilli et al., 2013). In this study, we numerically investigate the nearshore tsunami wave process involving energetic wave breaking and inundation by simulating recently collected benchmark data for the tsunami study.

6.4.1 Experimental and numerical setup

This experimental data of solitary wave transformation over a 3D reef was reported by Swigler (2009), and it was conducted in the Tsunami Wave Basin at the O. H. Hinsdale Wave Research Laboratory of Oregon State University, USA. The data was considered as the benchmark test of the 2009 Inundation Science & Engineering Cooperative Community Workshop held in Corvallis, Oregon. The basin is 48.8 m long, 26.5 m wide and 2.1 m deep with a piston-type wave maker for generation of the incident tsunami-like wave (i.e., solitary wave) in the experiment.
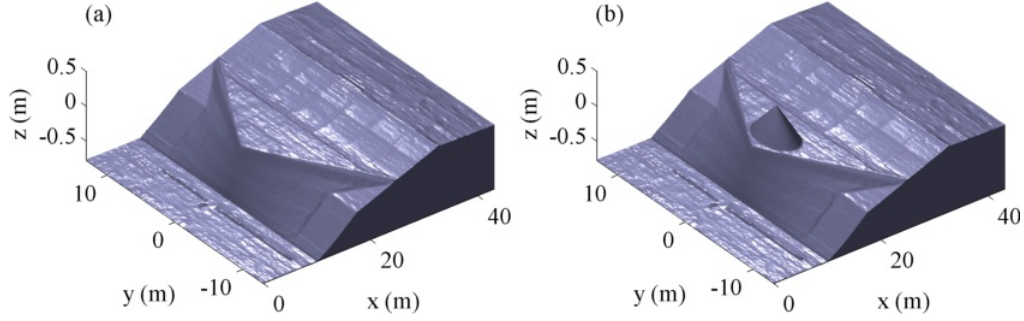
Figure 6.11. Bathymetry of the experiment of Swigler (2009). (a) Case I, and (b) Case II.

Two cases denoted as I and II, with the same incident wave condition and different bathymetries, are considered in this study. The walls and underlying bathymetry of the basin were made of concrete to reduce boundary effects due to friction. Figure 6.11(a) shows the bathymetry of Case I, which was determined from a laser scan. The experimental coordinate system was as follows: $x = 0$ m at the wavemaker and increases positively in the direction of wave propagation; $z = $ -0.78 m at the basin floor in the constant depth portion of the basin near the wavemaker and increases positively upwards; $y = 0$ m at the centerline of the basin and increases positively parallel to the wavemaker. Opposite the wavemaker, a complex shallow water bathymetry was built to force the wave to break symmetrically about the centerline of the basin. First, a 1:30 slope planar beach was constructed, which began at $x = 10.2$ m and extended to $x = 31$ m with a height of 0.95 m before becoming level and extending to the back wall of the basin. Second, beginning at the toe of the planar beach, a 3D shallow water triangular reef was built. The top of the reef was located at an elevation of $z = $ -0.07 m with the apex located at $x = 12.6$ m. In the experiment, the designed water depth 0.78 m measured from the constant depth portion of the basin was maintained. As a result, the still water shoreline intersected the planar beach at $x = 25.75$ m. Time series of free surface elevations were recorded at six gauges along the centerline, and another six gauges at 5 m offset the centerline. In addition, time series of velocities were also recorded at three gauges, as listed in Table 6.3. The bathymetry of Case II was built on that of Case I by adding an island feature using a concrete cone of 6 m diameter and 0.45 m height fitted

Table 6.3. Locations of wave & velocity gauges in Case I of Swigler (2009).

NO.	(x, y)	NO.	(x, y)
1	(7.5, 0)	9	(13, -5)
2	(11.5, 0)	10	(15, -5)
3	(13, 0)	11	(17, -5)
4	(15, 0)	12	(21, -5)
5	(17, 0)	V1	(13, 0)
6	(21, 0)	V2	(21, 0)
7	(7.5, -5)	V3	(21, -5)
8	(11.5, -5)		

Note: suffix V denotes velocity gauges; Unit: m

Table 6.4. Locations of wave & velocity gauges in Case II of Swigler (2009).

NO.	(x, y)	NO.	(x, y)
1	(7.5, 0)	7	(25, 0)
2	(13, 0)	8	(25, 5)
3	(21, 0)	9	(25, 10)
4	(7.5, 5)	V1	(13, 0)
5	(13, 5)	V2	(21, 0)
6	(21, 5)	V3	(21, -5)

Note: suffix V denotes velocity gauges; Unit: m

to the apex of the reef between $x = 14$ and 20 m, as shown in Figure 6.11(b). Similar to the measurement layout of Case I, time series of free surface elevations were recorded at nine gauges, and time series of velocities were also recorded at three gauges in Case II, as listed in Table 6.4. In both cases, the incident solitary wave has a wave height of $A = 0.39$ m, resulting in a strongly nonlinear condition with $A/h = 0.5$.

In the numerical simulation, the computation domain of both cases is discretized with mesh sizes $\Delta x = \Delta y = 0.1$ m, the numerical time step is $\Delta t = 0.005$ s, and a Manning coefficient of $n = 0.014$ is used to approximate the surface roughness. As energetic wave breaking was observed in both experiments (Swigler, 2009), CCHE2D-NHWAVE is applied with the HFA scheme of Smit et al. (2013) to numerically deal with the wave breaking process.
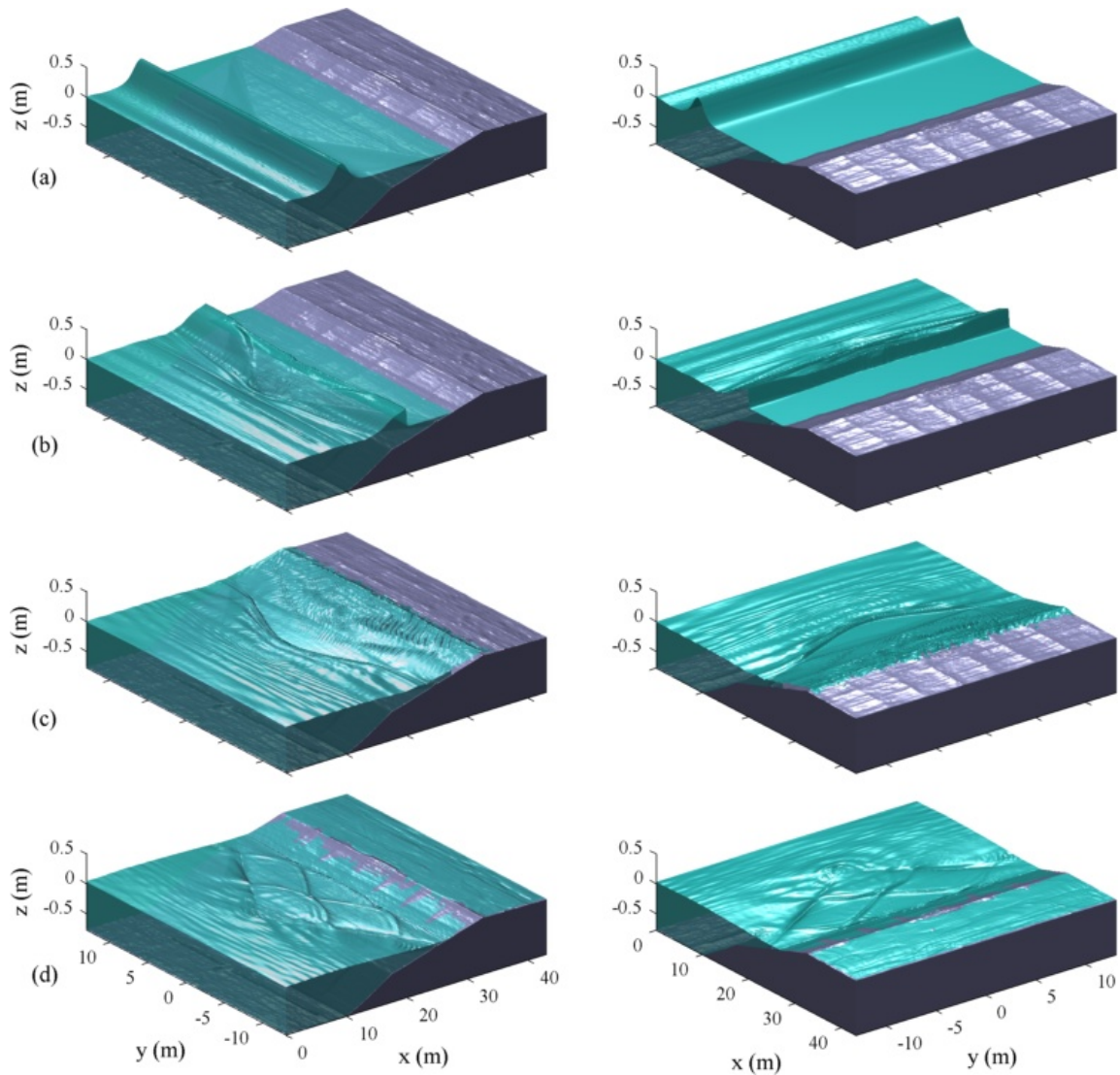
Figure 6.12. Snapshots of free surface elevations with both front and lee-side views in Case I of Swigler (2009). (a) t = 4 s, (b) t = 7 s, (c) t = 14 s, and (d) t = 29 s.

6.4.2 A triangular shaped reef

Figure 6.12 shows a series of snapshots of free surface elevations in Case I as the solitary wave propagates, breaks, runs up, and retreats over the triangular shaped reef. At $t = 4$ s, the solitary wave reaches the toe of the reef. As it continues to climb up the reef, the wave front becomes steeper and a plunging wave develops along the reef edge and spreads across the entire reef flat in the experiment (Swigler, 2009; Roeber and Cheung, 2012). The steep wave front and spreading process are clearly captured by the numerical model as shown

at $t = 7$ s. After the wave breaks, the flow forms into a surge that runs up the dry beach slope as predicted by the model at $t = 14$ s. Gradually, the surge spreads into a sheet flow, which propagates and inundates the whole upper beach, and then it is reflected by the back wall. After that, the flow starts to withdraw from the beach, and more and more areas become dry as shown at $t = 29$ s. It is worth mentioning that the symmetric wave patterns during the whole process are correctly simulated by the numerical model, as presented in Figure 6.12.
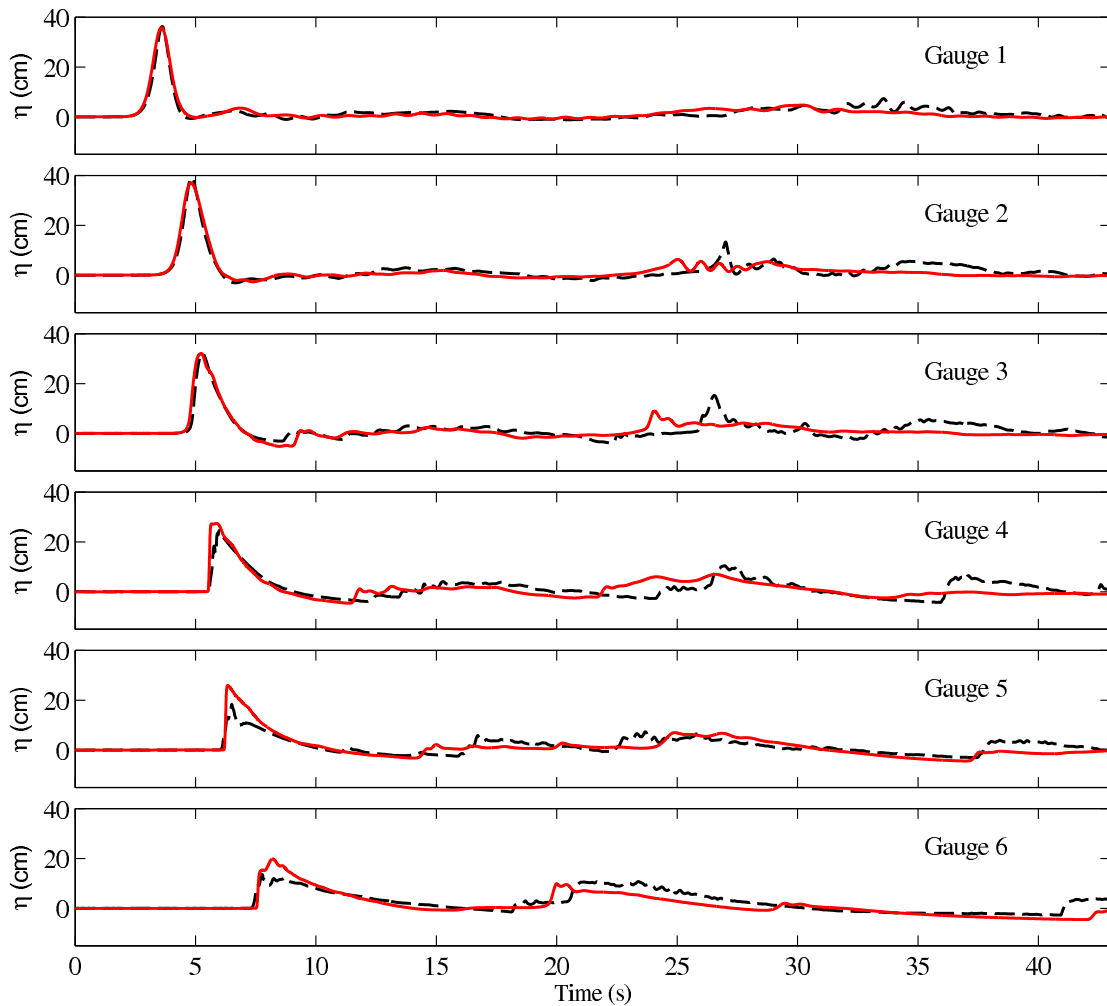
Figure 6.13. Comparison of simulated and measured time series of free surface elevations at six wave gauges along the basin centerline in Case I of Swigler (2009). Experimental data (dashed lines), numerical results (solid lines).

Next, we compare the numerical results with the available experimental data. Fig-

113
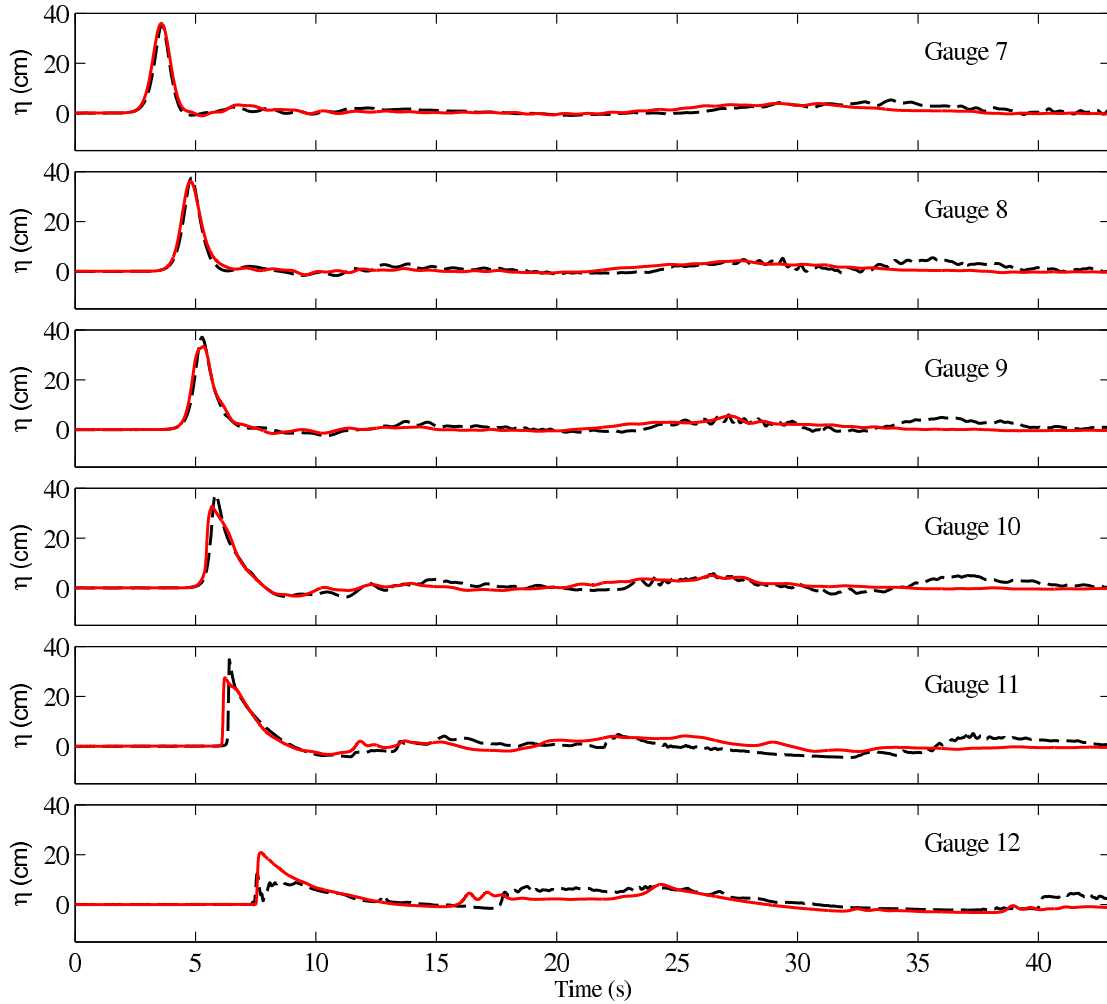
Figure 6.14. Comparison of simulated and measured time series of free surface elevations at six wave gauges along $x = $ -5 m in Case I of Swigler (2009). Experimental data (dashed lines), numerical results (solid lines).

ure 6.13 shows the comparison of simulated and measured time series of free surface elevations at six wave gauges along the centerline of the basin. The steepening and breaking of the solitary wave along the centerline are well captured by the model. The simulated wave breaking is slightly postponed at Gauges 3, 4, and 5, but the agreement quickly recovers at the end of wave breaking. Figure 6.14 shows the time series of free surface elevation comparison at six wave gauges along $x = $ -5 m, similar observations to those presented in the centerline can be drawn. As the wave process is mainly flux-dominated in the cross-shore direction, the along-shore velocity is smaller than the cross-shore one, and therefore, we only show the time

series of cross-shore velocity comparison at three gauges in Figure 6.15. The first velocity gauge was located along the centerline, and the numerical model successfully reproduces the velocity when the wave breaks. The other two velocity gauges were located at the flat reef, so they only recorded data after the wave breaks. The numerical results match well with the recorded data.
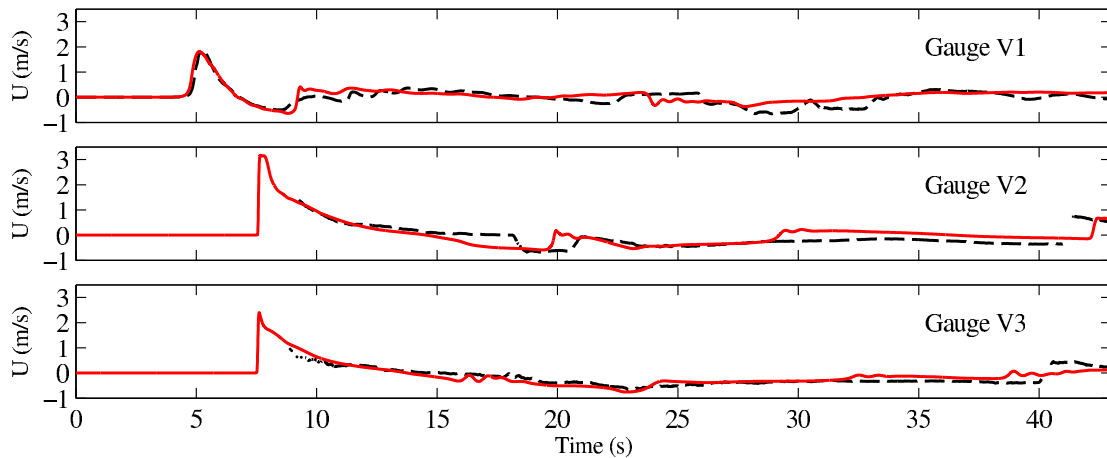
Figure 6.15. Comparison of simulated and measured time series of cross-shore velocities at three velocity gauges in Case I of Swigler (2009). Experimental data (dashed lines), numerical results (solid lines).

6.4.3   A triangular shaped reef with an island feature

For Case II, an island feature was added into the basin of Case I using a concrete cone, which makes the hydrodynamic and wave processes even more complicated over the triangular reef. In Figure 6.16, we also show a series of snapshots of free surface elevations in Case II as the solitary wave propagates, breaks, runs up, and retreats over the triangular shaped reef. At $t = 4$ s, the solitary wave reaches the toe of the reef. The wave shape is very similar to that of Case I. As the wave front becomes steeper, the wave breaks around the island and even overtops it, as shown at $t = 7$ s. After the wave breaks, the wave continues to surge over the beach slope. Due to the presence of the island, a more complex free surface distribution (e.g., refraction) compared with that in Case I is observed at $t = 14$ s. Once the surge climbs up the upper beach, a sheet flow is also formed and reflected by the back

wall. Finally, it flows back from the beach slope due to gravity.
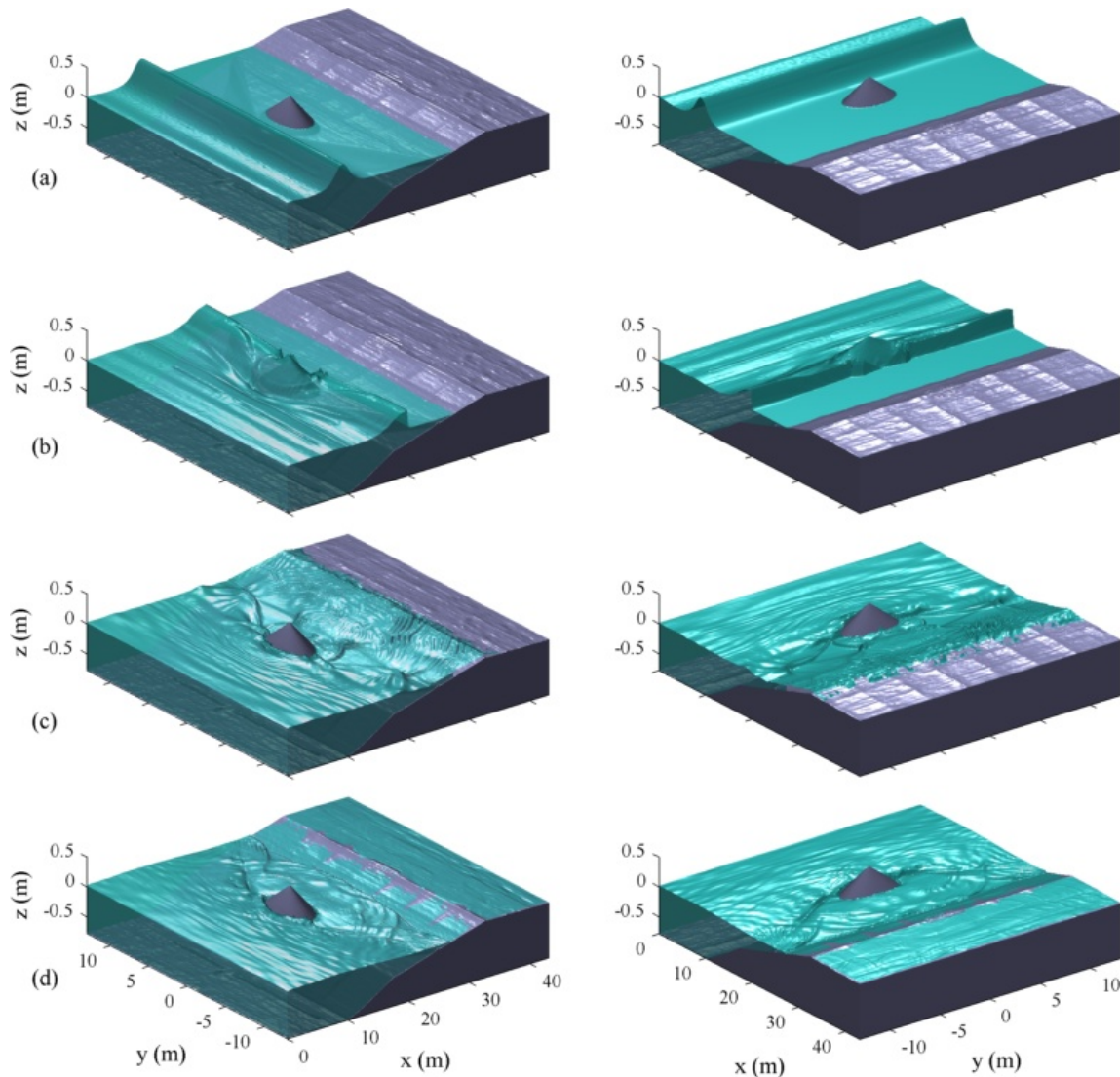
Figure 6.16. Snapshots of free surface elevations with both front and lee-side views in Case II of Swigler (2009). (a) t = 4 s, (b) t = 7 s, (c) t = 14 s, and (d) t = 29 s.

Figure 6.17 compares the simulated and measured time series of free surface elevations at nine gauges in the basin of Case II. The wave steepening and breaking processes are also well captured by the numerical model (see Gauges 1 - 6). There is a slight discrepancy of the wave breaking pattern at Gauges 3 and 6, and a similar prediction was reported by using the fully nonlinear Boussinesq-type model, FUNWAVE (Shi et al., 2012). Gauges 7, 8, and 9 were located at the side of the basin, and good agreement at these gauges indicates

that the numerical model also reasonably simulates the wave refraction near the sidewall. Figure 6.18 shows the comparison of time series of cross-shore velocity at three gauges, which were located at the same locations as those in Case I. The model correctly predicts the velocity trend at Gauges 1 and 3, but it slightly underpredicts the cross-shore velocity at Gauge 2. Overall, the agreement between the numerical results and the experimental data is comparable to that produced by FUNWAVE (Shi et al., 2012).
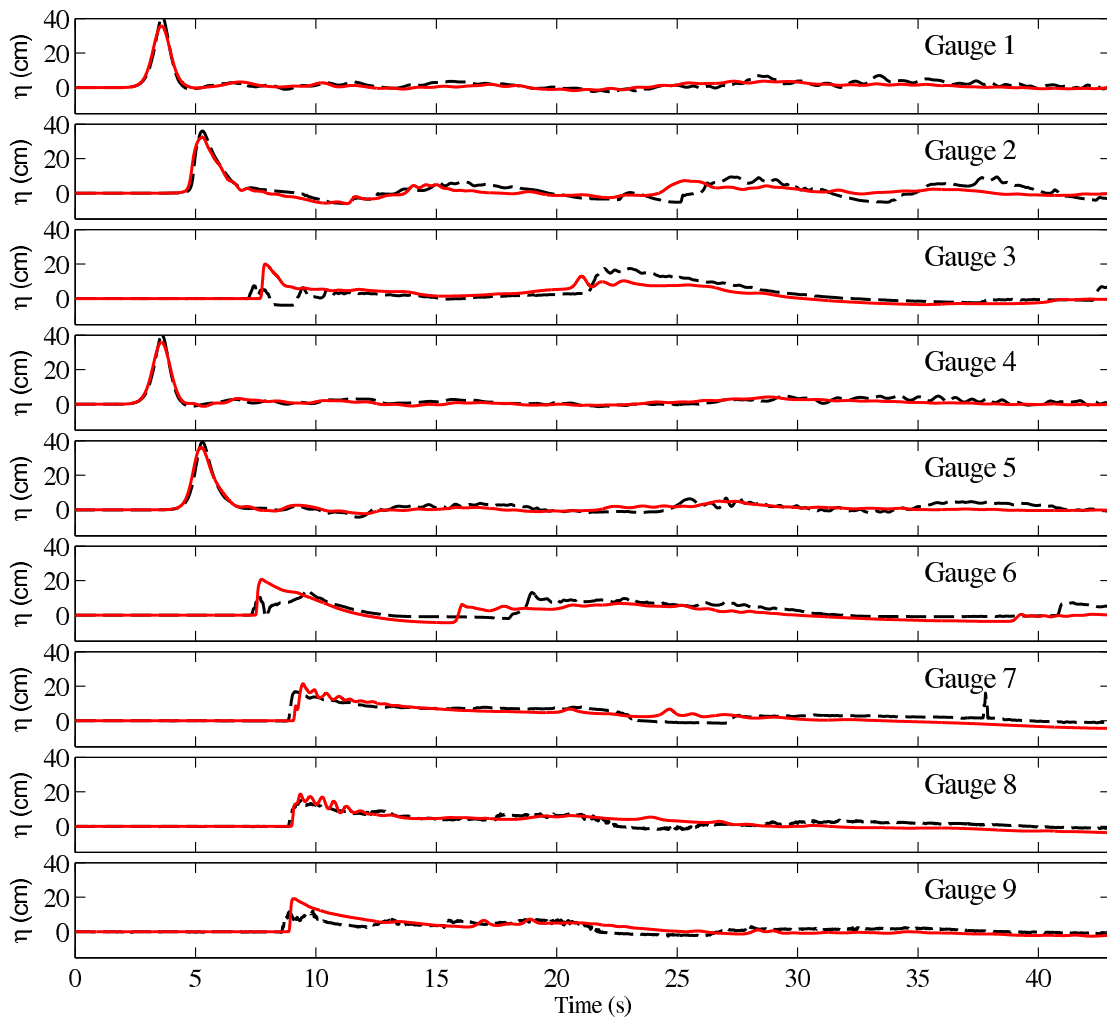
Figure 6.17. Comparison of simulated and measured time series of free surface elevations at nine wave gauges in Case II of Swigler (2009). Experimental data (dashed lines), numerical results (solid lines).

In summary, CCHE2D-NHWAVE has successfully simulated a set of benchmark data on tsunami wave transformation over a 3D reef. The experiment involves strongly nonlinear
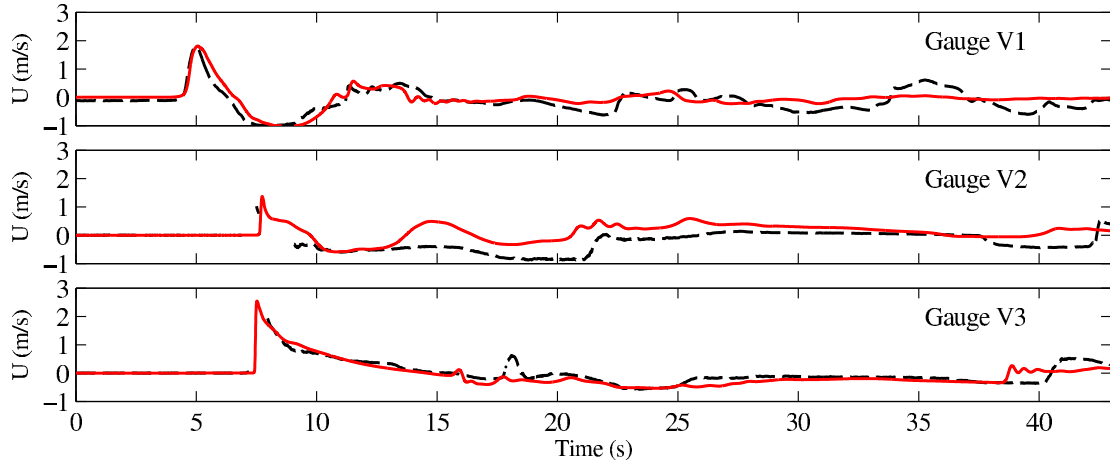
Figure 6.18. Comparison of simulated and measured time series of cross-shore velocities at three velocity gauges in Case II of Swigler (2009). Experimental data (dashed lines), numerical results (solid lines).

dispersive wave propagation, energetic wave breaking, and rapid wetting and drying process. The satisfactory prediction shows that a non-hydrostatic model with a mass and momentum conservation formulation and a simple wetting and drying scheme has a great potential to simulate tsunami wave hazards in the nearshore and coastal areas. Last but not least, we present the computation efficiency of the non-hydrostatic model. Previously, Case I has been simulated by a RANS model, OpenFOAM® (Higuera et al., 2013). Here we show the computation cost of this case by using OpenFOAM® and CCHE2D-NHWAVE, and present the comparison in Table 6.5. It can be seen that there is a huge difference between the two models in terms of computation cost. Be aware that similar numerical results have been obtained by both models, the advantage of a depth-integrated non-hydrostatic model is obvious from the computation efficiency point of view.

6.5   Chapter Summary

This chapter has applied CCHE2D-NHWAVE to study a wide range of coastal wave processes. Fairly good agreement between the numerical results and the measurements has demonstrated a good capability of the non-hydrostatic model to simulate the hydrodynamic process in the swash zone, wave transformation over fringing reefs of steep slopes and com-

118

Table 6.5. Comparison of computation cost of Case I of Swigler (2009).

	OpenFOAM®	CCHE2D-NHWAVE
Parallelization	Yes, using MPI	Not yet
Processor(s)	36 (1.9 GHz)	1 (2.69 GHz)
Domain size	a half size of wave basin	the whole wave basin
Mesh size (horizontally)	0.1 m	0.1 m
Mesh size (vertically)	0.06 m	one layer
Physical time	15 s	50 s
Computation time	approx. 7 days	approx. 2.5 hours

plex topography, wave attenuation through submerged and emergent vegetation zones, and tsunami wave breaking and inundation over a 3D reef. Although the test cases addressed could also be well simulated by other numerical techniques (e.g., the RANS model and the Boussinesq-type model), the non-hydrostatic model has an apparent advantage over them when it comes to the simplicity of numerical discretization and computational efficiency, and the advantage would be more prominent when a large-scale or real-life coastal wave process is considered.

CHAPTER 7

CONCLUSIONS AND RECOMMENDATIONS

7.1   Conclusions

This dissertation has developed a series of non-hydrostatic finite element wave models for simulating propagation, breaking, and run-up of dispersive waves in the coastal zone through the following steps:

(1) Development of a depth-integrated non-hydrostatic model for wave propagation. A depth-integrated non-hydrostatic finite element model for wave propagation has been developed by directly introducing a non-hydrostatic pressure module into the existing finite element free surface flow model, CCHE2D. The total pressure is decomposed into hydrostatic and non-hydrostatic parts, and the NLSW equations and a depth-integrated vertical momentum equation are solved with a linear distribution assumed in the vertical direction for the non-hydrostatic pressure and the vertical velocity. The solution of governing equations is split to several steps. First of all, a provisional velocity field is obtained without considering the non-hydrostatic pressure. And then the non-hydrostatic pressure is calculated by using the divergence-free velocity field condition. Next, the provisional velocity is updated by including the non-hydrostatic pressure terms. Finally, the free surface elevation is computed by the depth-integrated continuity equation. Several benchmark tests were carried out to verify and validate the depth-integrated non-hydrostatic wave model. The model is equivalent to or slightly better than the numerical models based on the classical Boussinesq-type equations for weakly dispersive waves, and it is evident that this model can properly handle the linear and nonlinear dispersive waves, wave shoaling, refraction, diffraction, and

120

focusing. However, this version of non-hydrostatic model is not able to simulate the wave breaking process (it has been identified, although it is not shown in the dissertation). Furthermore, a wetting and drying algorithm is needed to deal with the moving shoreline.

(2) Development of a depth-integrated non-hydrostatic model for simulating nearshore wave processes. A new depth-integrated non-hydrostatic finite element model for nearshore wave processes has been developed. The model solves a depth-integrated vertical momentum equation and the conservation form of the NLSW equations including extra non-hydrostatic pressure terms. A pressure projection method and the divergence-free velocity field condition are used together to solve the non-hydrostatic pressure. To simulate the discontinuous flow (e.g., wave breaking), the numerical model treats it as a hydraulic jump and obtain the correct free surface elevation at the end of wave breaking by ensuring that the mass and momentum are conserved at the discretized level. Furthermore, a simple but efficient wetting and drying algorithm is developed by considering global mass conservation. The numerical model has been intensively verified and validated by a series of analytical and experimental cases. First of all, three cases with analytical solutions have demonstrated that the non-hydrostatic wave model is well-balanced and efficient for modeling moving boundaries. And then four sets of laboratory experiments, which present several nearshore wave phenomena (e.g., nonlinear dispersive wave propagation, breaking, and run-up), have been used to evaluate the model's capability for simulating real-life and large-scale wave motions. Good agreements between numerical results and experimental data proved that the depth-integrated non-hydrostatic model is applicable to resolve a wide range of wave processes in the nearshore zone. Similar to the previous version of depth-integrated non-hydrostatic model, this model is limited to weakly dispersive waves, and this restriction can be alleviated or eliminated by extending it to be a multi-layer non-hydrostatic model with several vertical layers.

121

(3) Development of a multi-layer non-hydrostatic model with an improved capability for modeling nonlinear and dispersive waves. A multi-layer non-hydrostatic finite element model for simulating highly dispersive waves has been developed by extending more layers in the vertical direction of the model developed in the second objective. For this development, these vertical layers are chosen to be strictly horizontal in the vertical direction, and the edge-based pressure allocation method is implemented. To ensure mass and momentum conservation, the governing equations are obtained by the vertical integration of the RANS equations over each vertical layer. Similar to previous models, a pressure projection method is implemented and the numerical solution is decomposed into several steps. Several benchmark cases were carried out to verify its improved capability for highly nonlinear waves and highly dispersive waves. Although more vertical layers could be used, a two-layer non-hydrostatic model has clearly demonstrated the superiority of the multi-layer model over the depth-integrated model with respect to modeling highly dispersive waves.

(4) Application of the non-hydrostatic model for simulating coastal wave processes. The ultimate goal for this dissertation research is to simulate coastal waves by using the developed the non-hydrostatic finite element models, this was achieved by applying the depth-integrated non-hydrostatic model, CCHE2D-NHWAVE, for simulating several types of coastal wave processes. Specifically, the model is applied to (a) predict the swash zone hydrodynamics involving wave bore propagation, (b) resolve wave propagation, breaking, and overtopping in fringing reef environments with steep reef slopes, (c) study the vegetation effect on wave height reduction through both submerged and emergent vegetation zones using the drag force term technique, and (d) simulate tsunami wave breaking in the nearshore zone and inundation in the coastal area. Satisfactory agreement between numerical result and benchmark data confirmed that the non-hydrostatic model is capable of modeling a wide range of coastal wave processes. Furthermore, thanks to its simple numerical formulation, the non-hydrostatic

model also demonstrates a better computation efficiency when comparing with other numerical models.

To conclude, this dissertation has fulfilled its research objectives, and the developed non-hydrostatic finite element wave models are ready to be applied to study real-life coastal wave processes.

7.2 Recommendations

Based on the experience gained through this dissertation research, we recommend several research directions to further improve the current work as follows:

(1) Improvement of the multi-layer non-hydrostatic model. To ensure the mass is strictly conserved in the framework of a finite element model, we adopted the z - level grid method in the vertical direction of the multi-layer method. This strategy brings about a limitation for cases with rapidly varying topography. In deep water, it is possible that all vertical layers are active, on the other hand, it might only have one or two layers are active in the nearshore zone, there is an unbalance of computation loads. Furthermore, the wetting and drying treatment is also complicated as the number of active layers varies node by node in the coastal zone. An alternative vertical grid scheme is the so-called sigma coordinate system, which is particularly useful when dealing with the wetting and drying process. Since the total number of vertical grids are constant, the total water depth is only needed to be evaluated when determining the wetting and drying cells. The challenging part for this coordinate system is to ensure the correct mass conservation when solving the non-hydrostatic pressure using the local continuity equation. As the vertical layer interface varies at each time step, resulting in extra spatial and temporal gradient terms of the layer interface in the horizontal momentum equations, some mixed spatial and temporal terms are introduced when applying the divergence operators (i.e., $\frac{\partial}{\partial x}$ and $\frac{\partial}{\partial y}$) in the local continuity equation. As a result, the numerical solution of this equation is much more complicated than the

one obtained by assuming a strictly horizontal layer interface, as implemented in this study. However, it is worth investing efforts on this improvement, which will make the model more robust in real-life applications.

(2) Implementation of a high-order time integration scheme. Through this dissertation, the two-stage prediction-and-correction time integration scheme works very well. This is mainly due to two reasons: (a) simulation of short waves requires a small numerical time step, and (b) many numerical experiments considered in this work are flux-dominated and the physical time of laboratory experiments is also very short. As a result, some issues (e.g., a phase lag between numerical results and the measurements) due to a low-order time integration scheme are not exposed in the numerical tests. However, when the model is applied for simulating wave propagation for a long distance and for a long period of time, a high-order time integration scheme is valuable for obtaining a correct prediction.

(3) Adaption of the momentum conservation discretization and the wetting and drying algorithm to be compatible with a non-orthogonal grid. The existing CCHE2D model was implemented on a non-orthogonal grid system. But the momentum conservation discretization and the wetting and drying scheme presented in Chapter 4 are based on the assumption that the mesh is rectangular, and the finite difference scheme was used for the advection term discretization. At the current stage, all considered verification and validation cases have a simple geometry and they are discretized with a rectangular grid, and therefore both implementations are applicable in the CCHE2D model. However, to apply the developed model to real-life coastal wave processes, which involve a complex domain, there is a need to transform the momentum conservation discretization and the wetting and drying algorithm to be compatible with the non-orthogonal grid.

(4) Application of the non-hydrostatic model for more challenging coastal waves. In the

numerical formulation of a non-hydrostatic model, the high-order term is only up to a second-order, so the discretization is simple. In addition, the non-hydrostatic model is able to simulate highly dispersive waves using a very limited number of vertical grids. It is no doubt that the non-hydrostatic model provides a simpler numerical technique for simulating coastal wave processes when comparing with other numerical models (e.g., the RANS and the Boussinesq-type models). This improvement builds a great foundation to enhance the non-hydrostatic model to address other coastal wave processes, e.g., landslide-generated tsunami, wave-induced sediment transport, and wave-current interaction.

(5) Improvement of computation efficiency. It is well-known that Boussinesq-type models involve complex numerical formulations with high-order temporal and spatial derivatives. In this work, the highest order terms used in the non-hydrostatic model are only second-order, so the non-hydrostatic model has a simpler numerical formulation than that of the Boussinesq-type models. As a result, this improvement may also result in a cheaper computational cost. Furthermore, the non-hydrostatic model has an apparent advantage over the RANS model for simulating wave processes in view of computation time as demonstrated in Chapter 6. To efficiently simulate a large-scale physical experiment, and even model the real-life coastal wave processes, there is still a demand to improve the computational efficiency of the non-hydrostatic model by using state-of-the-art computing technique, e.g., GPU computing.

BIBLIOGRAPHY

BIBLIOGRAPHY

Agnon, Y., P. A. Madsen, and H. Schäffer (1999), A new approach to high-order Boussinesq models, *Journal of Fluid Mechanics*, 399, 319–333.

Ai, C., and S. Jin (2012), A multi-layer non-hydrostatic model for wave breaking and run-up, *Coastal Engineering*, 62, 1–8.

Ai, C., S. Jin, and B. Lv (2010), A new fully non-hydrostatic 3D free surface flow model for water wave motions, *International Journal for Numerical Methods in Fluids*, 66(11), 1354–1370.

Asano, T., S. Tsutsui, and T. Sakai (1988), Wave damping characteristics due to seaweed, in *Proceedings of the 35th Japanese Conference on Coastal Engineering*, pp. 138–142.

Austin, M. J., and G. Masselink (2006), Observations of morphological change and sediment transport on a steep gravel beach, *Marine Geology*, 229(1), 59–77.

Barnes, M. P., T. O'Donoghue, J. M. Alsina, and T. E. Baldock (2009), Direct bed shear stress measurements in bore-driven swash, *Coastal Engineering*, 56(8), 853–867.

Beji, S., and J. A. Battjes (1993), Experimental investigation of wave propagation over a bar, *Coastal Engineering*, 19(1), 151–162.

Beji, S., and J. A. Battjes (1994), Numerical simulation of nonlinear wave propagation over a bar, *Coastal Engineering*, 23(1), 1–16.

Beltrami, G. M., G. Bellotti, P. D. Girolamo, and P. Sammarco (2001), Treatment of wave breaking and total absorption in a mild-slope equation FEM model, *Journal of Waterway, Port, Coastal, and Ocean Engineering*, 127(5), 263–271.

Berkhoff, J. C. W. (1976), Mathematical models for simple harmonic linear water waves: wave diffraction and refraction, Ph.D. thesis, Delft University of Technology, the Netherlands.

Berkhoff, J. C. W., N. Booy, and A. C. Radder (1982), Verification of numerical wave propagation models for simple harmonic linear water waves, *Coastal Engineering*, 6(3), 255–279.

Booij, N. (1983), A note on the accuracy of the mild-slope equation, *Coastal Engineering*, 7(3), 191–203.

Brander, R. W., P. S. Kench, and D. Hart (2004), Spatial and temporal variations in wave characteristics across a reef platform, Warraber Island, Torres Strait, Australia, *Marine Geology*, 207(1), 169–184.

Briggs, M. J., C. E. Synolakis, G. S. Harkins, and D. R. Green (1995), Laboratory experiments of tsunami runup on a circular island, in *Tsunamis: 1992–1994*, pp. 569–593, Springer.

Briggs, M. J., C. E. Synolakis, U. Kanoglu, and D. R. Green (1996), Runup of solitary waves on a vertical wall, in *Long-wave runup models*, edited by H. H. J. Yeh, P. L. F. Liu, and C. E. Synolakis, pp. 375–383, World Scientific, Singapore.

Carrier, G. F., and H. P. Greenspan (1958), Water waves of finite amplitude on a sloping beach, *Journal of Fluid Mechanics*, 4(1), 97–109.

Carrier, G. F., T. T. Wu, and H. Yeh (2003), Tsunami run-up and draw-down on a plane beach, *Journal of Fluid Mechanics*, 475(1), 79–99.

Casulli, V. (1999), A semi-implicit finite difference method for non-hydrostatic, free-surface flows, *International Journal for Numerical Methods in Fluids*, 30(4), 425–440.

Casulli, V., and G. S. Stelling (1998), Numerical simulation of 3D quasi-hydrostatic, free-surface flows, *Journal of Hydraulic Engineering*, 124(7), 678–686.

Casulli, V., and P. Zanolli (2002), Semi-implicit numerical modeling of nonhydrostatic free-surface flows for environmental problems, *Mathematical and Computer Modelling*, 36(9), 1131–1149.

Chamberlain, P., and D. Porter (1995), The modified mild-slope equation, *Journal of Fluid Mechanics*, 291, 393–407.

Chen, W., V. Panchang, and Z. Demirbilek (2005), On the modeling of wave–current interaction using the elliptic mild-slope wave equation, *Ocean Engineering*, 32(17), 2135–2164.

Chen, X. J. (2003), A fully hydrodynamic model for three-dimensional, free-surface flows, *International Journal for Numerical Methods in Fluids*, 42(9), 929–952.

Christensen, E. D., and R. Deigaard (2001), Large eddy simulation of breaking waves, *Coastal Engineering*, 42(1), 53–86.

Cui, H., J. D. Pietrzak, and G. S. Stelling (2012), Improved efficiency of a non-hydrostatic, unstructured grid, finite volume model, *Ocean Modelling*, 54-55, 55–67.

Dalrymple, R. A., and B. D. Rogers (2006), Numerical modeling of water waves with the SPH method, *Coastal Engineering*, 53(2), 141–147.

Dalrymple, R. A., J. T. Kirby, and P. A. Hwang (1984), Wave diffraction due to areas of energy dissipation, *Journal of Waterway, Port, Coastal, and Ocean Engineering*, 110(1), 67–79.

Demirbilek, Z., and V. Panchang (1998), CGWAVE: A Coastal Surface Water Wave Model of the Mild Slope Equation, *Tech. rep.*, Army Engineer Waterways Experiment Station, Vicksburg, USA.

Dietrich, J., et al. (2011), Hurricane Gustav (2008) waves and storm surge: hindcast, synoptic analysis, and validation in Southern Louisiana., *Monthly Weather Review*, 139(8).

Ding, Y., and S. S. Y. Wang (2008), Development and application of a coastal and estuarine morphological process modeling system, *Journal of Coastal Research*, pp. 127–140.

Ding, Y., M. S. Altinakar, Y. Jia, S. N. Kuiry, Y. Zhang, and A. Goodman (2012), Simulation of storm surge in the Mississippi Gulf Coast using an integrated coastal processes model, in *World Environmental and Water Resources Congress 2012*, pp. 1635–1652, Albuquerque, USA.

Dingemans, M. W. (1997), *Water wave propagation over uneven bottoms: Linear wave propagation*, World Scientific, Singapore.

Enet, F., and S. T. Grilli (2007), Experimental study of tsunami generation by three-dimensional rigid underwater landslides, *Journal of Waterway, Port, Coastal, and Ocean Engineering*, 133(6), 442–454.

Fuhrman, D. R., and P. A. Madsen (2008), Simulation of nonlinear wave run-up with a high-order Boussinesq model, *Coastal Engineering*, 55(2), 139–154.

Fuhrman, D. R., and P. A. Madsen (2009), Tsunami generation, propagation, and run-up with a high-order Boussinesq model, *Coastal Engineering*, 56(7), 747–758.

Gingold, R. A., and J. J. Monaghan (1977), Smoothed particle hydrodynamics-theory and application to non-spherical stars, *Monthly Notices of the Royal Astronomical Society*, 181, 375–389.

Gobbi, M. F., J. T. Kirby, and G. Wei (2000), A fully nonlinear Boussinesq model for surface waves. Part 2. Extension to $O(kh)^4$, *Journal of Fluid Mechanics*, 405(1), 181–210.

Gomez-Gesteira, M., and R. A. Dalrymple (2004), Using a three-dimensional smoothed particle hydrodynamics method for wave impact on a tall structure, *Journal of Waterway, Port, Coastal, and Ocean Engineering*, 130(2), 63–69.

Grilli, S. T., J. C. Harris, T. S. T. Bakhsh, T. L. Masterlark, C. Kyriakopoulos, J. T. Kirby, and F. Shi (2013), Numerical simulation of the 2011 Tohoku tsunami based on a new transient FEM co-seismic source: Comparison to far-and near-field observations, *Pure and Applied Geophysics*, 170(6-8), 1333–1359.

Harlow, F. H., and J. E. Welch (1965), Numerical calculation of time-dependent viscous incompressible flow of fluid with free surface, *Physics of Fluids*, 8, 2182.

Hérault, A., G. Bilotta, and R. A. Dalrymple (2010), SPH on GPU with CUDA, *Journal of Hydraulic Research*, 48(S1), 74–79.

Higuera, P., J. L. Lara, and I. J. Losada (2013), Simulating coastal engineering processes with OpenFOAM®, *Coastal Engineering*, 71, 119–134.

Hirsch, C. (2007), *Numerical computation of internal and external flows: the fundamentals of computational fluid dynamics*, vol. 1, second ed., Butterworth-Heinemann, Oxford, UK.

Hirt, C. W., and B. D. Nichols (1981), Volume of fluid (VOF) method for the dynamics of free boundaries, *Journal of Computational Physics*, 39(1), 201–225.

Hughes, M. G. (1992), Application of a non-linear shallow water theory to swash following bore collapse on a sandy beach, *Journal of Coastal Research*, pp. 562–578.

Jia, Y. (2013a), Technical manual of CCHE2D (Version 4.1), *Tech. rep.*, National Center for Computational Hydroscience and Engineering, The University of Mississippi.

Jia, Y. (2013b), Technical manual of CCHE3D (Version 3.1), *Tech. rep.*, National Center for Computational Hydroscience and Engineering, The University of Mississippi, USA.

Jia, Y., and S. S. Y. Wang (1999), Numerical model for channel flow and morphological change studies, *Journal of Hydraulic Engineering*, 125(9), 924–933.

Jia, Y., and S. S. Y. Wang (2001), CCHE2D: A two-dimensional hydrodynamic and sediment transport model for unsteady open channel flows over loose bed, *Tech. rep.*, National Center for Computational Hydroscience and Engineering, The University of Mississippi, Mississippi, USA.

Jia, Y., S. S. Y. Wang, and Y. Xu (2002), Validation and application of a 2D model to channels with complex geometry, *International Journal of Computational Engineering Science*, 3(01), 57–71.

Kirby, J. T. (1984), A note on linear surface wave-current interaction over slowly varying topography, *Journal of Geophysical Research: Oceans (1978–2012)*, 89(C1), 745–747.

Kroon, A. (2009), Implementation of a wetting and drying algorithm in a finite element model, Master's thesis, Delft University of Technology, the Netherlands.

Kubo, Y., Y. Kotake, M. Isobe, and A. Watanabe (1992), Time-dependent mild slope equation for random waves, in *Proceedings of 23th International Conference on Coastal Engineering*, vol. 1, pp. 285–299, Venice, Italy.

Lam, D. C. L., and R. B. Simpson (1976), Centered differencing and the box scheme for diffusion convection problems, *Journal of Computational Physics*, 22(4), 486–500.

Lara, J., N. Garcia, and I. Losada (2006), RANS modelling applied to random wave interaction with submerged permeable structures, *Coastal Engineering*, 53(5), 395–417.

Li, B., and C. A. Fleming (2001), Three-dimensional model of Navier-Stokes equations for water waves, *Journal of Waterway, Port, Coastal, and Ocean Engineering*, 127(1), 16–25.

Li, C. W., and K. Yan (2007), Numerical investigation of wave–current–vegetation interaction, *Journal of Hydraulic Engineering*, 133(7), 794–803.

Li, R. M., and H. W. Shen (1973), Effect of tall vegetations on flow and sediment, *Journal of the Hydraulics Division*, 99(5), 793–814.

Liang, Q., and F. Marche (2009), Numerical resolution of well-balanced shallow water equations with complex source terms, *Advances in Water Resources*, 32(6), 873–884.

Lin, P., and P. L. F. Liu (1998a), A numerical study of breaking waves in the surf zone, *Journal of Fluid Mechanics*, 359(1), 239–264.

Lin, P., and P. L.-F. Liu (1998b), Turbulence transport, vorticity dynamics, and solute mixing under plunging breaking waves in surf zone, *Journal of Geophysical Research: Oceans (1978–2012)*, 103(C8), 15,677–15,694.

Lin, P., K. Chang, and P. L. F. Liu (1999), Runup and rundown of solitary waves on sloping beaches, *Journal of Waterway, Port, Coastal, and Ocean Engineering*, 125(5), 247–255.

Liu, M. B., and G. R. Liu (2010), Smoothed particle hydrodynamics (SPH): an overview and recent developments, *Archives of Computational Methods in Engineering*, 17(1), 25–76.

Liu, P. L. F., and I. J. Losada (2002), Wave propagation modeling in coastal engineering, *Journal of Hydraulic Research*, 40(3), 229–240.

Liu, P. L. F., Y. S. Cho, M. J. Briggs, U. Kanoglu, and C. E. Synolakis (1995), Runup of solitary waves on a circular island, *Journal of Fluid Mechanics*, 302, 259–286.

Lucy, L. B. (1977), A numerical approach to the testing of the fission hypothesis, *The Astronomical Journal*, 82, 1013–1024.

Lugo-Fernández, A., H. H. Roberts, and J. N. Suhayda (1998), Wave transformations across a Caribbean fringing-barrier coral reef, *Continental Shelf Research*, 18(10), 1099–1124.

Luth, H. R., G. Klopman, and N. Kitou (1994), Project 13G: Kinematics of waves breaking partially on an offshore bar; LDV measurements for waves with and without a net onshore current, *Delft Hydraulics Report H*, 1573, 40.

Lynett, P., and P. L.-F. Liu (2004), A two-layer approach to wave modelling, *Proceedings of the Royal Society of London. Series A: Mathematical, Physical and Engineering Sciences*, 460(2049), 2637–2669.

Lynett, P. J., T. R. Wu, and P. L. F. Liu (2002), Modeling wave runup with depth-integrated equations, *Coastal Engineering*, 46(2), 89–107.

Ma, G., F. Shi, and J. T. Kirby (2012), Shock-capturing non-hydrostatic model for fully dispersive surface wave processes, *Ocean Modelling*, 43-44, 22–35.

Madsen, P. A., and O. R. Sørensen (1992), A new form of the Boussinesq equations with improved linear dispersion characteristics. Part 2. A slowly-varying bathymetry, *Coastal Engineering*, 18(3), 183–204.

Madsen, P. A., R. Murray, and O. R. Sørensen (1991), A new form of the Boussinesq equations with improved linear dispersion characteristics, *Coastal Engineering*, 15(4), 371–388.

Madsen, P. A., H. B. Bingham, and H. Liu (2002), A new Boussinesq method for fully nonlinear waves from shallow to deep water, *Journal of Fluid Mechanics*, 462(3), 1–30.

Madsen, P. A., H. B. Bingham, and H. A. Schäffer (2003), Boussinesq-type formulations for fully nonlinear and extremely dispersive water waves: derivation and analysis, *Proceedings of the Royal Society of London. Series A: Mathematical, Physical and Engineering Sciences*, 459(2033), 1075–1104.

Massel, S. R. (1993), Extended refraction-diffraction equation for surface waves, *Coastal Engineering*, 19(1), 97–126.

Maxworthy, T. (1976), Experiments on collisions between solitary waves, *Journal of Fluid Mechanics*, 76(01), 177–186.

Maza, M., J. L. Lara, and I. J. Losada (2013), A coupled model of submerged vegetation under oscillatory flow using Navier–Stokes equations, *Coastal Engineering*, 80, 16–34.

Monaghan, J. J. (1994), Simulating free surface flows with SPH, *Journal of Computational Physics*, 110(2), 399–406.

Munson, B. R., D. F. Young, and T. H. Okiishi (2002), *Fundamentals of Fluid Mechanics*, 4th ed., John Wiley & Sons Inc, New York, USA.

Nadaoka, K., S. Beji, and Y. Nakagawa (1994), A fully-dispersive nonlinear wave model and its numerical solutions, in *Coastal Engineering Proceedings*, vol. 1, pp. 427–441.

Namin, M. M., B. Lin, and R. A. Falconer (2001), An implicit numerical algorithm for solving non-hydrostatic free-surface flow problems, *International Journal for Numerical Methods in Fluids*, 35(3), 341–356.

Nepf, H. M. (1999), Drag, turbulence, and diffusion in flow through emergent vegetation, *Water Resources Research*, 35(2), 479–489.

Nwogu, O. (1993), Alternative form of Boussinesq equations for nearshore wave propagation, *Journal of Waterway, Port, Coastal, and Ocean Engineering*, 119(6), 618–638.

O'Donoghue, T., D. Pokrajac, and L. Hondebrink (2010), Laboratory and numerical study of dambreak-generated swash on impermeable slopes, *Coastal Engineering*, 57(5), 513–530.

Peregrine, D. H. (1967), Long waves on a beach, *Journal of Fluid Mechanics*, 27(4), 815–827.

Puleo, J. A., R. A. Beach, R. A. Holman, and J. S. Allen (2000), Swash zone sediment suspension and transport and the importance of bore-generated turbulence, *Journal of Geophysical Research: Oceans (1978–2012)*, 105(C7), 17,021–17,044.

Ren, B., H. Wen, P. Dong, and Y. Wang (2014), Numerical simulation of wave interaction with porous structures using an improved smoothed particle hydrodynamic method, *Coastal Engineering*, 88, 88–100.

Rijnsdorp, D. P., P. B. Smit, and M. Zijlema (2014), Non-hydrostatic modelling of infragravity waves under laboratory conditions, *Coastal Engineering*, 85, 30–42.

Rodi, W. (1993), *Turbulence models and their application in hydraulics*, CRC Press.

Roeber, V., and K. F. Cheung (2012), Boussinesq-type model for energetic breaking waves in fringing reef environments, *Coastal Engineering*, 70, 1–20.

Roeber, V., K. F. Cheung, and M. H. Kobayashi (2010), Shock-capturing Boussinesq-type model for nearshore wave processes, *Coastal Engineering*, 57(4), 407–423.

Saad, Y. (2005), SPARSKIT: a basic tool kit for sparse matrix computations, version 2, *Software available at http://www. cs. umn. edu/ saad.*

Satake, K. (1995), Linear and nonlinear computations of the 1992 Nicaragua earthquake tsunami, in *Tsunamis: 1992–1994*, pp. 455–470, Springer.

Schäffer, H. A., P. A. Madsen, and R. Deigaard (1993), A Boussinesq model for waves breaking in shallow water, *Coastal Engineering*, 20(3), 185–202.

Shi, F., J. T. Kirby, J. C. Harris, J. D. Geiman, and S. T. Grilli (2012), A high-order adaptive time-stepping TVD solver for Boussinesq modeling of breaking waves and coastal inundation, *Ocean Modelling*, 43, 36–51.

Smagorinsky, J. (1963), General circulation experiments with the primitive equations: I. the basic experiment, *Monthly Weather Review*, 91(3), 99–164.

Smit, P., M. Zijlema, and G. S. Stelling (2013), Depth-induced wave breaking in a non-hydrostatic, near-shore wave model, *Coastal Engineering*, 76, 1–16.

Smit, P., T. Janssen, L. Holthuijsen, and J. Smith (2014), Non-hydrostatic modeling of surf zone wave dynamics, *Coastal Engineering*, 83, 36–48.

Sorensen, R. M. (2006), *Basic Coastal Engineering*, 3 ed., Springer.

Stansby, P. K., and J. G. Zhou (1998), Shallow-water flow solver with non-hydrostatic pressure: 2D vertical plane problems, *International Journal for Numerical Methods in Fluids*, 28(3), 541–563.

Stansby, P. K., A. Chegini, and T. C. D. Barnes (1998), The initial stages of dam-break flow, *Journal of Fluid Mechanics*, 374, 407–424.

Stelling, G. S., and S. P. A. Duinmeijer (2003), A staggered conservative scheme for every Froude number in rapidly varied shallow water flows, *International Journal for Numerical Methods in Fluids*, 43(12), 1329–1354.

Stelling, G. S., and M. Zijlema (2003), An accurate and efficient finite-difference algorithm for non-hydrostatic free-surface flow with application to wave propagation, *International Journal for Numerical Methods in Fluids*, 43(1), 1–23.

Stone, H. L. (1968), Iterative solution of implicit approximations of multidimensional partial differential equations, *SIAM Journal on Numerical Analysis*, 5(3), 530–558.

Suh, K. D., C. Lee, and W. S. Park (1997), Time-dependent equations for wave propagation on rapidly varying topography, *Coastal Engineering*, 32(2), 91–117.

Swigler, D. T. (2009), Laboratory study investigating the three dimensional turbulence and kinematic properties associated with a breaking solitary wave, Master's thesis, Texas A&M University, USA.

Thacker, W. C. (1981), Some exact solutions to the nonlinear shallow-water wave equations, *Journal of Fluid Mechanics*, 107(1), 499–508.

Titov, V. V., and C. E. Synolakis (1995), Modeling of breaking and nonbreaking long-wave evolution and runup using VTCS-2, *Journal of Waterway, Port, Coastal, and Ocean Engineering*, 121(6), 308–316.

Titov, V. V., and C. E. Synolakis (1998), Numerical modeling of tidal wave runup, *Journal of Waterway, Port, Coastal, and Ocean Engineering*, 124(4), 157–171.

Tonelli, M., and M. Petti (2010), Finite volume scheme for the solution of 2D extended Boussinesq equations in the surf zone, *Ocean Engineering*, 37(7), 567–582.

Van der Vorst, H. A. (1992), Bi-CGSTAB: A fast and smoothly converging variant of Bi-CG for the solution of nonsymmetric linear systems, *SIAM Journal on Scientific and Statistical Computing*, 13(2), 631–644.

Veeramony, J., and I. A. Svendsen (2000), The flow in surf-zone waves, *Coastal Engineering*, 39(2), 93–122.

Walters, R. A. (2005), A semi-implicit finite element model for non-hydrostatic (dispersive) surface waves, *International Journal for Numerical Methods in Fluids*, 49(7), 721–737.

Wang, S. S. Y., and K. K. Hu (1992), Improved methodology for formulating finite element hydrodynamic models, *Finite Elements in Fluids*, 8, 457–478.

Watson, G., T. C. D. Barnes, and D. H. Peregrine (1996), Numerical modelling of solitary wave propagation and breaking on a beach and runup on a vertical wall, in *Long-wave runup models*, edited by H. H. J. Yeh, P. L. F. Liu, and C. E. Synolakis, pp. 291–297, World Scientific, Singapore.

Wei, G., and J. T. Kirby (1995), Time-dependent numerical code for extended Boussinesq equations, *Journal of Waterway, Port, Coastal, and Ocean Engineering*, 121(5), 251–261.

Wei, G., J. T. Kirby, S. T. Grilli, and R. Subramanya (1995), A fully nonlinear Boussinesq model for surface waves. Part 1. Highly nonlinear unsteady waves, *Journal of Fluid Mechanics*, 294, 71–92.

Wei, G., J. T. Kirby, and A. Sinha (1999), Generation of waves in Boussinesq models using a source function method, *Coastal Engineering*, 36(4), 271–299.

Wei, Y., X. Z. Mao, and K. F. Cheung (2006), Well-balanced finite-volume model for long-wave runup, *Journal of Waterway, Port, Coastal, and Ocean Engineering*, 132(2), 114–124.

Wu, W. (2007), *Computational river dynamics*, Taylor & Francis Group, London, UK.

Wu, W., M. Zhang, Y. Ozeren, and D. Wren (2012), Analysis of vegetation effect on waves using a vertical 2D RANS model, *Journal of Coastal Research*, 29(2), 383–397.

Yamazaki, Y., Z. Kowalik, and K. F. Cheung (2008), Depth-integrated, non-hydrostatic model for wave breaking and run-up, *International Journal for Numerical Methods in Fluids*, 61(5), 473–497.

Yeh, H. H. J., P. L. F. Liu, and C. E. Synolakis (1996), *Long-wave runup models*, World Scientific, Singapore.

Yuan, H., and C. H. Wu (2004), An implicit three-dimensional fully non-hydrostatic model for free-surface flows, *International Journal for Numerical Methods in Fluids*, 46(7), 709–733.

Zelt, J. A. (1991), The run-up of nonbreaking and breaking solitary waves, *Coastal Engineering*, 15(3), 205–246.

Zhou, J. G., D. M. Causon, C. G. Mingham, and D. M. Ingram (2004), Numerical prediction of dam-break flows in general geometries with complex bed topography, *Journal of Hydraulic Engineering*, 130(4), 332–340.

Zijlema, M., and G. S. Stelling (2005), Further experiences with computing non-hydrostatic free-surface flows involving water waves, *International Journal for Numerical Methods in Fluids*, 48(2), 169–197.

Zijlema, M., and G. S. Stelling (2008), Efficient computation of surf zone waves using the nonlinear shallow water equations with non-hydrostatic pressure, *Coastal Engineering*, 55(10), 780–790.

Zijlema, M., G. S. Stelling, and P. Smit (2011), SWASH: An operational public domain code for simulating wave fields and rapidly varied flows in coastal waters, *Coastal Engineering*, 58(10), 992–1012.

VITA

Zhangping Wei was born on December 7, 1984 at Luzhou city, Sichuan Province, China. He received the degree of Bachelor of Engineering with Honours from Hohai University, China in June 2008. And then he obtained the degree of Master of Engineering from Nanjing Hydraulic Research Institute, China in July 2010. He entered the National Center for Computational Hydroscience and Engineering at The University of Mississippi for the degree of Doctor of Philosophy in August 2010.